UNIVERSITY OF OKLAHOMA

GRADUATE COLLEGE

APPLICATION OF SEISMIC ATTRIBUTES AND MACHINE LEARNING CLUSTERING TECHNIQUES TO THE CHARACTERIZATION OF FAULTS IN A POST-SALT RESERVOIR, JUBARTE FIELD (CAMPOS BASIN)

A THESIS

SUBMITTED TO THE GRADUATE FACULTY

in partial fulfillment of the requirements for the

Degree of

MASTER OF SCIENCE

By

EDIMAR PERICO

Norman, Oklahoma

2021

Downloaded from SHAREOK. Persistent Handle URL: https://hdl.handle.net/11244/329540

APPLICATION OF SEISMIC ATTRIBUTES AND MACHINE LEARNING CLUSTERING TECHNIQUES TO THE CHARACTERIZATION OF FAULTS IN A POST-SALT RESERVOIR, JUBARTE FIELD (CAMPOS BASIN)

A THESIS APPROVED FOR THE

SCHOOL OF GEOSCIENCES

BY THE COMMITTEE CONSISTING OF

Dr. Heather Bedle, Chair

Dr. Brett M. Carpenter

Dr. Matthew J. Pranter

© Copyright by EDIMAR PERICO 2021

All Rights Reserved.

To my wife and kids

ACKNOWLEDGEMENTS

I would first like to express my sincere thanks to my company, Petróleo Brasileiro S.A. (Petrobras), for giving me support to study at the University of Oklahoma. I will always be grateful for this opportunity to pursue a Master's degree in Geophysics. I am also grateful to the Brazilian National Agency of Petroleum, Natural Gas and Biofuels (ANP), which in conjunction with Petrobras, authorized me to use datasets from the Jubarte Field for my research. Thanks to many company colleagues who encouraged and helped me prepare the required documents before and during my stay in Norman.

I would also like to extend my deepest gratitude to my advisor, Dr. Heather Bedle. Thanks for all the suggestions I received during my master's studies. Your knowledge, optimism, and comprehension really helped me to expand my understanding of many geophysical topics. With your continuous support and constructive advice, I was able to achieve my academic goals.

Special thanks to my committee members, Dr. Brett M. Carpenter and Dr. Matthew J. Pranter, for the recommendations I received during the proposal, classes, and meetings. I want to extend my gratitude to Dr. Kurt J. Marfurt for the helpful and insightful suggestions. I really appreciate your comments and observations that contributed to my learning process.

I appreciate being part of the Subsurface Detective Agency (SDA) and Attribute-Assisted Seismic Processing & Interpretation (AASPI) teams. The weekly meetings were great moments to discuss and collaborate. Many thanks to Jose Pedro Mora Ortiz, Alexandro Vera Arroyo, Ahmet Murat Alyaz, Karelia La Marca, Javier Tellez, David Lubo, Thang Ha, and Andrea Damasceno for the discussions and suggestions that I received.

My sincere thanks also to the University of Oklahoma for all the essential equipment and laboratories. The pandemic made the journey even more challenging, and the support of many

professors, staff, and IT technicians helped me continue my studies. I also wish to thank Jessica A. Reynolds for helping to improve my English with your very engaging classes. Thanks to Mark J. Laufersweiler for helping to understand better some Python functions.

I am incredibly grateful to my wife Claudia and kids (Debora and Rafael) for everything you have done to help me achieve my goals. I know I can always count on you. Your presence, support, and love were fundamental to my happiness and success. I felt inspired and confident to pursue my objectives, being encouraged by my family and friends. I do not have enough words to describe how special you are to me. I thank all of you.

TABLE OF CONTENTS

ACKNOWLEDGEMENTS v

TABLE OF CONTENTS vii

LIST OF FIGURES x

LIST OF TABLES xviii

ABSTRACT xix

CHAPTER 1: INTRODUCTION 1

MOTIVATION 6

GEOLOGICAL FRAMEWORK 7

Jubarte Field 10

SEISMIC ATTRIBUTES APPLIED FOR FAULT IDENTIFICATION 12

DATA AND METHODS 17

Seismic 17

Wells 21

WORKFLOW 24

REFERENCES 34

CHAPTER 2: SEISMIC ATTRIBUTES AND UNSUPERVISED MACHINE LEARNING TECHNIQUES APPLIED TO FAULT CHARACTERIZATION IN A POST-SALT RESERVOIR INTERVAL, JUBARTE FIELD (CAMPOS BASIN) 39

ABSTRACT 39

INTRODUCTION 41

Geological setting 45

Data and methods 46

SEISMIC ATTRIBUTES AND STRUCTURAL INVESTIGATIONS 48
MACHINE LEARNING IN GEOPHYSICAL STUDIES 51
RESULTS 53
Data conditioning 53
Instantaneous attributes 55
Curvature attributes 57
Similarity attributes 60
Frequency-based analysis 62
DISCUSSIONS 66
CONCLUSIONS 68
ACKNOWLEDGMENTS 69
REFERENCES 70
CHAPTER 3 – COMBINING AZIMUTHAL VOLUMES, ENERGY-RATIO ATTRIBUTE, AND MACHINE LEARNING TO INVESTIGATE FAULTS IN THE JUBARTE FIELD, CAMPOS BASIN 80
SUMMARY 80
INTRODUCTION 81
GEOLOGICAL SETTING 83
DATA AND METHODS 84
RESULTS 86
DISCUSSIONS AND CONCLUSIONS 91
ACKNOWLEDGMENTS 92
REFERENCES 93

CHAPTER 4 – DISCUSSIONS AND CONCLUSIONS 97

FUTURE WORK 104

REFERENCES 105

APPENDIX A – Example of well tie 106

APPENDIX B – Reflectivity analysis using well logs 110

APPENDIX C – Comparison of different spectral balancing factors 112

APPENDIX D – Computation of dip attribute and the results for different parameters 113

APPENDIX E – Comparison between a vertical section before and after spectral balancing and application of Ormsby Filter. 115

APPENDIX F – Examples of parameters used to compute the structure-oriented filtering (SOF) and an additional comparison 116

APPENDIX G– Comparison between different instantaneous attributes computed after data conditioning 118

APPENDIX H – PCA results for instantaneous attributes 121

APPENDIX I - SOM results for instantaneous attributes 122

APPENDIX J – Comparison between different curvature algorithms and parameters 123

APPENDIX K – Comparison between short and long wavelengths operator 124

APPENDIX L - SOM results for instantaneous attributes 125

APPENDIX M – PCA results for different windows of observations 127

APPENDIX N – Comparison between the PCA results, considering the first and second principal components 128

APPENDIX O – PCA results (original amplitude volume vs. energy-ratio attribute) 129

LIST OF FIGURES

Figure 1. 1 - (A) Examples of changes in seismic traces that can reveal the presence of faults. Common indications are related to offset reflections, change in dip, change in signal-to-noise ratio, and change in amplitude/phase. From Hart (2011). (B) Lateral changes in the continuity of seismic reflectors (reflector offset) associated with a smaller fault system. From Chopra et al. (2000). (C) Example of a fault zone (red arrows) in the Jubarte Field. (C) Another example from the study area, but now the discontinuity is marked by subtle variations that make more difficult the recognition of a fault system. 2

Figure 1. 2 – Geological chart representing a profile along the Campos Basin, characterized by three sequences (non-marine, transitional, and marine) and three sectors (shallow, deep, and ultra-deep waters). Note the impact that faults have on hydrocarbon distribution in post-salt reservoirs (Mohriak et al., 2012). 4

Figure 1. 3 – Cross-section showing the principal geological units in the Jubarte Field. Note the impact that faults have on the southeastern termination of the Maastrichtian deposits (Fontanelli et al., 2009). Vertical axis unit: meter. 5

Figure 1. 4 – A representative vertical seismic section (full-stack data). Yellow arrows point discontinuities observed in regions with strong acoustic impedance contrast. The red boxes indicate areas below the post-salt reservoirs where the identification of fault continuity is difficult due to seismic noise and weak amplitude. The vertical section is displaying 900ms of time. 6

Figure 1. 5 – Location of the Jubarte PRM seismic acquisition, situated offshore in the northern part of Campos Basin. The Jubarte PRM survey is located 77 km offshore from Espírito Santo State coast. 7

Figure 1. 6 – Stratigraphic chart of the Campos Basin with the three evolution phases: rift, post-rift, and drift. The interval of interest corresponds to the Maastrichtian section (red box). The source unit (Coqueiros Formation), seal (Ubatuba Formation), and post-salt reservoir (Carapebus Formation) are indicated. Modified from Winter et al. (2007) and Castro & Picolini (2015). 8
Figure 1. 7 - Optical photomicrograph of a poorly sorted sandstone. Note the intense variation of the grain fragments. From Fontanelli et al. (2009). 11
Figure 1. 8 - Examples of attributes used to enhance the visualization of changes in the original seismic dataset. Dip, curvature, and aberrancy attributes correspond to the first, second, and third derivatives. From Bhattacharya and Verma (2019). 15
Figure 1. 9 – Curvature attribute commonly applied for structural studies. Note the possibilities that this attribute can assume: zero, positive and negative values. Depending on the degree of the surface change, higher curvature (small circle) or lower curvature components (larger circle) can better describe the changes in the reflector shape. From Chopra and Marfurt (2007b). 16
Figure 1. 10 – Comparison between the partial stacks related to Monitor-01 acquisition. The analysis window corresponds to the interval of interest, and it was limited vertically and horizontally (inline and crosslines numbers: 2350-2530). 19
Figure 1. 11 – Vertical section displaying the amplitude volume (white and black color bar) and the velocity model (colored bar). The higher and lower velocities will be considered for the computation of maximum and minimum vertical resolution, respectively. 20
Figure 1. 12 – Checkshot points from wells B, C, and Q. Note the velocity variations close to Maastrichtian reservoirs, as indicated with the black brace. 22
Figure 1. 13 - Example of the well tie in Well Q. Display of the log curves: caliper, gamma-ray, resistivity, density, P-wave, S-wave. The top of the Cretaceous represents a regional surface used

to initiate the correlations. To generate this seismogram was initially adopted by a statistical wavelet, complemented with phase adjusted based on the logs. The vertical section is displaying 400ms of time. 23

Figure 1. 14 – General aspect of the post-salt section (Monitor-01 full-stack). Left panel: time slice along the reservoir with the position of four wells used in this project. Note the abrupt limit of some amplitudes demonstrating the presence of Fault 1. In a map view, the recognition of Fault 2 is not so evident as Fault 1. Right panel: vertical section revealing the two mentioned faults, the reservoir interval, top of Cretaceous reflector, and more evident noise below the reservoir (dashed line). Vertical exaggeration: 2x..... 25

Figure 1. 15 – Original amplitude section with and without interpretation of some features of interest. Two faults can be interpreted (orange lines) based on the reflector's lateral continuity changes. Close to the edge of the survey is possible to see seismic noise (yellow arrows) that, in critical cases, can interfere in fault recognition (red arrows). Vertical exaggeration: 2x. The vertical section is displaying 1070ms of time..... 26

Figure 1. 16 – Original amplitude section with and without interpretation of some features of interest. It is possible to see two faults (orange lines) based on the reflector's lateral continuity changes. Close to the edge of the survey occurs dipping events (yellow arrows) that correspond to seismic noise and can affect the recognition of faults (red arrows). Vertical exaggeration: 2x. The vertical section is displaying 970ms of time..... 27

Figure 1. 17 – Vertical section with the amplitude volume (red-white-blue color) corendered with similarity attribute. It is possible to see that low similarity values will be associated with faults (green arrows), chaotic deposits (yellows box), and seismic noise (orange box)..... 28

Figure 1. 18 – Vertical section comparing the original amplitude volume (red-white-blue color) and the difference between the energy-ratio attribute computed from Monitor-01 and Monitor-02. The noise below the reservoir (orange box) can be noted in both surveys and is more intense than the adjacent units..... 29
Figure 1. 19 – NRMS map between Monitor-01 and Monitor-02 PP full-stack volume, computed using a 200 ms time window below the base of the depositional system. The histogram was estimated inside the black polygon because datasets are more impacted by artifacts close to the edges of the survey,..... 30
Figure 1. 20 – Workflows defined to improve the identification of faults zones in seismic. Three main phases can be recognized: data conditioning attributes computation and machine learning. 31

Figure 2. 1 – (A) Location of the Campos Basin in the eastern Brazilian margin and the (B) Jubarte PRM system positioned offshore of the Espírito Santo coast. (C) Time slice of the original full-stack amplitude data. Note the presence of two faults marked by changes in amplitude. (D) Vertical section close to Well B, where it is possible to see two discontinuities. Blue boxes indicate an interval below the post-salt reservoir with weak amplitude contrasts. Vertical exaggeration:2x. The vertical section is displaying 1250ms of time..... 44
Figure 2. 2 – Comparison between the original amplitude volume (A) and the same vertical section after the application of spectral balancing, Ormsby filter, and structure-oriented filtering (B). Yellows arrows indicate discontinuities more clearly observed after the data conditioning. Red boxes indicate regions where seismic noise elements (undulating features) were attenuated. The blue box and the green arrows show improvements in the lateral continuity of reflectors. 54

Figure 2. 3 – Comparison between the amplitude volume after the data conditioning (upper left figure) with different instantaneous attributes. Two faults are indicated with the green and yellow arrows. Better results for fault recognition are observed with the cosine of instantaneous phase attribute. A description of different aspects of these attributes is in the text. The vertical section is displaying 600ms of time. 56

Figure 2. 4 - Comparison between the amplitude volume (post data conditioning) and the most-positive (k1) and most negative curvature (k2), obtained with short (left) and long-wavelength operators (right). Yellow arrows indicate more vertical faults observed close to the top of the reservoir. The green arrows show areas where the discontinuities have a lower dip angle, and the curvature attribute couldn't delineate the fault geometry completely (stair-step features). The orange box demonstrates the interval with weak impedance contrast, where seismic noise was enhanced with short wavelengths. The vertical section is displaying 350ms of time. 58

Figure 2. 5 – Comparison between short and long-wavelengths (λ) used to compute curvature most -positive (k1) and most-negative (k2) components. Upper part: time slice with long-wavelength demonstrating two faults, also visible in the vertical section (yellow and green arrows). Short-wavelength reveals localized features such as noise and stratigraphic terminations (orange arrow). 59

Figure 2. 6 – Comparison between the seismic dataset (after data conditioning) with Sobel filter and energy ratio similarity attributes. Note the sharp termination of features with low similarity in energy ratio (right figure)..... 60

Figure 2. 7 – Comparison between the original amplitude volume (full-stack, Monitor-01) and the Sobel filter, outer-product, and energy-ratio attributes. The attributes were computed using the filtered volume after the application of the SOF algorithm. The energy-ratio attribute resulted in

more sharp discontinuities compared to Sobel filter results, as indicated with the green arrows. On the other hand, the Sobel filter attribute helped reveal local features, such as the ones indicated with the orange arrows. 61

Figure 2. 8 – Vertical section comparing the original amplitude volume (full-stack, Monitor-01) with the energy-ratio similarity attribute with different frequency volumes. The broadband cube reveals better the fault geometry compared. Well is projected about 115 m from its position. ... 63

Figure 2. 9 – PCA results for similarity attributes, including multi-spectral, broadband volumes, and ten frequency cubes for each similarity attributes (energy-ratio, Sobel filter, and Outer product). Input includes 36 volumes. The volumes with higher variability include multi-spectral and broadband volumes. 63

Figure 2. 10 – Comparison between the original amplitude volume and SOM in a time slice (left) and vertical section (right). The green and red arrows indicate fault planes described by specific neurons (orange color in the 10x10 topology). 64

Figure 2. 11 – Comparison between the original amplitude volume (upper left) and the SOM classification (upper right) using a time slice. The discontinuity indicated in SOM colored in red is associated with a subtle change in the reflector's lateral continuity. Using the original amplitude volume is difficult to recognize this feature in a time slice (green arrow). SOM anomaly could reflect a subtle fault. The orange arrows indicate a possible vertical continuation of this subtle fault. 65

Figure 3. 1 – Left: Location of the Campos Basin along the eastern Brazilian margin. After Milani et al. (2007). Right: Position of the Jubarte PRM seismic acquisition, offshore Brazil. 81

Figure 3. 2 - (A) Comparison of the azimuth stack sectors and the full azimuth stack volume. Full azimuth stack volume has a broader spectrum compared to individual azimuth data sets. (B)

Azimuthal sectors and associated angle range and center angle (Barros, 2005, processing report). 85

Figure 3. 3 – Comparison between the energy-ratio similarity attribute computed with the full azimuth stack volume (upper vertical section) and individual azimuth sectors (45-225º; 90-270º; 135-315º, and 0-180º). The full azimuth stack volume has less seismic noise, and it is easy to identify the fault (yellow arrows). The vertical section is displaying 1400ms of time. 86

Figure 3. 4 – Comparison between the energy-ratio similarity attribute computed with the full azimuth stack volume (upper time slice) and the individual azimuth sectors. The yellow arrows show regions where the full-stack azimuth results in more linear features. Arrow with other colors demonstrate improvements obtained locally for each azimuth sector (red for 0-180º, green for 45-225º, white for 90-270º, and orange for 135-315º). 87

Figure 3. 5 – (A) Comparison between the full azimuth stack and individual azimuth sectors. The ERS attribute is displayed using black and white color bar in the time slice, while the seismic amplitude stacks are shown in the vertical slice. The yellow arrow exemplifies a fault segment where it is possible to see a more rectilinear and uniform discontinuity. Additional arrows demonstrate improvements obtained locally for each azimuth sector (green for 45-225º, white for 90-270º, and orange for 135-315º). (B) PCA results for the first principal component. The higher contribution is defined by the ERS attribute computed with the full-stack azimuth volume. 89

Figure 3. 6 – (A and B) Comparison between the original amplitude volume and SOM in a time slice. The black arrows indicate a fault. (C) Vertical section displayed in A and B with the location of the analyzed fault. (D) Another vertical section comparing the original amplitude volume (black and white color bar) and SOM results (8x8 topology). Note that the selected neurons indicate a

fault plane within the reservoir (red arrow) and minor stratigraphic termination (brown arrow). The same vectors are also associated with seismic noise components in the interval below. 90

Figure 4. 1 - Comparison between a time slice and vertical section using the original amplitude volume (left) and the energy-ratio attribute (right). The fault is easily observed with the energy-ratio attribute and is also possible to interpret with more confidence close to the base of the depositional system (green arrow). The vertical section is displaying 400ms of time. 99

Figure 4. 2 – Curvature attributes (most-positive and most-negative components) and energy-ratio similarity attribute computed at the top of the Cretaceous horizon. An eight ms window was used to obtain the values similarity and curvature values. The energy-ratio attribute defined the major discontinuities. The lateral extension of some discontinuities can be complemented using curvature computed with short-wavelength (yellow arrows show the possible extension of the structures). 100

LIST OF TABLES

Table 1. 1 - General information related to the Jubarte PRM acquisition and processing. From Barros (2015, processing report)..... 19

Table 1. 2 - Four well used to calibrate the seismic and logs. 22

ABSTRACT

Seismic reflection datasets represent an important source of information capable of revealing structural features in the subsurface, such as fault zones. Faults can be interpreted using the original amplitude volumes, especially when blocks of rocks have moved dozens or hundreds of meters relative to each other. One of the seismic characteristics that contribute to fault recognition is the presence of significant acoustic impedance contrasts in the faulted sedimentary layers. However, the recognition of subtle discontinuities represents a more challenging task when performed in intervals with a low signal-to-noise ratio and weak contrasts of acoustic properties. In these cases, seismic attribute analysis can enhance structural mapping. Seismic attributes are different measurements of the original seismic components, such as amplitude and phase. These attributes are routinely applied to highlight geological features of interest, not only for structural studies but also for stratigraphic analysis.

This research aims to compare instantaneous and geometric attributes (with different spectral components and azimuth volumes) to define what improvements can be obtained for fault characterization. The southeastern part of the post-salt section in the Jubarte Field (Campos Basin) represents the area selected to evaluate the impact of different parameters. In that region, the implementation of a 4D/4C system called Jubarte PRM resulted in many seismic volumes associated with various surveys. The main input used within this research is the P-wave full-stack volume, but complementary investigations included different azimuth data sets. Four wells helped calibrate log curves and seismic cubes and generate synthetic seismograms to characterize the Maastrichtian reservoir response.

Data conditioning represents a significant step to prepare the datasets to compute seismic attributes. Spectral balancing and structure-oriented filtering (SOF) are algorithms applied in this

initial phase. Attenuation of random seismic noise, enhanced visualization of stratigraphic reflectors, and more visible faults (higher contrasts with relation to the background) are examples of improvements obtained with the data conditioning.

The computation of most attributes requires specific parameters. For instance, curvature components are estimated using different algorithms (structural vs. amplitude) with short or long operators. The results show that different attributes can highlight distinct aspects of the seismic traces. For example, the cosine of instantaneous phase indicates discontinuities, and it is less affected by different amplitude contrasts. This attribute provides a uniform visualization of the discontinuities, keeping visible some additional features, such as stratigraphic elements. The energy-ratio attribute delineated discontinuities with sharper anomalies compared to other similarity attributes. Broadband volumes provide superior results for the delineation of non-vertical faults. The discontinuities' geometry is better defined using the entire amplitude spectrum than volumes composed by specific frequency ranges. Furthermore, comparisons using vertical sections and time slices demonstrate the benefits of having a full-stack azimuth data set (e.g., less seismic noise and more uniform fault segments). Individual azimuth sectors reveal small discontinuities, especially when oriented perpendicular to the acquisition direction. In short, I noticed after various tests that a multi-attribute approach was adequate for a more reliable and complete description of faults and fracture zones.

Unsupervised machine learning techniques complemented the analysis due to the larger number of volumes available and its sub-products (seismic attributes). I used principal components analysis (PCA) to identify the volumes with higher variability. Self-organizing maps (SOM) were included within the workflow to see if this clustering technique can delineate fault surfaces. Although the method has some limitations related to non-vertical discontinuities and noise

interference, it can improve and optimize the visualization of structural discontinuities as observed in the reservoir interval.

Lastly, it is necessary to check the results in all the steps because various methods can increase non-desired features such as seismic noise. Evaluation of the seismic features needs to be considered in-context interpretation to define the geological meaning for the structures described in seismic cubes. Overall, I noticed that an integrated investigation using data conditioning methods, different seismic attributes, and analysis of multiples volumes using unsupervised clustering methods improved the subsurface structural investigation of the Jubarte Field.

CHAPTER 1: INTRODUCTION

Seismic attributes are essential tools for interpretation activities, capable of providing critical insights into hydrocarbon reservoir management. Depending on the geological evolution of an area, some features can have more or less influence on the petroleum system elements. For instance, faults can create migration pathways. Discontinuities can also separate different flow units, and as a consequence, guide the proposition of injection and production wells. Rijks and Jauffred (1991) describe examples of how seismic attributes can improve the characterization of subtle faults and guide the field development strategy. For instance, dip and azimuth maps reveal faults, which were not observed previously in a southern North Sea field.

Changes in the waveform, amplitude, and phase components of the original signal, can indicate discontinuities in the subsurface (Marfurt et al., 1998a; Chopra et al., 2000; Al-Dossary and Marfurt, 2006; Hart, 2011; Iacopini, 2016). Changes in the dip of some reflections, variations of the signal-to-noise ratio, and local offsets are examples of features that interpreters consider when tracking a fault segment (Figures 1.1A and 1.1B). However, the recognition of faults could be more complicated in seismically noisy areas and regions with weak acoustic impedance contrasts (Figure 1.1C).

The objective of this study was to identify improvements to fault characterization using a variety of seismic attributes. The workflow consists of three main phases: data conditioning, attributes computation, and unsupervised machine learning analysis. A few motivational questions can be listed to describe in more detail the mentioned primary goal:

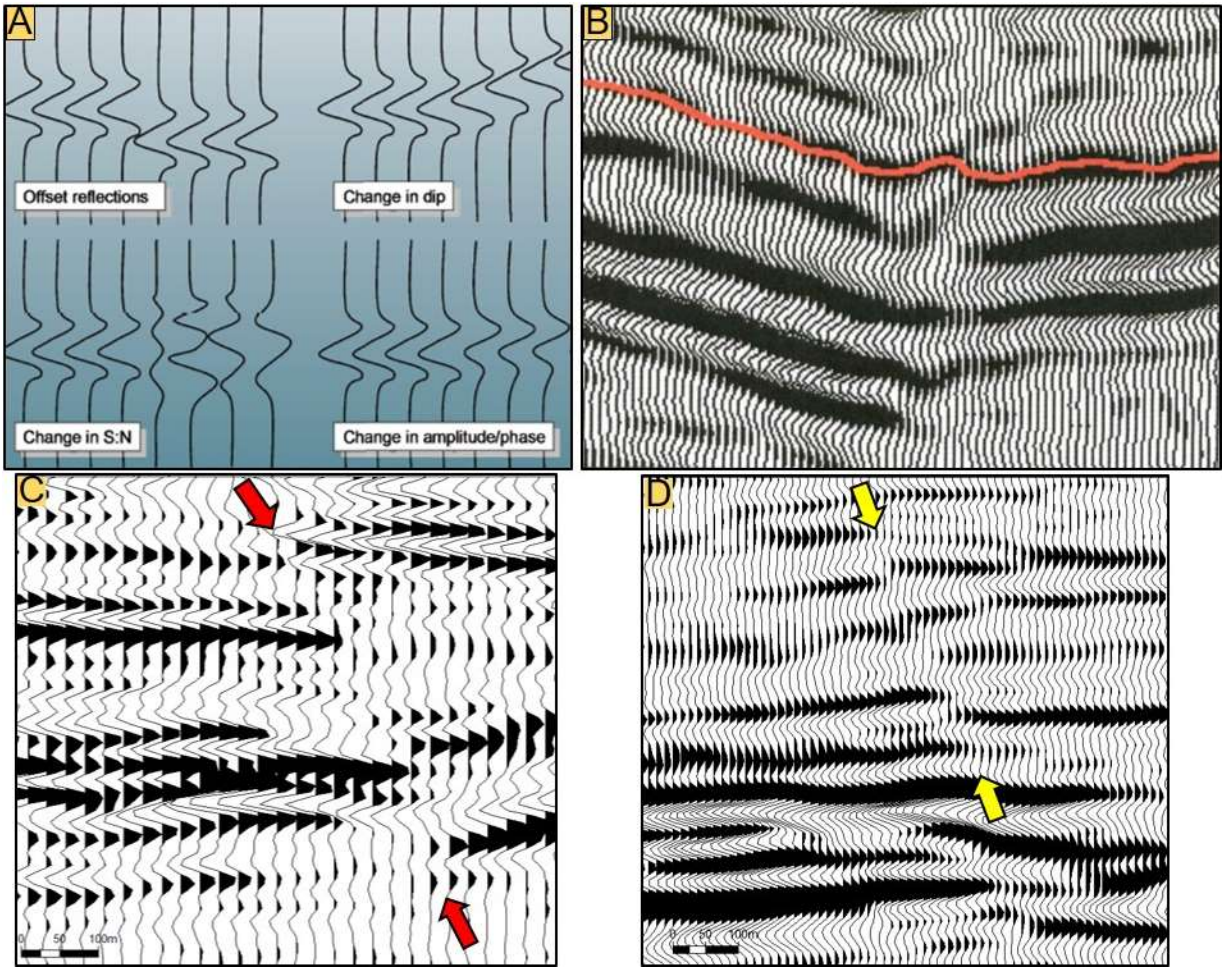


Figure 1. 1 - (A) Examples of changes in seismic traces that can reveal the presence of faults. Common indications are related to offset reflections, change in dip, change in signal-to-noise ratio, and change in amplitude/phase. From Hart (2011). (B) Lateral changes in the continuity of seismic reflectors (reflector offset) associated with a smaller fault system. From Chopra et al. (2000). (C) Example of a fault zone (red arrows) in the Jubarte Field. (C) Another example from the study area, but now the discontinuity is marked by subtle variations that make more difficult the recognition of a fault system.

► What methods can be applied during the data conditioning phase to improve the recognition of faults?

► Which seismic attributes better delineate faults and fractures?

► Is it better to use the entire amplitude spectrum or a specific frequency range?

► What are the interpretational impacts of different azimuthal sectors?

► Do principal component analysis (PCA) and self-organizing maps (SOM) provide additional insights into the traditional seismic interpretation methods?

Faults are important elements to understand the geological evolution of the Campos Basin. A representative regional geological chart demonstrates the relation that faults and oil distribution have in the post-salt section (Figure 1.2). This figure shows that faults also control the distribution of many turbidite deposits within the marine sequence. Some faults have significant displacements (orange arrows), and on the other hand, some fault systems display small displacements between adjacent fault blocks (black arrow). Salt movements created extensional and compressional structures in different parts of the eastern Brazilian margin (Davison, 2007). The figure also shows older faults affecting the basement and source rocks within the non-marine sequence.

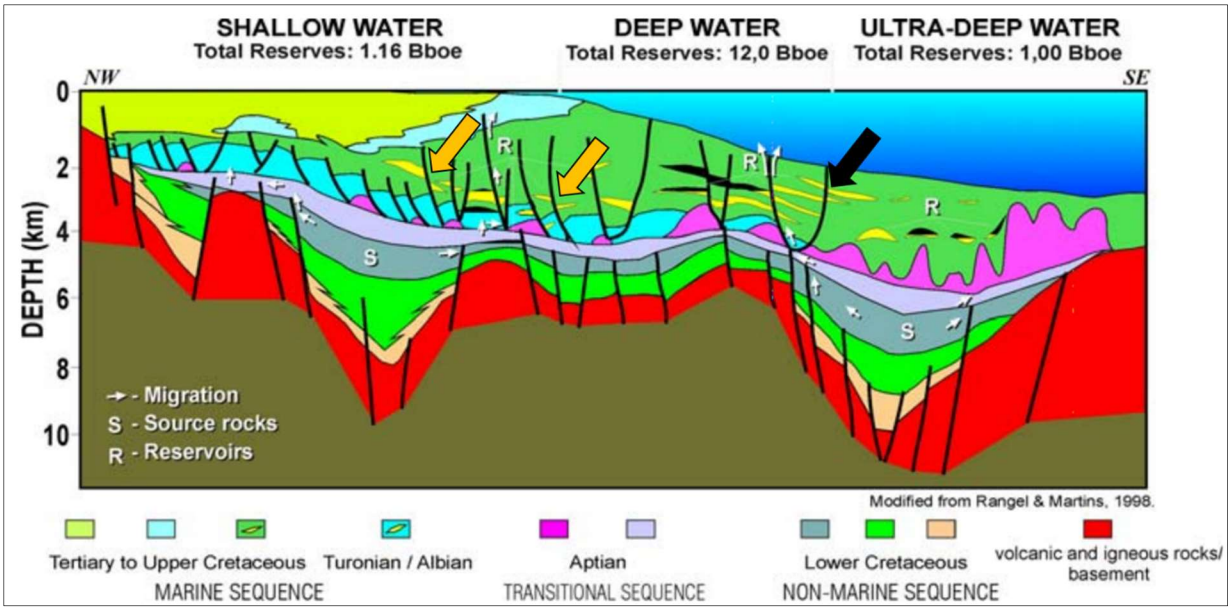


Figure 1. 2 – Geological chart representing a profile along the Campos Basin, characterized by three sequences (non-marine, transitional, and marine) and three sectors (shallow, deep, and ultra-deep waters). Note the impact that faults have on hydrocarbon distribution in post-salt reservoirs (Mohriak et al., 2012).

On a local scale, it is also possible to see the importance of faults and fracture zones in the Jubarte Field (Figure 1.3). The cross-section reveals a fault that limits the eastern portion of the field. In some areas, the fault juxtaposes reservoirs against non-reservoir units (orange arrows). However, it is also possible to see that sandstones can be linked to another sandstone (black arrows). Bezerra et al. (2004) also recognize the importance that this structure has within the Jubarte Field. Thedy et al. (2011) mention subtle faults that are difficult to recognize using 3D seismic in the study area. According to Thedy et al. (2011), these subtle discontinuities may not

disconnect blocks but can affect production. Waterfront moving can be observed within hanging and footwall blocks when the sandstones are connected (Thedy et al., 2015).

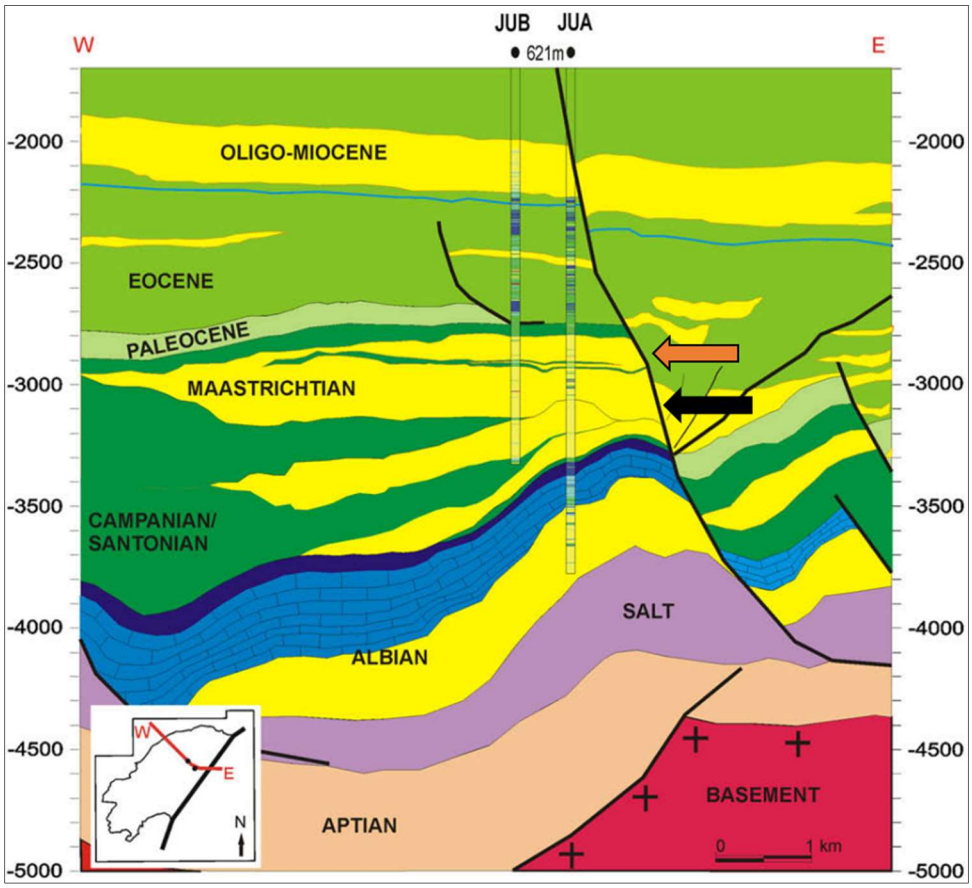


Figure 1. 3 – Cross-section showing the principal geological units in the Jubarte Field. Note the impact that faults have on the southeastern termination of the Maastrichtian deposits (Fontanelli et al., 2009). Vertical axis unit: meter.

The Maastrichtian section was examined in more detail because it includes sandstone reservoirs with faults and fractures impacting the seismic reflectors' lateral continuity. I presented more details on that within the next section.

MOTIVATION

A representative vertical section of the study area reveals that the seismic response of fault zones varies (Figure 1.4). The seismic expression depends on geological characteristics (e.g., composition), the reflector's location (shallow *vs*. deep interval), and the processing techniques applied during the data preparation. In the study area, it is easier to identify faults close to the reservoir's top and top of Cretaceous, regions with strong acoustic impedance contrasts, as indicated with the yellow arrows. However, areas composed of shales and mudstones contain weak impedance contrasts and more seismic noise (red boxes). These difficulties associated with the faults' recognition motivated the present study.

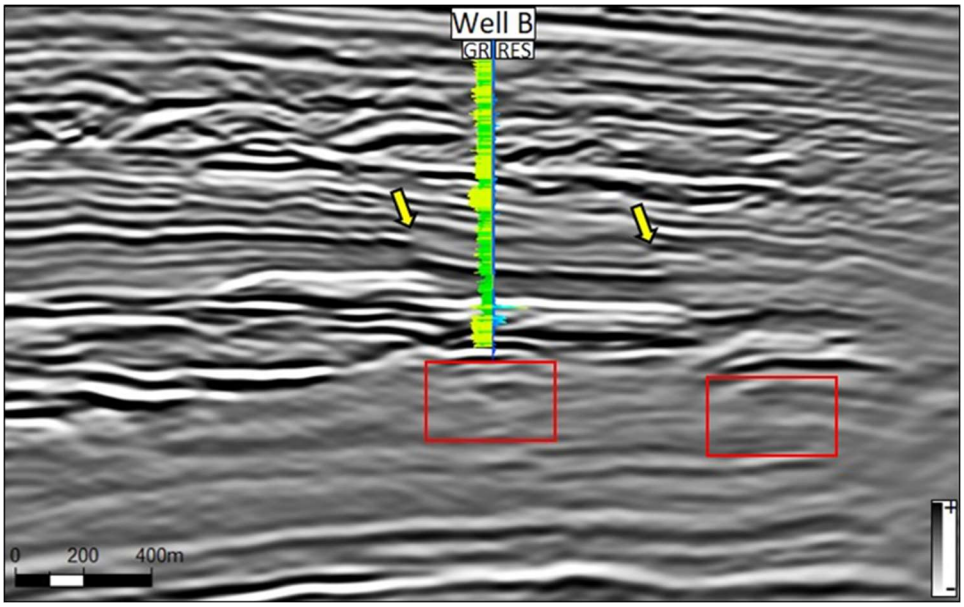


Figure 1. 4 – A representative vertical seismic section (full-stack data). Yellow arrows point discontinuities observed in regions with strong acoustic impedance contrast. The red boxes indicate areas below the post-salt reservoirs where the identification of fault continuity is difficult due to seismic noise and weak amplitude. The vertical section is displaying 900ms of time.

GEOLOGICAL FRAMEWORK

The study area is located offshore in the eastern Brazilian margin, in the northern part of Campos Basin (Figure 1.5). The regional evolution is related to the break-up of Gondwana and involved different phases (Guardado et al., 1997; Delgado et al., 2018). This research considers the three main phases described by Winter et al. (2007): rift, post-rift, and drift (Figure 1.6).



Figure 1. 5 – Location of the Jubarte PRM seismic acquisition, situated offshore in the northern part of Campos Basin. The Jubarte PRM survey is located 77 km offshore from Espírito Santo State coast.

The rift phase was marked by diachronic deformation processes that generated faults and grabens. Some of the major faults (oriented parallel to the coast) are segmented locally by transfer zones. Next, a post-rift sequence deposited during the Aptian was associated with thermal subsidence processes. The drift stage of evolution was marked by the formation of an oceanic crust

and included a significant contribution of sediment load mechanism during full marine settings (Milani et al., 2007).

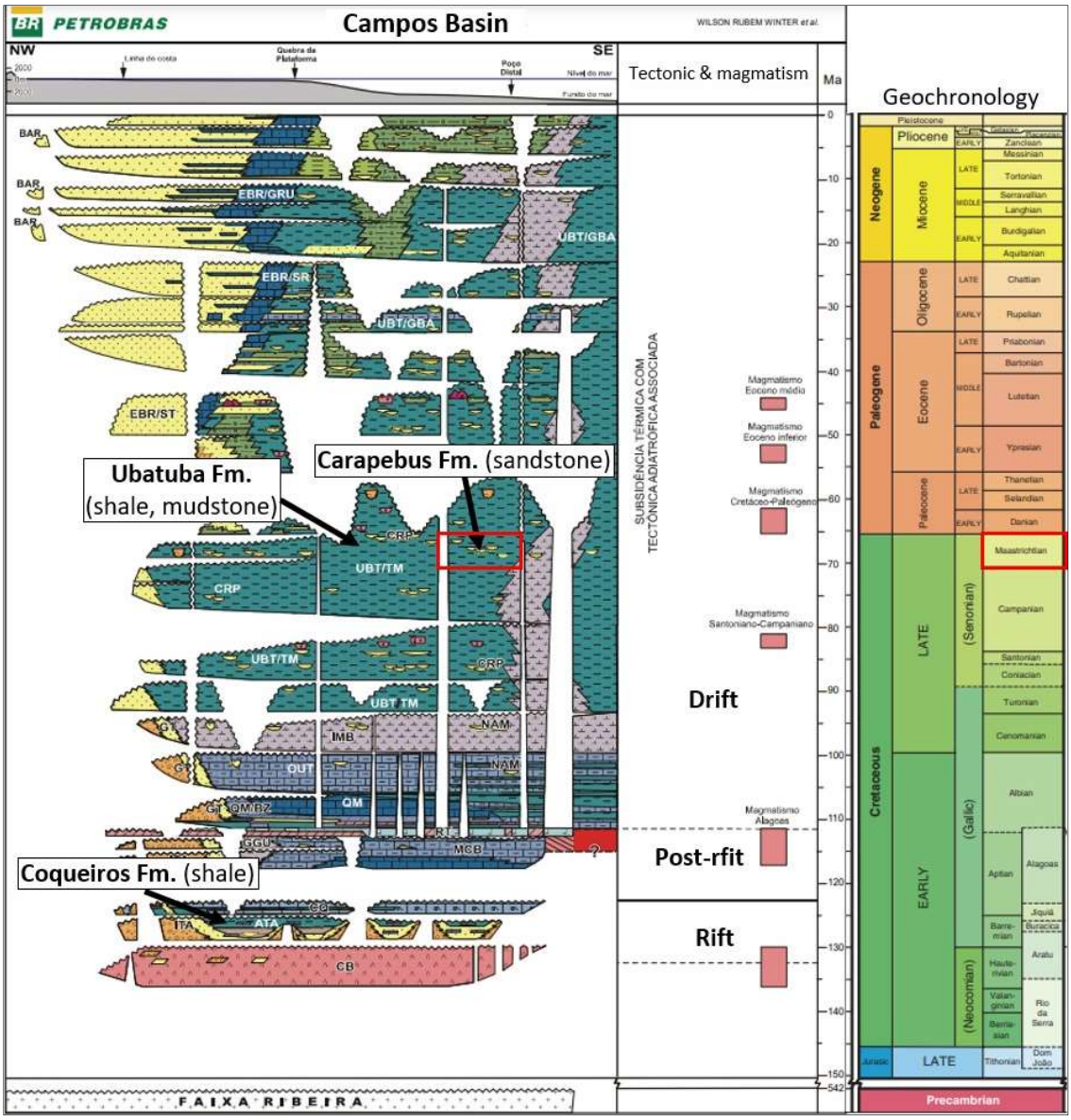


Figure 1. 6 – Stratigraphic chart of the Campos Basin with the three evolution phases: rift, post-rift, and drift. The interval of interest corresponds to the Maastrichtian section (red box). The source unit (Coqueiros Formation), seal (Ubatuba Formation), and post-salt reservoir (Carapebus Formation) are indicated. Modified from Winter et al. (2007) and Castro & Picolini (2015).

Regarding the petroleum system, the reservoirs are formed by post-salt deposits (Carapebus Formation), and the seal is composed of shales and mudstones (Ubatuba Formation) included in the drift phase of the evolution. Lacustrine shale represents the source rocks deposited during the rift phase (Coqueiros Formation), as described by Winter et al. (2007). Fault zones deformed these geological units. In many cases, the modification imposed by salt movements is associated with structural traps, as observed with NE-SW faults in Jubarte Field (Dariva et al., 2016).

Considering the structural control, the main features described in the basement are normal faults with antithetic and synthetic segments, strike-slip faults, horsts, and grabens (Fontanelli et al., 2009; Castro and Picolini, 2015). Also, homoclinal and roll-over structures were observed (Delgado et al., 2018). Regarding the interval of interest, halokinesis created faults and reactivated structures, as observed in the regional geological chart (Figure 1.2). Major faults oriented NE-SW and small discontinuities aligned NW-SE occur (Fontanelli et al., 2009). A significant discontinuity is the Jubarte Fault (oriented NE-SW), which in conjunction with other features, controls the sandstones' distribution as observed in Figure 1.4.

Seismic methods have been applied in the Campos Basin for different goals, mainly regional studies and detailed analysis applied to characterize reservoirs. For instance, Davison et al. (2012) describe the advantages of using a reverse time migration (e.g., acceptance of extreme lateral velocity variations) to analyze complex structures related to salt movement. On the other hand, these authors also mention some limitations associated with vertical resolution and amplitude preservation. The recognition of the oil-water contact within turbiditic sandstone reservoirs in the Bicudo Field is marked by amplitude contrast related to the fluid effect, also

supported by modeling investigations (Rosa et al., 1985). This is one example of how seismic reflection data can be used to evaluate hydrocarbons' occurrence in the subsurface.

Jubarte Field

The field is situated 77 km offshore from Espírito Santo State coast, in a region with water depths between 1,200 and 1,300 m. The post-salt oil field was discovered in 2001 (Dariva et al., 2016; Balabekov et al., 2017), and the oil production started in 2006 (Thedy et al., 2011). Regarding the pre-salt targets, production started in 2008 (Batalha and Cunha, 2018; Roberto et al., 2018). Pre-salt production in the Jubarte Field corresponds to Brazil's fourth-largest petroleum production (ANP, 2021, monthly bulletin).

Daher Jr. et al. (2007) discuss textural and mineralogical aspects and petrophysical properties of the Maastrichtian reservoirs. In general, the deposits include poorly-sorted, very coarse-grained to fine-grained sandstones, with moderate to poor consolidation and feldspathic composition (Fontanelli et al. 2009; Balabekov et al., 2017). The variability of the grain size and the presence of angular and sub-angular grains reveal the immature signature of the deposits (Figure 1.7). Gontijo et al. (2005) describe the dimension of the elements involved during the deposition of the turbidites, such as the size of the trough (8 – 14 km) and its width (1.5 - 5.5 km). Individual channels were defined as being 150 – 300 m wide and 30-50 m deep. Gontijo et al. (2015) describe angular to sub-angular clasts and organic matter fragments within massive and cross-bedded sandstones.

The deposits were formed during a transgressive mega-sequence (Del Rey et al., 2012), and it is possible to recognize two main source areas (southwest and northwest) with different

provenance signatures (Fontanelli et al., 2009). The 350 m-thick deposit comprises turbidites and mudstones with high net-to-gross ratios (73%) (Bezerra et al., 2004). Porosity and permeability average values are 23-26% and 800-1,200 mD (Colodette et al., 2007; Thedy et al., 2011; Dariva et al., 2016). The hydrocarbon has a heavy oil signature with 17.1° API (Del Rey et al., 2012) that required special operations to improve production (Bezerra et al., 2004; Tarcha et al., 2016; Roberto et al., 2018).

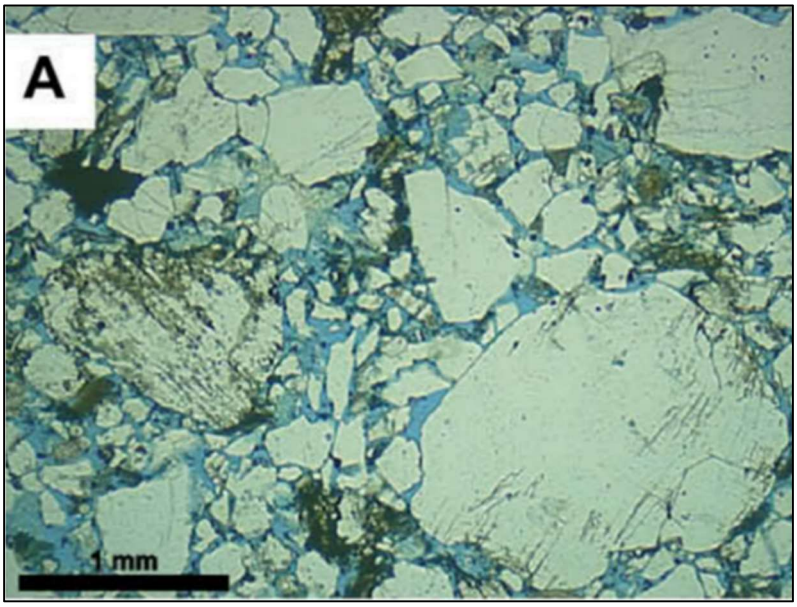


Figure 1. 7 - Optical photomicrograph of a poorly sorted sandstone. Note the intense variation of the grain fragments. From Fontanelli et al. (2009).

Besides stratigraphic elements of the reservoirs, recent publications also discuss other aspects of the Jubarte Field. Dariva et al. (2016) describe changes in the seismic amplitude related to production. Factors controlling changes in the 4D response are related to water saturation changes, variations of pressure close to injector wells, and noise (Dariva et al., 2016).

Balabekov et al. (2017) demonstrate results using pre-stack Bayesian inversion to define the oil-water contact and contribute to an adequate reservoir management. For instance, it is possible to determine the probability of various properties (e.g., thickness, net-to-gross, porosity, oil saturation).

Damasceno (2020) represents an important contribution to seismic inversion studies. Improvements in 4D investigations are described using PP-PS inversion that helped quantify anomalies related to reservoir properties and fluid content. In addition, refinements were obtained considering the alignment of different partial stacks.

SEISMIC ATTRIBUTES APPLIED FOR FAULT IDENTIFICATION

The literature review demonstrates improvements for the identification of geological features that can be obtained based on various seismic attribute categories (Roden et al., 2015). The instantaneous and geometric attributes represent the classes of attributes evaluated in more detail within this study. One advantage of using different attributes is that different operations were implemented, and various concepts can be analyzed. Let's briefly analyze concepts associated with some instantaneous attributes.

The complex seismic trace is composed of two terms: the real and imaginary parts. Following Taner et al. (1979) notation, the real seismic trace f(t) is composed by time-dependent amplitude A(t) and the phase component θ(t) and can be indicated as:

$$f(t) = A(t)\cos\theta(t).$$

The Hilbert transform uses an operator that is applied to estimate the quadrature trace $f^*(t)$ that is responsible for generating a 90-degree phase-shift (Barnes, 2016; Rosa, 2018):

$$f^*(\mathrm{t}) = A(t)\, sin\theta(t).$$

Based on these components, Taner et al. (1979) demonstrate how we can estimate the reflection strength (or envelope) A(t), and the instantaneous phase θ(t):

$$A(t) = [f^2(t) + f^{*2}(t)]^{\frac{1}{2}},$$

$$\theta(t) = tan^{-1}\left[\frac{f^*(t)}{f(t)}\right].$$

These two measurements correspond to essential attributes within the instantaneous attribute class, with the instantaneous phase having more applicability for identifying faults. Instantaneous frequency $f_i(t)$ is an attribute that describes the sinusoid that best fits the seismic signal within a small windows analysis and can be more sensitive to high-frequency noise (Barnes, 2016). The instantaneous frequency is described as the time derivative of the instantaneous phase (Barnes, 2016):

$$f_i(t) = \frac{1}{2\pi}\frac{d}{dt}\theta_i(t).$$

The importance of the Hilbert transform can also be noted in the computation of other attributes, such as coherency *c* when computed using the semblance approach (Chopra and Marfurt et al., 2007a):

$$c_s(t,p,q) = \frac{\sum_{k=-K}^{+K}\left\{\left[\sum_{j=1}^{J} u_j\left(t + k\Delta t - px_j - qy_j\right)\right]^2 + \left[\frac{1}{J}\sum_{j=1}^{J} u_j^H\left(t + k\Delta t - px_j - qy_j\right)\right]^2\right\}}{\sum_{k=-K}^{+K}\frac{1}{J}\sum_{j=1}^{J}\left\{\left[\sum_{j=1}^{J} u_j\left(t + k\Delta t - px_j\right)\right]^2 + \left[u_j^H\left(t + k\Delta t - px_j - qy_j\right)\right]^2\right\}}$$

where u^H indicates the Hilbert transform, *J* denotes the number of traces centered about the analysis point, *t* is the time of an event, *p* and *q* are the apparent dips in the inline and crossline directions, *u* describes the data traces, and K represents the vertical analysis window. Coherency results will be dependent on the size and shape of the analysis window (Marfurt et al., 1998b; Liu et al., 2017)

and the presence of noise as discussed in Libak et al. (2017). The energy-ratio coherence, defined by the ratio of the coherent energy and the total energy, also considers the analytic trace, as demonstrated in Lyu et al. (2020).

Luo et al. (2003) describe a generalized Hilbert transform (GHT) based on the windowed Fourier transform (having different order exponents) that is less sensitive to noise and can be used for different applications. Using 3D data, they demonstrate how this modification can improve the recognition of channels and faults. The relevance of the analytic trace can also be noted in the computation of the amplitude volume transform attribute - AVT (or TecVA in Portuguese). The inverse Hilbert transform is applied after the window-based RMS amplitude estimation, as presented by Bulhões and Amorin (2005).

I described until now some attributes and how they are related to the Hilbert transform. Another appropriate way to introduce the importance of seismic attributes for structural investigations is to use a visual representation of other geometric elements (Figure 1.8). It is possible to see in the upper part of this figure a surface y(x) that changes its shape laterally. The dip is one attribute defined by the first derivative of the initial surface that helps to identify the reflector's main variation. Curvature represents a first derivative in the inline and crossline components of the dip attribute (Chopra and Marfurt, 2013). Aberrancy corresponds to the third derivative and can also be applied for structural purposes, as demonstrated by Bhattacharya and Verma (2019). In many cases, faults can create subtle deformation within seismic horizons, as demonstrated in the upper curve y(x). The red vertical dashed line helps us see the differences that this feature can have a multi-attribute approach.

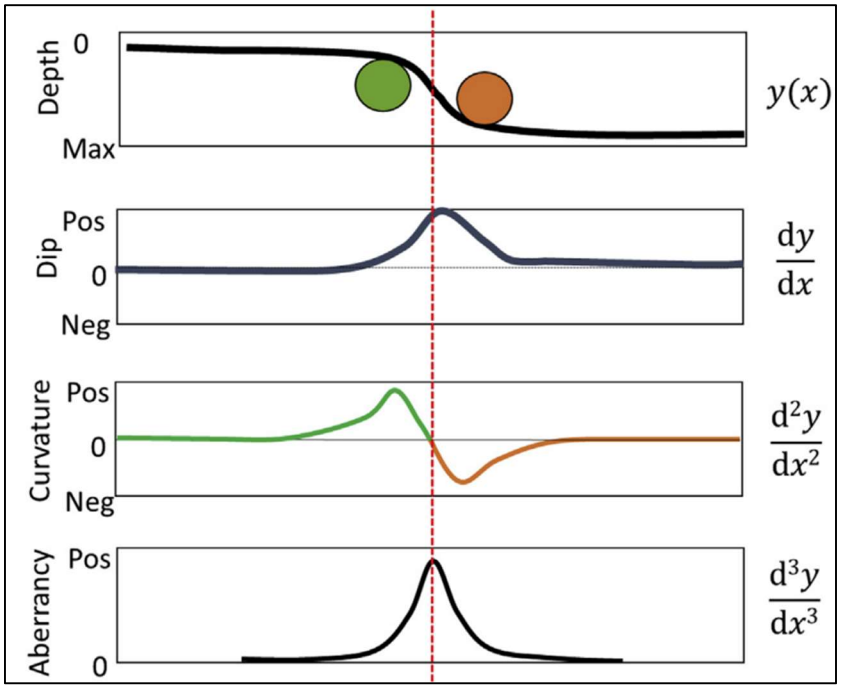


Figure 1. 8 - Examples of attributes used to enhance the visualization of changes in the original seismic dataset. Dip, curvature, and aberrancy attributes correspond to the first, second, and third derivatives. From Bhattacharya and Verma (2019).

When analyzed in more detail, the curvature attribute can be described by different components that show how bent a reflector or surface is at a specific point. It quantifies the rate of change of the direction of a curve and is reciprocal to the *radius* of curvature *K,* as K = 1/ R (Roberts, 2001). A smaller radius of curvature implies higher curvature values. This geometric attribute quantifies a surface's deformation at a specific point (Chopra and Marfurt, 2007b), as indicated in Figure 1.9. The most-positive and most-negative principal curvature components can also identify stratigraphic features (Chopra and Marfurt, 2007b).

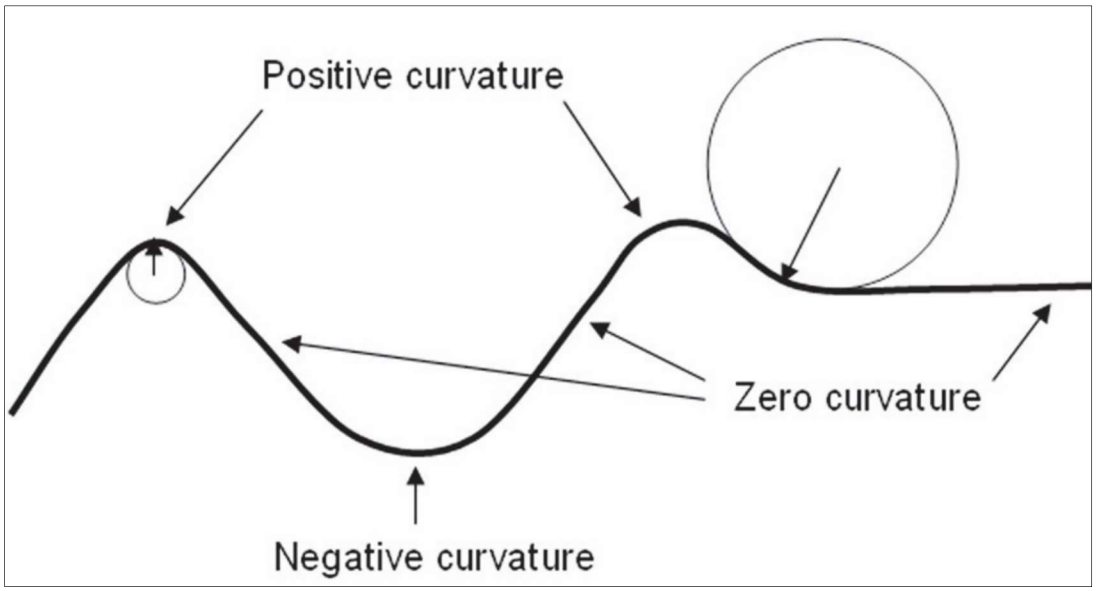


Figure 1. 9 – Curvature attribute commonly applied for structural studies. Note the possibilities that this attribute can assume: zero, positive and negative values. Depending on the degree of the surface change, higher curvature (small circle) or lower curvature components (larger circle) can better describe the changes in the reflector shape. From Chopra and Marfurt (2007b).

Based on the good results described in the literature, I opted to use most-positive and most-negative principal curvatures (k1 and k2) to investigate faults. These components can be estimated as:

$$k_1 = k_{mean} + (k_{mean}^2 - k_{Gauss}^2)^2,$$

$$k_2 = k_{mean} - (k_{mean}^2 - k_{Gauss}^2)^2,$$

where K_{mean} denotes mean curvature and K_{Gauss} describes Gaussian curvature. A more detailed description of the mean and Gaussian curvature components was presented by Roberts (2001).

After calculating many attributes, I evaluated the impact of these volumes for the characterization of fault zones. In addition, these attributes were compared using principal

component analysis (PCA) and self-organizing maps (SOM). At this phase, other operations become important such as the covariance matrix (S) used in the initial part of PCA studies, as demonstrated by Zhao et al. (2015) and in Liu et al. (2017):

$$S = \frac{1}{N}\sum_{n=1}^{N}(x_n - \bar{\mathrm{x}})(x_n - \bar{\mathrm{x}})^T,$$

where N describes the number of data points, $\bar{\mathrm{x}}$ denotes the mean vector of the data set, and T indicates the transpose matrix.

This section briefly demonstrated different methods that I selected to evaluate discontinuities using seismic datasets. The responses obtained with instantaneous attributes will be compared to geometric attributes to see what improvements can be made for structural investigations in the subsurface.

DATA AND METHODS

Seismic

The seismic volumes used in this research are associated with two surveys called Monitor-01 and Monitor-02, acquired by a Permanente Reservoir Monitoring (PRM) system positioned in the southeastern part of the Jubarte Field. The surveys were acquired with twelve month's interval, and the Monitor-01 was considered the reference one (Barros, 2015, processing report), guiding amplitude and phase adjusts of volumes from other surveys. Considering the seismic polarity, acoustic impedance increase (compression) is represented as a positive number. As a consequence, the top of the Cretaceous is indicated as a peak (black), and the top of the reservoirs correspond to a trough (white) related to an acoustic impedance decrease

The Jubarte PRM acquisition was proposed to improve the post-salt reservoirs' characterization and provide supplementary information to the geological models (Balabekov et al., 2017; Bruhn et al., 2017). In particular, oil-water flows and pressure changes are examples of variations expected to be monitored with the PRM system. One of the goals was to improve the recovery factor (Thedy et al., 2011).

The 4D project used sensors distributed along 11 receiver lines installed on the seafloor, separated by 300m. Each sensor is composed of three accelerometers and one hydrophone. The two surveys show great repeatability with an average NRMS value of 4 % (Thedy et al., 2015). Table 1.1 shows some aspects of the acquisition and processing.

I used PP post-stack files and partial stacks with different azimuthal distribution. Besides the full-stack azimuth volume, four individual azimuth data sets were investigated. The center angles correspond to 00-180º, 45-225º, 90-270º, and 135-315º. Each sector was migrated separately.

Figure 1.10 shows the amplitude spectrum of the different stacks (5-15, 10-25, 20-35, and 30-45 degrees) in the interval of interest using volumes from Monitor-01. The figure also compares the PP-wave and PS-wave volumes. The considered window of observation was limited in area and also in time. The PP-wave volume has a broader amplitude spectrum, and it was selected to be the primary data set to investigate the seismic attributes responses. The comprehension of the amplitude spectrum will also guide the application of frequency filters in the following steps.

Table 1. 1 - General information related to the Jubarte PRM acquisition and processing. From Barros (2015, processing report).

Recording system	PGS OptoSeis™ and gAS
Samples interval	2 ms
Number of sources	1 (Sercel G-Gun II)
Source air pressure	2000 psi
Shot interval and depth	25 m / 7 m
Receiver interval	50 m
Number of receivers (4C sensor stations)	712
Receiver depth (seafloor)	1240 – 1310 m
Final grid	12.5 m x 12.5 m
Processing resample	4 ms
Migration	3D pre-stack VTI Kirchhoff Depth Migration
Migration half aperture/offset range/offset increment	3000 m / 250 – 5950 m / 100 m

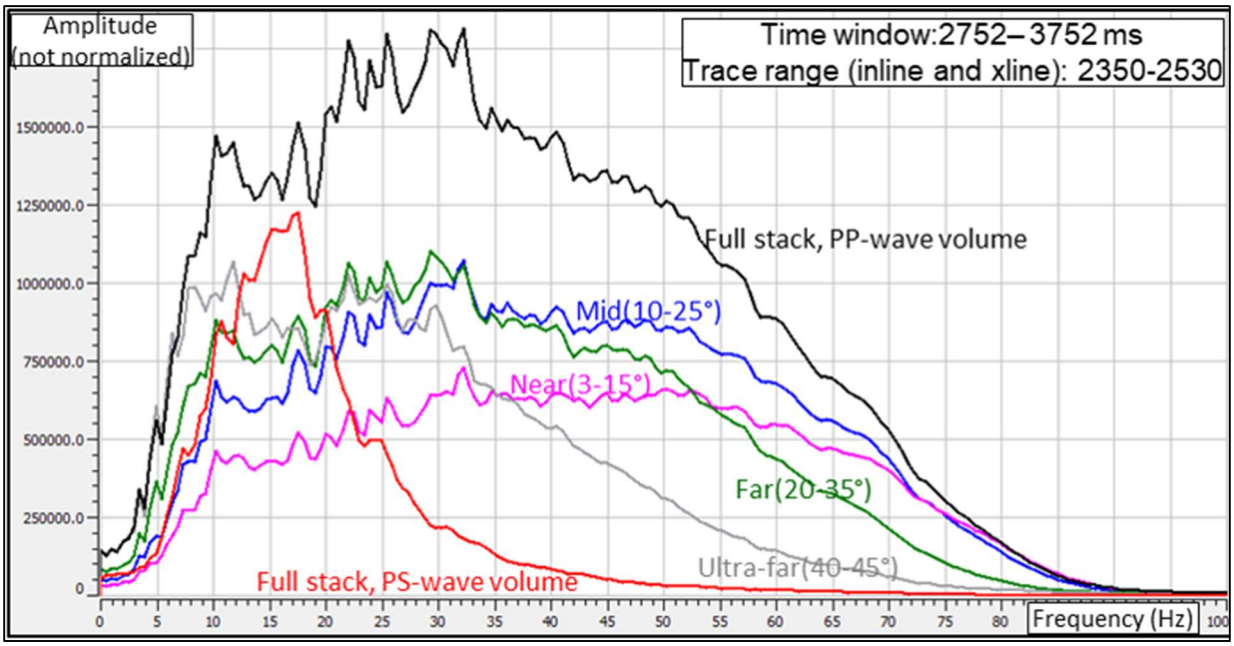


Figure 1. 10 – Comparison between the partial stacks related to Monitor-01 acquisition. The analysis window corresponds to the interval of interest, and it was limited vertically and horizontally (inline and crosslines numbers: 2350-2530).

The amplitude spectrum of the PP-wave full-stack volume also helped to estimate the vertical resolution. Considering the lateral and vertical variations of the frequency, I described the maximum and minimum resolution expected for the interval of interest. The velocities used to calculate the resolution were estimated above and below the reservoir (Figure 1.11).

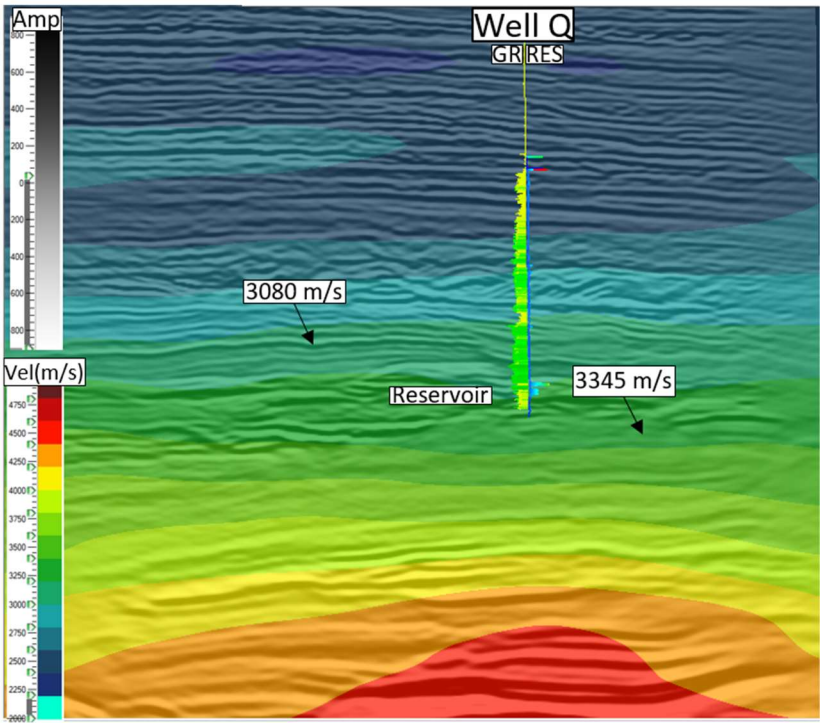


Figure 1. 11 – Vertical section displaying the amplitude volume (white and black color bar) and the velocity model (colored bar). The higher and lower velocities will be considered for the computation of maximum and minimum vertical resolution, respectively.

The higher vertical resolution is defined by the ratio of the minimum velocity and maximum dominant frequency. It corresponds to 19.2 m within the interval of interest (v = 3080

m/s and dominant frequency equal to 40 Hz). The lower vertical resolution is 41.8 m (v = 3345 m/s, and the dominant frequency equal to 20 Hz).

The processing report describes important aspects related to the preparation of the seismic datasets. For instance, a phase shift, an amplitude factor multiplication, and a time shift were applied to Monitor-02. Furthermore, the processing team applied a local match with a specific parameter for each azimuth sector and angle stack. The objective was to refine the repeatability (NRMS) of the data and improve the 4D responses (Barros, 2015, processing report). Damasceno (2020) also demonstrates additional improvements that can be obtained using PP and PS time-shifts. Additional methods applied in the original processing workflow of the post-stack volumes include spectral broadening that applied "effective Q" values to compensate for amplitude attenuation.

This research was based on seismic volumes, but well logs were essential to calibrate the seismic reflectors with geological surfaces (well tie). Furthermore, density and sonic logs were used to generate synthetic seismograms to better understand the post-salt reservoir's response.

Wells

Four wells were used to correlate seismic and logs during the well ties (Table 1.2). The quality control phase includes the selection of the curves, rare interpolations due to discontinuities in the measurements when merging logs from different runs. The caliper log was used to investigate outlier values, which in some cases have a relation with problematic measurements.

Table 1. 2 - Four well used to calibrate the seismic and logs.

Well	Seafloor (m)	MR (m)	Final depth (m)	Checkshot	GR	RES	DT	Density
B	-1269	19	2951	x	GRSL	RD	DT24	ZDEN
C	-1280	12	3026.5	x	GR	P40H_UNC	DTCO1	RHOZ
Q	-1280	25	3220	x	GR	RLA5	DTCO	RHOZ
R	-1246	25	3888.49		GR	HLLD	DTCO	RHOZ

Checkshots from three wells reveal a velocity variation close to the Maastrichtian reservoir. (Figure 1.12). The well tie helped to identify the major markers and the reflectors of interest, such as the top of the Cretaceous (Figure 1.13). Synthetic seismograms for different angles were used to investigate the different responses of the reservoir in two wells.

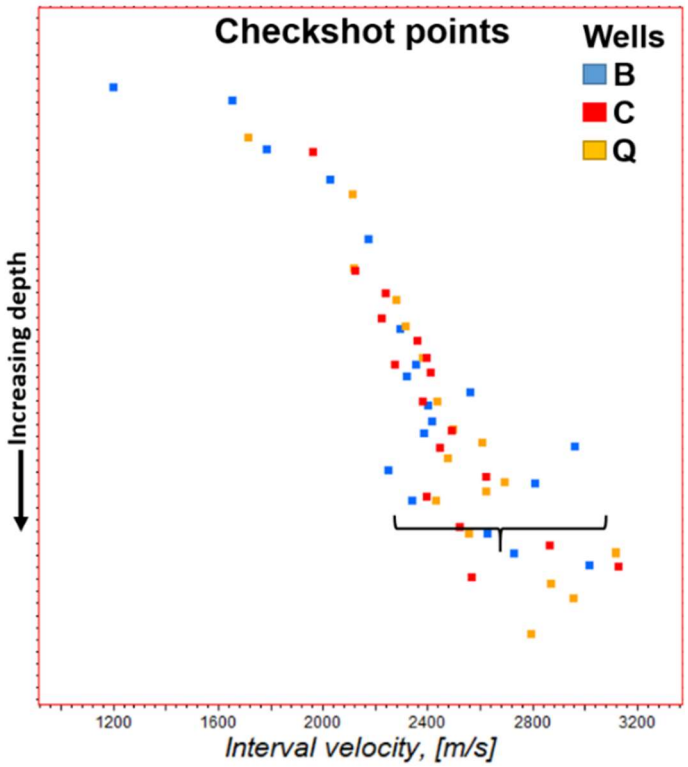


Figure 1. 12 – Checkshot points from wells B, C, and Q. Note the velocity variations close to Maastrichtian reservoirs, as indicated with the black brace.

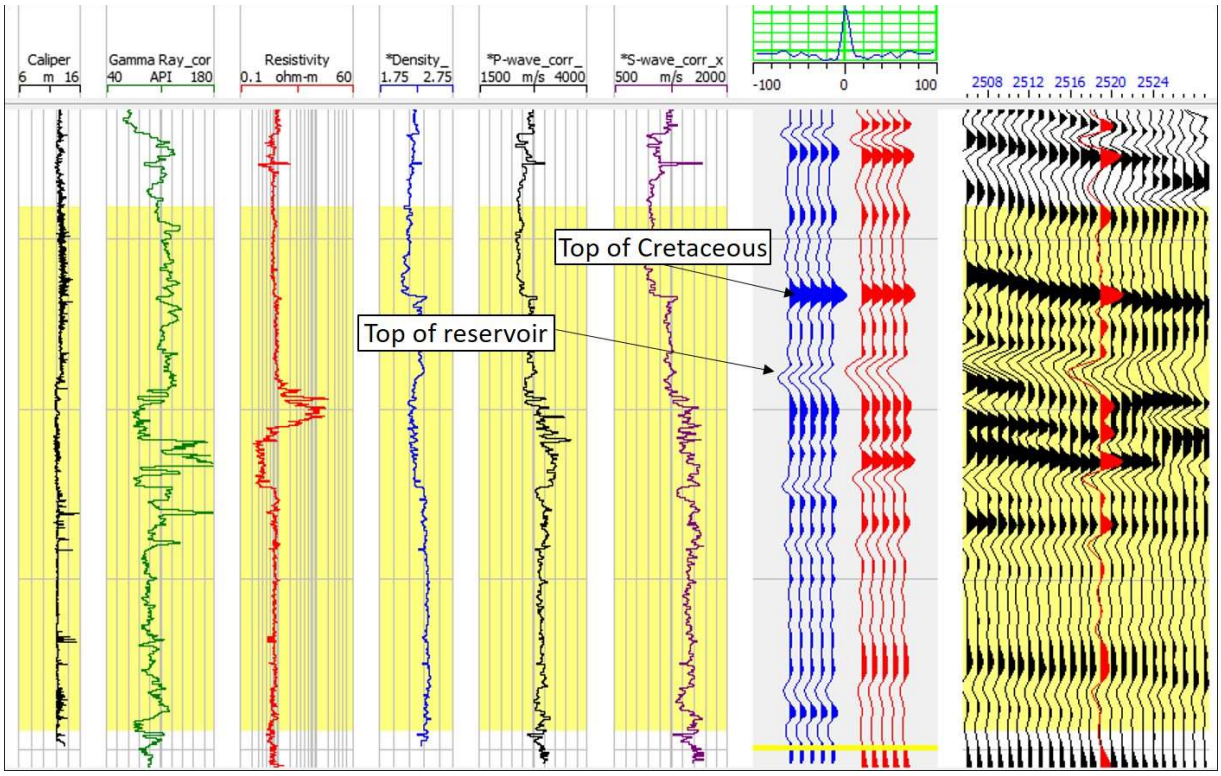


Figure 1. 13 - Example of the well tie in Well Q. Display of the log curves: caliper, gamma-ray, resistivity, density, P-wave, S-wave. The top of the Cretaceous represents a regional surface used to initiate the correlations. To generate this seismogram was initially adopted by a statistical wavelet, complemented with phase adjusted based on the logs. The vertical section is displaying 400ms of time.

The estimation of the wavelet represents a crucial phase, and the statistical wavelet was selected initially. Yi et al. (2003) compared four types of methods to estimate wavelets. To refine the wavelet estimation, I followed the hybrid method. This approach uses the amplitude spectrum of the seismic data and phase spectrum obtained from density and sonic logs to apply a phase rotation (Appendix A). Having the logs and the wavelet made it possible to generate synthetic

seismograms for different angles on incidence. Well Q has an upward thinning and shows a small gradient compared to Well B that has more abrupt changes in the properties close to the top of the reservoir (Appendix A).

Besides the well tie, the log curves were used to investigate the reservoir interval's seismic response. The wavelet effect was not considered within this exercise. Fatti et al. (1994) three-term equation was analyzed in Python to see only the impact of the changes in the logs:

$$R = \frac{1}{2}\frac{\Delta I}{I}(1 + tan^2\theta) - 4\left(\frac{W}{V}\right)^2\left(\frac{\Delta J}{J}\right)sin^2\theta - \left[\frac{1}{2}\left(\frac{\Delta\rho}{\rho}\right)tan^2\theta - 2\left(\frac{W}{J}\right)^2\left(\frac{\Delta\rho}{\rho}\right)sin^2\theta\right],$$

where P and W denote the P and S velocities, I and J represents P and S impedances, ρ means density, and θ describes the medium angle. Appendix B shows the code implemented in Python to check the amplitude variation with angle (AVA) of different parts of the reservoir. For Well R, the region with a higher gradient is located in the middle of the reservoir. This vertical variation of the reflectivity in different parts of the reservoir can indicate an improvement in the reservoir quality.

WORKFLOW

The workflow defined for this research combines different methods and techniques to enhance the identification of faults. To better understand the workflow, some items will be briefly described.

Figure 1.14 helps to understand the motivation to include a data conditioning phase. Two main discontinuities can be observed (Fault 1 and Fault 2). The left side of the figure shows abrupt changes in the amplitudes related to Fault 1. However, the recognition of the Fault 2 is not so evident, especially, when using the time slice visualization. Looking at the right panel is possible

to see a vertical section with the indication of both discontinuities. Note that it is possible to see more clearly lateral changes in the reflectors' continuity within the reservoir. However, the interval below the reservoir composed of shale has weak acoustic impedance contrasts, and the noisy components seem more visible. Close to the survey edges, dipping seismic noise features also interfere in the identification of subtle faults (Figures 1.15 and 1.16).

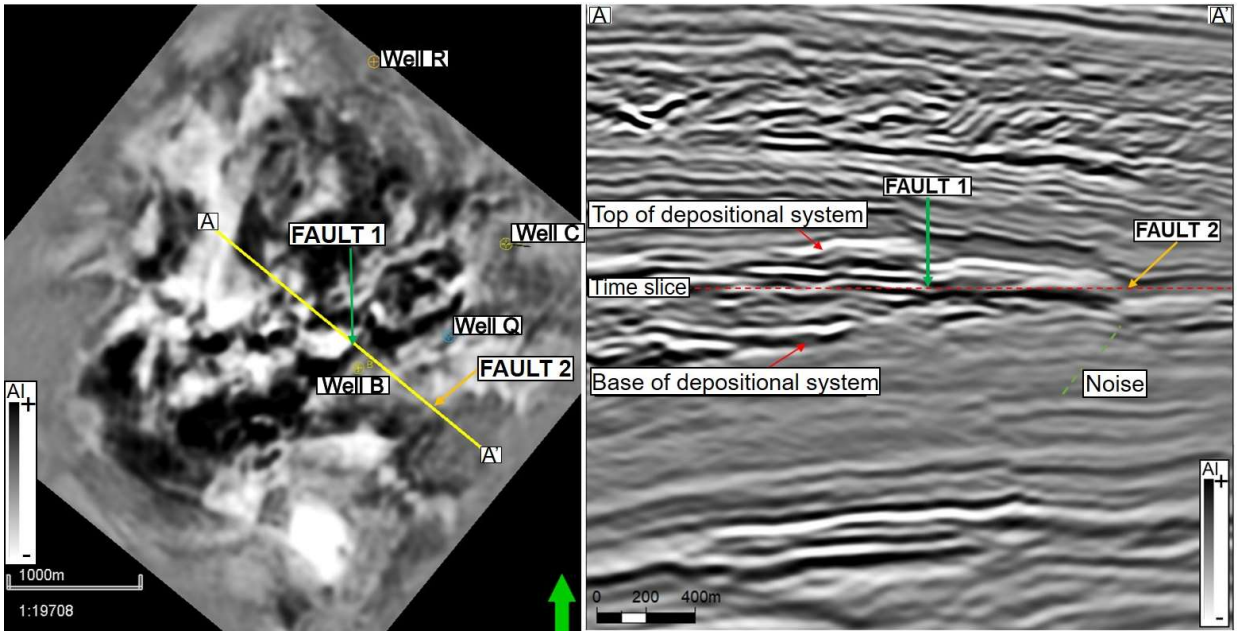


Figure 1. 14 – General aspect of the post-salt section (Monitor-01 full-stack). Left panel: time slice along the reservoir with the position of four wells used in this project. Note the abrupt limit of some amplitudes demonstrating the presence of Fault 1. In a map view, the recognition of Fault 2 is not so evident as Fault 1. Right panel: vertical section revealing the two mentioned faults, the reservoir interval, top of Cretaceous reflector, and more evident noise below the reservoir (dashed line). Vertical exaggeration: 2x.

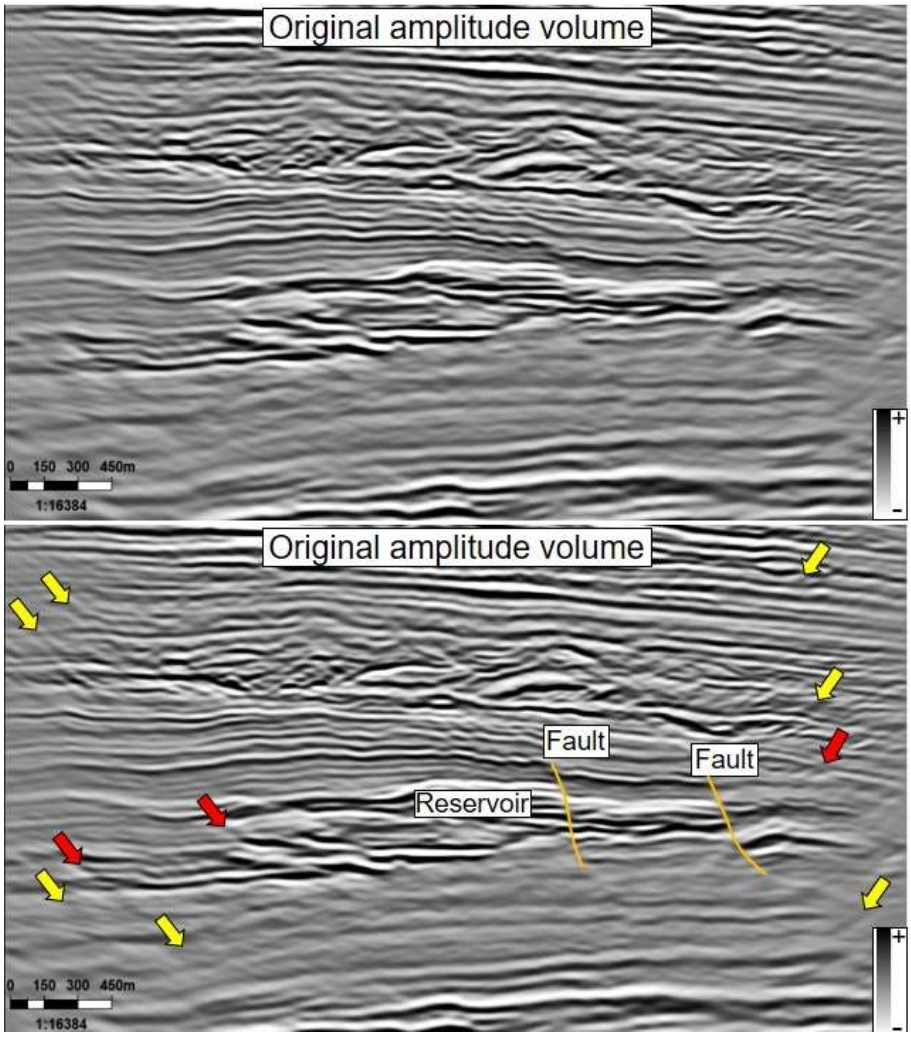


Figure 1. 15 – Original amplitude section with and without interpretation of some features of interest. Two faults can be interpreted (orange lines) based on the reflector's lateral continuity changes. Close to the edge of the survey is possible to see seismic noise (yellow arrows) that, in critical cases, can interfere in fault recognition (red arrows). Vertical exaggeration: 2x. The vertical section is displaying 1070ms of time.

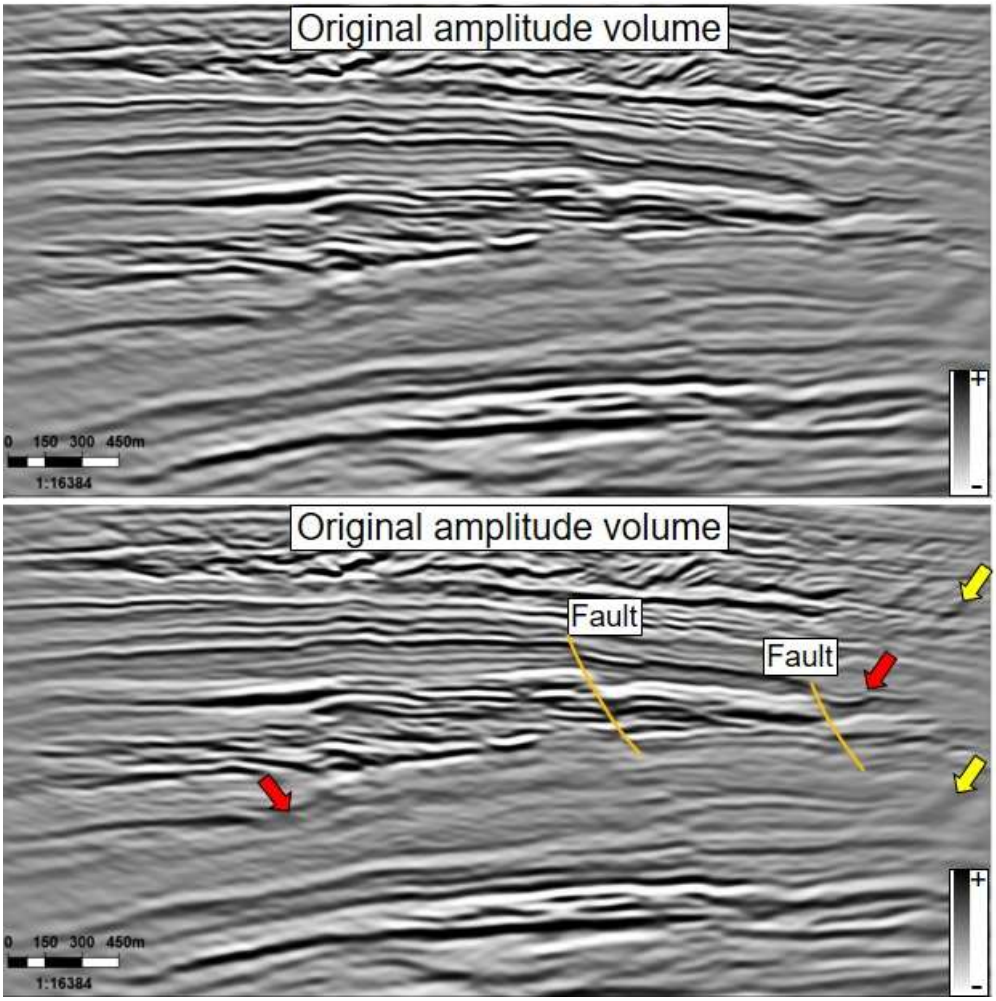


Figure 1. 16 – Original amplitude section with and without interpretation of some features of interest. It is possible to see two faults (orange lines) based on the reflector's lateral continuity changes. Close to the edge of the survey occurs dipping events (yellow arrows) that correspond to seismic noise and can affect the recognition of faults (red arrows). Vertical exaggeration: 2x. The vertical section is displaying 970ms of time.

The characterization of the main seismic features is important because it will interfere with the subsequent interpretation of seismic attribute results. Faults, fractures, stratigraphic features,

and seismic noise are examples of elements that can be enhanced (Figure 1.17). The corendered image shows the original amplitude volume (blue-white-red color bar) and the energy-ratio similarity attribute (black-and-white color bar with transparency). Green arrows indicate segments of a fault, interpreted based on the changes in the reflectors' lateral continuity. Note that chaotic sedimentary deposits (yellow box) and seismic noise (orange box) also have lower similarity values. This complexity involved in the attribute interpretation demands a consistent QC investigation to check the geological meaning of the features described.



Figure 1. 17 – Vertical section with the amplitude volume (red-white-blue color) corendered with similarity attribute. It is possible to see that low similarity values will be associated with faults (green arrows), chaotic deposits (yellows box), and seismic noise (orange box).

The interval just below the reservoir displays weak impedance contrasts compared to adjacent sections (orange box in Figure 1.18). The impact of the seismic noise is visible, and as a

consequence, difficult to the recognition of discontinuities. That tendency was observed using full-stack volumes from Monitor-01 and Monitor-02.

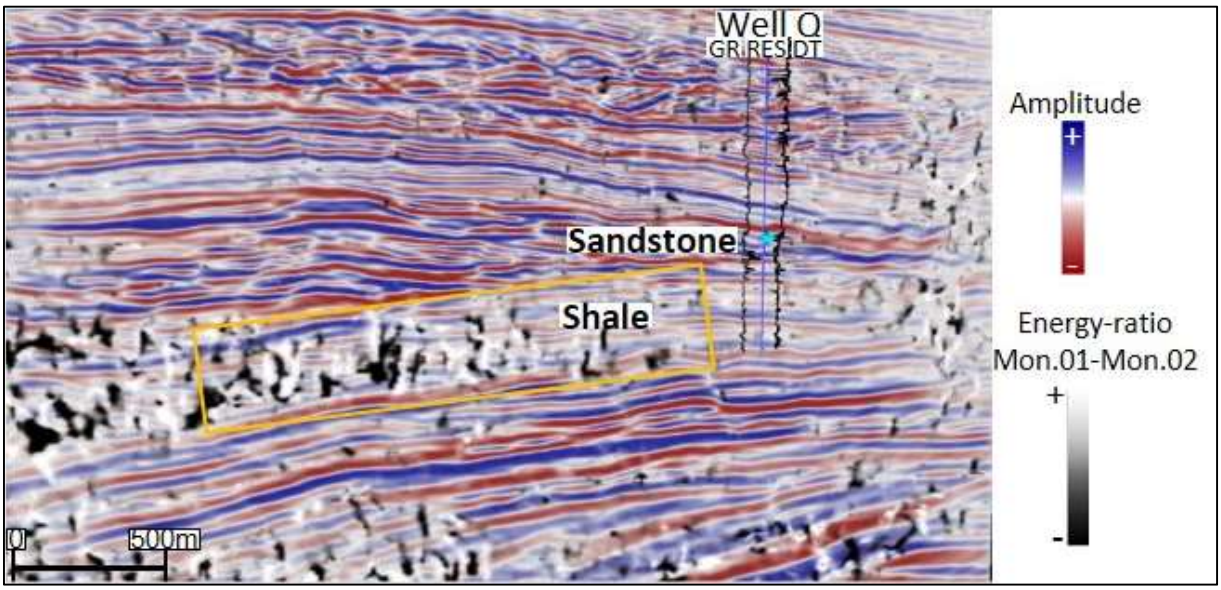


Figure 1. 18 – Vertical section comparing the original amplitude volume (red-white-blue color) and the difference between the energy-ratio attribute computed from Monitor-01 and Monitor-02. The noise below the reservoir (orange box) can be noted in both surveys and is more intense than the adjacent units.

One way to quantify the differences between the two surveys is using the NRMS error. Damasceno (2020), investigating the interval above the reservoir, demonstrates an average value of 4.5 % using the following equation:

$$NRMS = 200\ \frac{RMS(Monitor2 - Monitor1)}{RMS(Monitor2) + RMS(Monitor1)}$$

I applied the same NRMS error method to investigate the interval below the reservoir (200 ms window). The average value of 9% confirmed the higher noise content within the region of interest close to the analyzed wells (Figure 1.19).

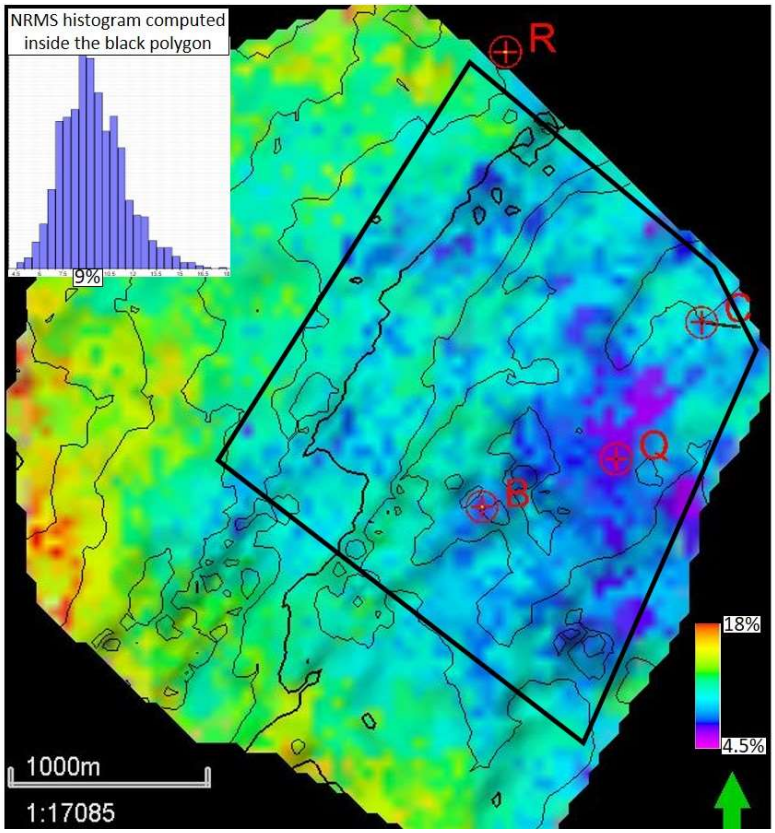


Figure 1. 19 – NRMS map between Monitor-01 and Monitor-02 PP full-stack volume, computed using a 200 ms time window below the base of the depositional system. The histogram was estimated inside the black polygon because datasets are more impacted by artifacts close to the edges of the survey,

Based on these qualitative and quantitative observations about the impact of noise, two algorithms were applied during the data conditioning phase. Different methods can be used to

prepare the seismic volumes before computing the attributes (Chopra et al., 2011). The selected methods for this research include spectral balancing and structure-oriented filtering (SOF). The application of these methods was conducted in AASPI software.

Data conditioning was defined as an initial step of the study (Figure 1.20). Then, the attributes were computed in AASPI using different techniques and parameters. PCA and SOM were used to check if additional insights can be obtained.

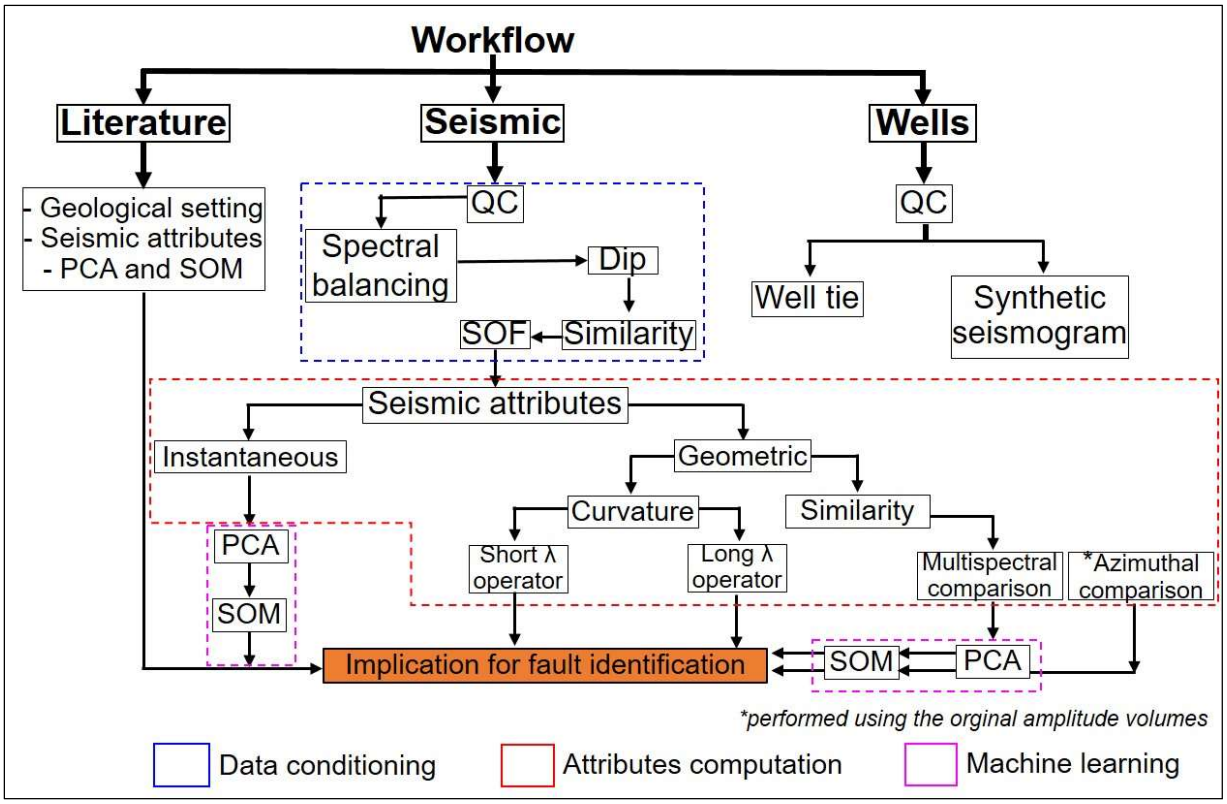


Figure 1. 20 – Workflows defined to improve the identification of faults zones in seismic. Three main phases can be recognized: data conditioning attributes computation and machine learning.

Considering the spectral balancing, different lower and higher frequency values and spectral balancing factors were tested. The selected parameters included equally spaced frequencies with the lowest and highest output frequencies of 10 and 120 Hz. The selected approach included the attenuation of lower frequencies and enhancement of higher frequencies. Also, 0.5% was considered an appropriate spectral balancing factor. This value increased the lateral extension of the reflectors, and it is less impacted by seismic noise than higher balancing factors. Appendix C contains a comparison with different spectral balancing values.

The computation of the dip attribute helped to improve the results obtained with other attributes such as coherency (Marfurt and Alvez, 2015). The gradient structure tensor method was applied in this study, which, according to Chopra and Marfurt (2007a), reveals the direction of the most significant variability based on derivatives of three axes. It considers the normal to the reflector as the first eigenvectors, as described in Marfurt and Alvez (2015). Appendix D shows the impact of some parameters, such as the lowest and highest frequency considered for the computation of the dip magnitude and dip azimuth.

An Ormsby filter (10-15-100-120 Hz) was applied in the sequence to attenuate lower frequencies associated with undulations in the seismic reflectors. The higher frequencies enhanced with spectral balancing were preserved. A comparison between the original amplitude volume and these preliminary algorithms (spectral balancing + Ormsby filter) can be found in Appendix E.

The structure-oriented filtering (SOF) was applied to attenuate random noise and emphasize the lateral continuity of the regional dip's reflectors. Chopra et al. (2011) mention the possibility of multiples implementations of SOF to achieve better results. Lyu et al. (2019) also

include SOF in a workflow to improve the recognition of faults. The selected parameters for Jubarte Field can be found in Appendix F.

This first chapter demonstrated different methods that could be applied to improve the interpretation task and faults' recognition. The objective was to emphasize that an appropriate workflow should incorporate additional techniques besides the attributes computation. The presence of seismic noise and intervals with weak acoustic impedance contrasts motivated the current investigation in the post-salt section of the Jubarte Field. Chapter 2 is presented in a manuscript format and contains the principal results and discussions of the study. Chapter 3 includes an expanded abstract that discusses how different acquisition azimuths interfere in the attribute responses. This section was submitted to the SEG 2021 Annual Meeting. Chapter 4 resumes the main conclusion for the current study and also indicates possible future analysis.

REFERENCES

Al-Dossary, S., and K. J. Marfurt, 2006, 3D volumetric multispectral estimates of reflector curvature and rotation: *Geophysics*, **71**, 5, 41-51.

ANP, 2021, Boletim mensal da produção de petróleo e gás natural. https://www.gov.br/anp/pt-br/centrais-de-conteudo/publicacoes/boletins-anp/202102boletim.pdf (in portuguese)

Balabekov, Y., M. Sebastiao, R. Couto, P. Dariva, W. Lisboa, C. Reiser, and P. Johann, 2017, Permanent Reservoir Monitoring – 4D Quantitative Interpretation: 15th International Congress of the Brazilian Geophysical Society, SBGf, Expanded Abstracts, 1-6.

Barnes, A. E., 2016, Complex seismic trace analysis, *in*: Handbook of poststack seismic attributes, SEG, 45-74.

Barros, Caio, 2015, Internal processing report – 4D/4C Jubarte PRM. Unpublished.

Batalha, M, and V. Cunha, 2018, The Big Journey of a Giant: The Campos Basin's History: Offshore Technology Conference, OTC-28781-MS, Expanded Abstracts, 1-11.

Bezerra, M. F. C., C. Pedroso Jr., A. C. C., Pinto, and C. H. L. Bruhn, 2004, The appraisal and development plan for the heavy oil Jubarte Field, Deepwater Campos Basin, Brazil: *Offshore Technology Conference,* OTC16301, 1-5.

Bhattacharya, S., and S. Verma, 2019, Application of volumetric seismic attributes for complex fault network characterization on the North Slope, Alaska: *Journal of Natural Gas Science and Engineering*, **65**, 56-67.

Bruhn, C. H. L., A. C. C., Pinto, P. R. S., Johann, C. C. M. Branco, M. C., Salomao, and E. B. Freire, 2017, Campos and Santos Basins: 40 years of reservoir characterization and management of shallow- to ultra-deep water, post- and pre-salt reservoirs – historical overview and future challenges: *Offshore Technology Conference*, OTC-28159-MS, 1-24.

Bulhões, E. M., and W. N. Amorim, 2005, Principio da SismoCamada Elementar e sua aplicacao a Tecnica Volume de Amplitudes (tecVA): 9th International Congress of the Brazilian Geophysical Society, 1-6. (in Portuguese)

Castro, R. D., J. P. Picolini, 2015, Main features of the Campos Basin Regional Geology, *in* Kowsmann, R. O., eds, Geology and Geomorphology: Elsevier, Habitats, **1**, 1-12.

Chopra, S., V. Sudhakar, G. Larsen, and H. Leong, 2000, Azimuth-based coherence for detecting faults and fractures: World Oil, 57-62.

Chopra, S., S. Misra, and K. J. Marfurt, 2011, Coherence and curvature attributes on preconditioned seismic data: *The Leading Edge*, **30**, 4, 386-393.

Chopra, S., and K. J. Marfurt, 2007a, Seismic attributes for prospect identification and reservoir characterization: SEG.

Chopra, S., and K. J. Marfurt, 2007b, Seismic curvature attributes for mapping fault/fractures, and other stratigraphic features: CSEG Recorder, 37-41.

Chopra, S., and K. J. Marfurt, 2013, Structural curvature versus amplitude curvature: The Leading Edge, **32**, 2, 178-184.

Colodette, G., C. A. G. Pereira, C. A. M. Siqueira, G. A. S. M. Ribeiro, R. Rodrigues, J. S. Matos, and M. P. Ribeiro, 2007, The new deepwater oil and gas province in Brazil: Flow assurance and artificial lift: innovations for Jubarte Heavy Oil: OTC-19083, Expanded Abstracts, 1-9.

Daher Jr. B., C. A. M. Siqueira, I. Nascimento, I. A. Pinto, J. B. Farias, R. A. B. Vieira, 2007, Jubarte Field– Development Strategy: *Offshore Techonology Conference*, OTC 19088, 1-5.

Damasceno, A., 2020, 4D quantitative interpretation of Jubarte Field (Brazil) – an integrated approach: M.S. thesis, Colorado School of Mines.

Dariva, P., W. L., Ramos Filho, C. C. Born, C. M. O. Falcone, and I. B. Zorzanelli, 2016, Monitoramento Sismico 4D no Campo de Jubarte, Bacia de Campos – Brasil: Congresso Brasileiro de Geologia.

Davison, I, 2007, Geology and tectonics of the South Atlantic Brazilian salt basins, *in* Ries, A. C., Butler, R. W. H., and Graham, R. H., eds., Deformation of the Continental Crust: The Legacy of Mike Coward: The Geological Society of London, **272**, 345-359.

Davison, I., L. Anderson, and P. Nuttall, 2012, Salt deposition, loading and gravity drainage in the Campos and Santos salt basins, *in* Alsop, G. I., Archer, S. G., Hartley, A. J., Grant, N. T., and Hodgkinson, R., eds, Salt Tectonics, Sediments and Prospectivity: The Geological Society of London, **363**, 159-173.

Del Rey, A.C., C.M.O. Falcone, J.G.R. da Silva, M.G.C. Meira, I.B. Zorzanelli, and R.A.B. Vieira, 2012, Jubarte Field 3D modeling based on the integration of outcrop analogs and elastic

seismic attributes, *in* Norman, C.R., P. Weimer, S.M.C. dos Anjos, S. Henrickson, E. Marques, M. Mayall, R. Fillon, T. D'Agostino, A. Saller, K. Campion, T. Juang, R. Sarg, and F. Schroeder, eds, New understanding of the Petroleum Systems of Continental Margins of the World: Society for Sedimentary Geology, 32, 1-17.

Delgado, L., A. Batezelli, and J. Luna, 2018, Petroleum geochemical characterization of Albian-Oligocene sequences in the Campos Basin: "Case study: Eastern Marlin oilfield, offshore, Brazil": *Journal of South American Earth Sciences*, **88**, 715-735.

Fatti, J. L., G.C. Smith, P.J. Vail, P.J. Strauss, and P.R. Levitt, 1994, Detection of gas in sandstone reservoirs using AVO analysis: a 3-D seismic case history using the Geostack technique: *Geophysics*, **59**, no.9, 1362-1376.

Fontanelli, P. De R., L. F. De Ros, and M. V. D. Remus, 2009, Provenance of deep-water reservoir sandstones from the Jubarte oil Field, Campos Basin, Eastern Brazilian Margin: *Marine and Petroleum Geology*, **26**, 1274-1298.

Gontijo, R. C., C. E. Souza Cruz, J. L. L. Caldas, L. M. Arienti, R. S. F. D'Avila, 2005, Structurally controlled sand-rich gravity deposits of the Jubarte Oil Field (Brazil deep-water sedimentation on the Southeast Brazilian Margin Project): AAPG Annual Meeting, Abstract.

Guardado, L. R., B. Wolff, and J. A. S. L. Brandao, 1997, Campos Basin, Brazil, a Model for Production Atlantic Type Basins: Offshore Technology Conference, OTC-8484, Expanded Abstracts, 457-462.

Hart, B. S., 2011, Introduction to seismic interpretation: AAPG discovery series, **v.1.1**, no. 16.

Iacopini, D., R. W. H. Butler, S. Purves, N. McArdle, and N. de Freslon, 2016, Exploring the seismic expression of fault zones in 3D seismic volumes: *Journal of Structural Geology*, **89**, 54-73.

Libak, A., B. Alaei, and A. Torabi, 2017, Fault visualization and identification in fault seismic attribute volumes: implications for fault geometric characterization: *Interpretation*, **5**, 2, B1-B16.

Liu, Z., C. Song, H. Cai, X. Yao, and G. Hu, 2017, Enhanced coherence using principal component analysis: Interpretation, 5, no.3, T351-359.

Luo, Y., S. Al-Dossary, M. Marhoon, and M. Alfaraj, 2003, Generalized Hilbert transform and its applications in geophysics: *The Leading Edge*, **22**, 3, 1-12.

Lyu, B., J. Qi, G. Machado, F. Li, and K. J. Marfurt, 2019, Seismic fault enhancement using spectral decomposition assisted attributes: 89th SEG Annual Meeting Abstract, 1938-1942.

Lyu, B., Qi, J., F. Li, Y. Hu., T. Zhao, S. Verma, and K. J. Marfurt, 2020, Multispectral coherence: Which decomposition should we use?: *Interpretation*, **8**, no. 1, T115-T129.

Marfurt, K. J., and T. M. Alves, 2015, Pitfalls and limitations in seismic attribute interpretation of tectonic features: *Interpretation*, **3**, no.1, A5-A15.

Marfurt, K. J., R. M. Scheet, J. A. Sharp, and M. G. Harper, 1998a, Suppression of the acquisition footprint for seismic sequence attribute mapping: *Geophysics,* **63**, no.3, 1024-1035.

Marfurt, K. J., R. L., Kirlin, S. L. Farmer, and M. S. Bahorich, 1998b, 3-D seismic attributes using a semblance-based coherency algorithm: *Geophysics*, **63**, 4, 1150-1165.

Mohriak, W. U., P. Szatmari, and S. Anjos, 2012, Salt: geology and tectonics of selected Brazilian basins in their global context*, in* Alsop, G. I., Archer, S. G., Hartley, A. J., Grant, N. T., and Hodgkinson, R., eds, Salt Tectonics, Sediments and Prospectivity: The Geological Society of London, **363**, 121-158.

Milani, E. J., H. D. Rangel, G. V. Bueno, J. M. Stica, W. R. Winter, J. M. Caixeta, O. C. Pessoa Neto, 2007, Bacias Sedimentares Brasileiras – Cartas estratigraficas, in: Boletim de Geosciencias da Petrobras, **15** (2), 183-205.

Rijks, E. J. H., and J. C. E. M. Jauffred, 1991, Attribute extraction: an important application in any detailed 3-D interpretation study: *The Leading Edge*, **10**, 11-19.

Roberto, M., A. B. Coutinho, and A. R. Dos Santos, 2018, Campos Basin Technologies Yard: 40 Years of Lessons Learned: Offshore Technology Conference, OTC-28716-MS, Expanded Abstracts, 1-31.

Roberts, A., 2001, Curvature attributes and their application to 3D interpreted horizons: First break, **19,** no.2, 85-100.

Roden, R., T. Smith, and D. Sacrey, 2015, Geologic pattern recognition from seismic attributes: Principal component analysis and self-organizing maps: Interpretation, **3**, no. 4, SAE59-SAE83.

Rosa, A. L. R., 2018, Analise do sinal sismico, Sociedade Brasileira de Geofisica (SBGf), 713 p. (in Portuguese)

Rosa, A. L. R., L. R. Arso, and R. Jaegher, 1985, Mapping oil-water contact with seismic data in Campos Basin, Offshore Brazil: SEG Annual Meeting, Abstract, 441-442.

Taner, M. T., F. Koehler, and R. E., Sheriff, 1979, Complex seismic trace analysis: *Geophysics*, **44**, no. 6, 1041-1063.

Tarcha, B. A., R. G. Furtado, O. C. Borges, L. Vergara, A. I. Watson, and G. T. Harris, 2016, Subsea ESP Skid Production System for Jubarte Field: Offshore Technology Conference, OTC-27138-MS, Expanded Abstracts, 1-20.

Thedy, E. A., W. L. Ramos Filho, J. R. R. da Silva, S. Seth, and S. Maas, 2011, Challenges for Jubarte Permanent Seismic System: 12th International Congress of the Brazilian Geophysical Society, SBGf, Expanded Abstracts, 1379-1382.

Thedy, E. A., P. Dariva, W. L. Ramos Filho, P. O. Maciel Jr., F. E. F. Silva, and I. B. Zorzanelli, 2015, Initial Results on Permanent Reservoir Monitoring in Jubarte, Offshore Brazil: 14th International Congress of the Brazilian Geophysical Society, SBGf, Expanded Abstracts, 838-841.

Winter, W. R., R. J. Jahnert, A. B. Franca, 2007, Bacia de Campos, in : Boletim de Geosciencias da Petrobras, **15** (2), 511-529.

Yi, B. Y., G.H. Lee, H.J. Kim, H.T. Jou, D.G. Yoo, B.J. Ryu, and K. Lee, 2013, Comparison of wavelet estimation methods: *Geosciences Journal*, **17**, no. 1, 55-63.

Zhao, T., V. Jayaram, A. Roy, and K. J. Marfurt, 2015, A comparison of classification techniques for seismic facies recognition: *Interpretation*, **3**, no. 4, SAE29-SAE58.

CHAPTER 2: SEISMIC ATTRIBUTES AND UNSUPERVISED MACHINE LEARNING TECHNIQUES APPLIED TO FAULT CHARACTERIZATION IN A POST-SALT RESERVOIR INTERVAL, JUBARTE FIELD (CAMPOS BASIN)

Edimar Perico[1,2] and Dr. Heather Bedle[2].

[1]Petroleo Brasileiro S.A. (Petrobras).

[2]The University of Oklahoma, School of Geosciences.

Keywords: data conditioning, seismic attributes, faults, interpretation, unsupervised machine learning

ABSTRACT

Seismic attributes are routinely applied for interpretation tasks. Changes in amplitude and phase components can reveal faults, and as such, provide insights into hydrocarbon reservoir management. We investigate how different seismic attributes can improve the recognition of discontinuities, including data conditioning and unsupervised machine learning methods as complementary analyses. The area covered by the 4D/4C Jubarte Permanent Reservoir Monitoring (PRM) system in the northern part of Campos Basin was used to evaluate the impact of instantaneous and geometric attributes. More detailed analyses and comparisons between different parameters were performed using geometric attributes. For instance, when evaluating the curvature attributes, structural and amplitude methods were tested with long and short wavelength operators. While changes in seismic anomalies associated with post-salt reservoirs reveal the presence of

fault zones, seismic noise and geological units with weak acoustic impedance contrasts required the application of additional methods. We applied spectral balancing and structure-oriented filtering (SOF) to increase the lateral continuity of some stratigraphic reflectors and attenuate random noise. Fault zones are more evident after the data conditioning, with higher contrasts compared to adjacent areas. Of the instantaneous attributes employed, the cosine of instantaneous phase was the most useful revealing discontinuities and was less impacted by different amplitude contrasts. Energy-ratio similarity revealed discontinuities with more precision, a positive aspect to increase the mapping accuracy. We also noticed that the fault geometry was better defined using the broadband volume compared to specific filter banks. Most-positive and most-negative principal curvature components indicated more detailed or major features, depending on the operator size. Also, these components have the advantage of indicating possible up-thrown and down-thrown sides of a deformational zone, beneficial to time or horizon slice analysis. The large number of seismic cubes and their derivative attributes motivated the use of principal component analysis (PCA) and self-organizing maps (SOM) for a multi-attribute analysis. For structural purposes, we consider these unsupervised machine learning techniques were more effective when applied using geometric attributes. The highest component independence resulting from PCA shows an agreement with qualitative observations that multi-spectral and broadband volumes are the most appropriate data for identifying faults. SOM complemented the identification of faults with clusters composed of specific neurons aligned within structural discontinuities in the reservoir interval. The improvements in fault mapping obtained demonstrated the importance of having a workflow that combines different attribute methods. For the Jubarte Field, a multi-attribute approach demonstrates advantages for delineating the lateral extension of faults and a more precise

discontinuity location. Finally, it was noted that seismic noise and stratigraphic features have a significant impact on the characterization of discontinuities associated with faults, and because of this, in-context interpretations are required to validate the methods.

INTRODUCTION

Seismic reflection studies strongly support the characterization of geological features in the subsurface. Insights into stratigraphic and structural elements can be obtained using original amplitude volumes and are commonly analyzed with vertical sections and time/horizons slices. Essential components to describe the real part of the seismic traces are the amplitude and phase (Taner et al., 1979). Lateral and vertical changes within these two components can reveal the presence of structural features. Furthermore, variations of the signal/noise ratio and the seismic reflector dip also reveal discontinuities (Marfurt et al., 1998a; Hart, 2011). There is not a simple procedure to follow in all cases, and under some circumstances, alternative and insightful interpretational images require a variety of filters and attributes (Chopra and Marfurt, 2007b).

The vast number of attributes available result from an evolution of mathematical concepts, associated with changes in the seismic acquisition styles (2D and 3D surveys) and technological innovations that improved computer performance (Roberts, 2001; Chopra and Marfurt, 2005; Zhao et al., 2015). The objective of this study is to identify the benefits of a variety of seismic attributes for fault characterization, particularly the recognition of subtle faults in intervals with high noise content or weak acoustic impedance contrasts. The results of this in-depth analysis of fault enhancement procedures in the Jubarte Field can complement structural studies in areas with similar geological settings and facilitate the identification of faults by seismic interpreters.

On a local scale, the presence of faults and fractures may guide the development of hydrocarbon fields, defining injector and producer wells' location and reducing risks (Rijks and Jauffred, 1991; Al-Dossary and Marfurt, 2006). The original amplitude seismic datasets are commonly used to calculate different groups of attributes (Roden et al., 2015; Valdez, 2019) that correspond to measurements of specific parts of the seismic trace, such as continuity, frequency, amplitude, phase, and interval velocity (Hoek et al., 2010; Luo et al., 2003; Sarhan, 2017).

Some attributes are applied with success for stratigraphic and structural studies, such as the instantaneous phase that can reveal faults and unconformities (Bahorich and Farmer, 1995; Chopra and Marfurt, 2015). Chopra and Marfurt (2007c) demonstrate that curvature indicates channel elements (axes and levees) and faults. Bulhões and Amorin (2015) show improvements to identify faults and stratigraphic features using a technique called AVT (or TecVa in Portuguese).

It is also possible to recognize that some attributes are more appropriate for specific tasks. For example, fault recognition is improved using algorithms that enhance discontinuities, revealing changes of some aspect of the seismic trace (Hart, 2011; Li and Lu, 2014; Libak et al., 2017; Phillips and Fomel, 2017; Bhattacharya and Verma, 2019; Lyu et al. 2019; Lyu et al., 2020a; Valdez, 2019). Even using the appropriate attributes, identifying smaller faults represents a difficult task because other geological elements may also be enhanced (e.g., channels flanks, onlap termination) masking the fault signal.

In addition to stratigraphic features, noise will also affect the fault mapping, especially for small-scale displacements (Libak et al., 2017). Regarding smaller faults, one parameter tested by Libak et al. (2017) is the temporal window size. It was noted that a larger analysis window might overestimate the fault height when subtle faults are analyzed. Jianguo et al. (2015) mention

difficulties involved in the identification of minor faults throw related to a strike-slip system in western China. In some cases, small discontinuities may be marked by localized amplitude variations without noticeable reflector displacements (Chopra and Marfurt, 2007c).

Acquisition footprints also affect the identification of the faults. These non-desired acquisition marks can be attenuated using specific filters, preferably using unmigrated volumes (Marfurt et al., 1998a). Fehmers and Hocker (2003) simplify the structural framework and attenuated undulating reflections by applying SOF, an edge-preserving oriented smoothing method. The application of anisotropic diffusion techniques in different steps can attenuate incoherent noise and detailed stratigraphic features, keeping the average seismic amplitude the same. Based on dip and azimuth differences of the seismic reflectors and noise components (estimated within a window), the SOF emphasizes the reflectors' lateral continuity, reducing non-geological elements (Chopra and Marfurt, 2007a). Examples of improvements described by Davogustto and Marfurt (2011), Lyu et al. (2020a), and (Qi et al., 2019) include attenuation of acquisition footprint and random noise. Lou et al. (2020) combine seismic attributes to refine seismic horizon picking and recommend applying a structure-oriented filter to attenuate noise. Two faults can be readily observed within the study area using the original amplitude volume (Figure 2.1). The recognition of some discontinuities represents a more challenging task due to seismic noise and weak amplitude contrasts. The heterogeneity in the response motived the integration of seismic attributes and data conditioning to improve faults' recognition.

Damasceno (2020), studying jointed PP and PS-inversion, investigated the NRMS error and, using the cross-equalized stacks, the mean value obtained above the post-salt reservoir was 4.5% (in accordance with the value described in the processing report). Using the original

amplitude volume and the same equation to estimate the NRMS, the value obtained for a 200 ms window below the reservoir was 9%. This value shows agreement with qualitative observations that the zone below the reservoir has higher noise elements. Because of this noise, an optimum workflow needs to include steps to mitigate seismic noise before the interpretation phase.

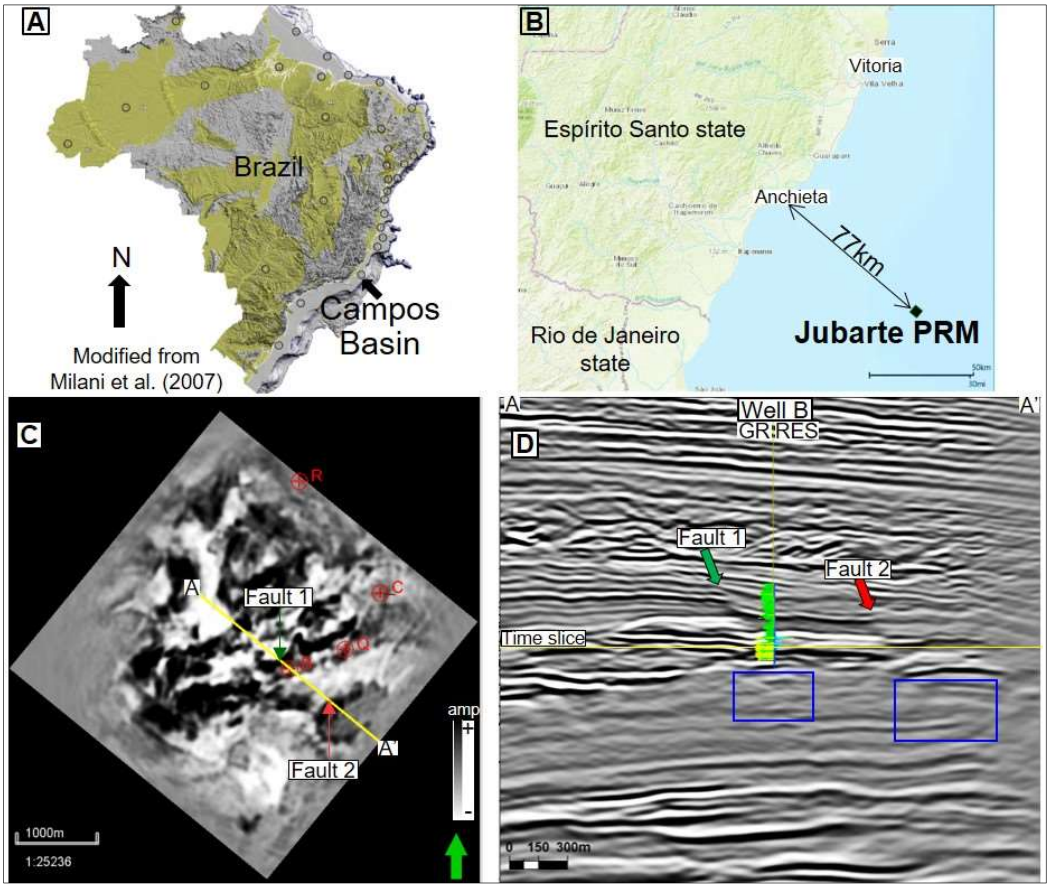


Figure 2. 1 – (A) Location of the Campos Basin in the eastern Brazilian margin and the (B) Jubarte PRM system positioned offshore of the Espírito Santo coast. (C) Time slice of the original full-stack amplitude data. Note the presence of two faults marked by changes in amplitude. (D) Vertical section close to Well B, where it is possible to see two discontinuities. Blue boxes indicate an interval below the post-salt reservoir with weak amplitude contrasts. Vertical exaggeration:2x. The vertical section is displaying 1250ms of time.

Geological setting

The evolution of the Campos Basin is related to tectono-sedimentary events that operated along the southeastern Brazilian margin during and after the Gondwana super-continent fragmentation. Extensional forces led to a break-up initiated in the south and gradually moved to the north (Mohriak et al., 2008). Winter et al. (2007) summarize the geological evolution of the basin using the three major stages, with the interval of interest located in the drift phase. Important elements to understand the regional framework are volcanic and evaporitic rocks (Ojeda, 1982; Blaich et al., 2011) that impacted the evolution of the Campos and Santos Basin (Guardado et al., 1997; Hoek et al., 2010; Delgado et al., 2018). Halokinesis was responsible for developing extensional and compressional structures such as asymmetric fold and thrust faults (Davison, 2007; Mohriak et al., 2012; Castro and Picolini, 2015). The movements of salt also contributed to fault reactivation (Davison et al., 2012). In conjunction with the thermal subsidence, halokinesis regulates the distribution and geometry of ultra-deepwater turbidites (Johann et al., 2001). Kang et al. (2018), combining seismic facies and log curves, demonstrated the presence of channel-levee complex controlled by salt movements in the Campos Basin. Besides, salt movements can form hydrocarbon traps, create migration pathways and structural traps, and impact production (Demercian et al., 1993; Coward et al., 1999; Thedy et al., 2011; Dariva et al., 2016).

Considering the region of interest, the Jubarte Field is situated in the northern part of the Campos Basin, 77 km offshore the Espírito Santo State coast, in a region with water depths between 1,200 and 1,300 m. The Maastrichtian interval includes post-salt turbidite reservoirs (Carapebus Formation) discovered in 2001 (Dariva et al., 2016; Balabekov et al., 2017), with oil production initiated in 2006 (Thedy et al., 2011). The reservoir is comprised of siliciclastic deposits, massive, immature texturally and coarse-grained, and feldspathic composition, with

moderate to poor consolidation (Balabekov et al., 2017). Porosity and permeability average values are 23-26% and 800-1,200 mD (Colodette et al., 2007; Thedy et al., 2011; Del Rey et al., 2012; Dariva et al., 2016). The hydrocarbon has a heavy oil signature with 17.19° API, a viscosity of 14 cp in reservoir conditions, and a gas-oil ratio equal to 45.97 $stdm^3/sdm^3$ (Colodette et al., 2007). These characteristics required special operations to improve production (Bezerra et al., 2004; Tarcha et al., 2016; Roberto et al., 2018). Mudstones from the Ubatuba Formation correspond to the seal. The importance of the faults in Jubarte Field has already been mentioned in some publications (Fontanelli et al., 2009; Thedy et al., 2015), particularly how faults controlled the evolution and the deposition style within the post-salt reservoir. Del Rey et al. (2012) describe the association of listric faults and salt structures and used VP/VS ratios to differentiate reservoir units (2.5-3.75) from shales (1.73-3.0).

In the Jubarte Field, Thedy et al. (2015) demonstrated how various seismic responses can be obtained over time, depending on the proximity of production and injector wells. Four primary types of amplitude responses were described to demonstrate the importance that saturation changes have on the amplitude response. In areas close to injector wells, the alteration of the pressure and water salinity conditions have a minor effect on the 4D response. Combining the seismic response with the production effects, Thedy et al. (2015) mention the benefits of better characterizing the waterfront in the southeastern part of Jubarte Field.

Data and methods

The seismic volumes used in this study were acquired by a Permanent Reservoir Monitoring (PRM) system located in the southernmost part of the Jubarte Field that covers an area

of approximately 9 km^2. It is a 4D project that uses optical fiber technology to improve the post-salt reservoirs' characterization, providing supplementary information to the geological models (Balabekov et al., 2017). Considering the acquisition parameters, the shot survey area was defined as an 11 x 11 km grid with a shooting interval of 25 meters (Barros, 2005, processing report). The acquisition included 712 receivers composed of four components (three accelerometers and one hydrophone) positioned on the ocean floor. The datasets correspond to two active acquisitions (Monitor-01 and Monitor-02), obtained with twelve months' interval, processed with a 3D pre-stack VIT Kirchhoff Depth Migration (Barros, 2005, processing report). The datasets include PP-wave reflection data, with four azimuthal sectors with five degrees of overlap.

Four wells were used to correlate the seismic volumes and log curves. The attributes were generated using AASPI software, HampsonRussel Geoview was used for well tie, Petrel was used to integrate all the sources of information, and Paradise was used to perform PCA and SOM studies. The PCA and SOM analysis were based in a more restrictive area, focused on the interval of interest with a limited time (3.1-3.5 s) and area (inline and crosslines 2350-2530). Self-organizing maps were generated using 100 epochs, using comparisons between 8x8, 10x10, and 16x16 neuron topology.

The adopted workflow included the data preparation performed before the attributes computation. Data conditioning included spectral balancing, Ormsby filter, and structure-oriented filtering. The combination of SOF and curvature attributes improve the characterization of faults, as demonstrated with a seismic data from Alberta (Chopra and Marfurt, 2007a). Chopra and Marfurt (2017) proposed a workflow to improve fault identification that combines data conditioning (two-pass structure-oriented filtering), most-positive and most-negative curvature

elements (using short and long wavelength), and fault probability volumes. Regarding the workflow for my study area, I adopted the order for the data preparation described by Ha et al. (2019), which includes the spectral balancing before the structural-oriented filtering.

SEISMIC ATTRIBUTES AND STRUCTURAL INVESTIGATIONS

Instantaneous Attributes

Seismic attributes represent measurements of different aspects of the seismic data, applied to enhance the identification of the features of interest. A starting point to demonstrate the relation between attributes and different seismic components are the instantaneous attributes. Taner et al. (1979) describe equations and concepts involved in the computation of amplitude and phase attributes. Barnes (2016) mentions the versatility of this group of attributes that can indicate bright spots, dim spots (amplitude components), and stratigraphic features (bandwidth measures).

The instantaneous phase can help structural investigations because it highlights changes in the reflector continuity (Chopra and Marfurt, 2005). Another example of attributes includes the Hilbert transform, which is applied to estimate the imaginary part of the signal (Chopra and Marfurt, 2005) and results in a phase shift of 90º (White, 1991; Barnes, 2016; Rosa, 2018). Other examples are the dominant frequency (Sarhan, 2017), amplitude volume transform AVT (Bulhões and Amorin, 2005), and instantaneous frequency, which helps to characterize low-frequency interval (zones of abnormal attenuation), as may occur above hydrocarbon reservoirs and close to fracture zones (Taner et al., 1979; Chopra and Marfurt, 2007c). The sweetness attribute corresponds to a relation between envelope and instantaneous frequency (Marfurt, 2014), and it is a good measurement to differentiate shale and sand units (Chopra and Marfurt, 2014). According

to Taner et al. (1979), the weighted average frequency improves reflectors' lateral continuity in noise areas. Barnes (2016) mentions two interesting aspects of the cosine of phase attribute: it has no discontinuities and no amplitudes changes that may interfere in the identification of the feature of interest. These attributes can be applied for different purposes, such as identifying geological features within a gas field (Radovich and Oliveros, 1998). The instantaneous attributes have a wide range of applications, but also some limitations, such as the interference of nearby reflectors that can affect the results of the instantaneous frequency attribute (Chopra and Marfurt, 2005).

Geometric Attributes

Geometric attributes represent a category of attributes commonly applied for structural investigations (Mai et al., 2009; Chopra and Marfurt, 2017). Curvature represents a second-order derivative of the reflector that reveals changes in a surface shape (Chopra and Marfurt, 2007b; Chopra and Marfurt, 2013). Two methods can be applied for the identification of fracture systems: structural vs. amplitude. Chopra and Marfurt (2011a) noted improvements for fault delineation using the amplitude curvature and more detailed features can be observed using short-wavelengths. Roberts (2001) describes the equations related to different components of a gridded surface like mean curvature, Gaussian curvature, maximum and minimum curvatures, most positive and negative curvatures. Al-Dossary and Marfurt (2006) demonstrated how curvature attributes can be estimated for the entire seismic, eliminating the need to interpret horizons to perform the analysis. Important parameters to be considered are the wavelength operator's size (short or long), the scale of observation, and the impact of noise (Roberts, 2001; Chopra and Marfurt, 2013; Bhattacharya and Verma, 2019).

Most-positive and most-negative curvatures enhanced the visualization of smaller fault segments (Roberts, 2001). Bhattacharya and Verma (2019) applied the most-positive, and most-negative curvature attributes to characterize faults in the North Slope (Alaska). Mai et al. (2009) combined curvature and coherence attributes to improve the identification of fault and folds. Aboaba and Liner (2020) used different attributes (including most-positive and most negative curvatures) to enhance the identification of paleokarst features and faults in the Arkoma Basin.

The term coherence includes different methods applied to evaluate waveform changes (Al-Dossary and Marfurt, 2006; Li and Lu, 2014; Liu et al., 2017; Chopra and Marfurt, 2018). Crosscorrelation is one example of an operation that highlights the lateral continuity of a seismic reflector because it compares two adjacent traces (Hill et al., 2006). Bahorich and Farmer (1995) use crosscorrelation and demonstrate faults as having low similarities values. An example of improvement includes the identification of discontinuities oriented parallel to the regional strike.

Another method comprises the semblance-based coherence. The windows used to compute the similarity of the seismic traces can be elliptical or rectangular. In some cases, larger vertical windows result in more evident discontinuities due to increased signal/noise ratio (Marfurt et al. 1998b). Semblance represents another method that indicates similarity between adjacent seismic traces. Instead of multiplying adjacent traces (like performed in the cross-correlation), it sums corresponding samples from both traces, and the result is squared before the final summation (Hill et al., 2006). Another difference from the cross-correlation includes the normalization processes that take into consideration the square of the individual traces.

Sobel filter is one similarity attribute applied for structural purposes having more than one implementation (e.g., Phillips and Fomel, 2017) and is sensitive to lateral changes in amplitude

(Chopra and Marfurt, 2007a; Marfurt and Alvez, 2015). Its estimation is similar to the semblance approach, but instead of summing adjacent traces, the Sobel filter attribute subtracted both traces at the beginning of the process (Hill et al., 2006). The wide range of application of coherence attributes also includes the use of individual voice components that can improve the delineation of faults (Chopra and Marfurt, 2018).

MACHINE LEARNING IN GEOPHYSICAL STUDIES

Many publications discuss the use of machine learning and seismic attributes in geosciences (Zhao et al., 2015, Kim et al., 2019; Marfurt, 2014; Ha et al., 2019; Chenin and Bedle, 2020; La Marca, 2020), some of them focused on structural features (Tingdahl and Hemstra, 2013; Liu et al., 2017; Mora et al., 2020; Hussein et al., 2020, 2021). Johann et al. (2001) analyzed seismic attributes using unsupervised and supervised techniques with applications in the Campos Basin. The pattern recognition was applied for seismic facies analysis and helped to define distinct geological units (e.g., amalgamated lobs, distal lobes, thin lobes).

Principle component analysis (PCA) is commonly applied in geosciences to indicate volumes (in our cases, seismic attributes) with higher variability, attempting to reduce redundancy within the chosen attributes so that a smaller selection of attributes may be selected for computational efficiency. The covariance matrix plays an essential role in measuring redundancy in the PCA method (Chopra and Marfurt, 2014). PCA highlights the seismic inputs with the most significant variability (Roden et al., 2015), and it is helpful for data reduction (Coléou et al., 2003; Zhao et al., 2015; Liu et al., 2017). Chopra and Marfurt (2015) applied principal component analysis to investigate spectral decomposition volumes and complement complex trace attributes

analysis. Liu et al. (2017) mention the impact of the windows of investigation and propose a three-step workflow to improve the identification of subtle features using PCA and coherence. Using a case study from Sichuan Basin, they demonstrated how different principal components can reveal geology.

Self-organizing maps (SOM) is a technique commonly applied after PCA (Chopra and Marfurt, 2014; Laudon et al., 2019), using the most appropriate attributes defined as a result of PCA. SOM is an unsupervised clustering method that defines groups that can help to delineate geological features of interest, not easily observed with other standard attribute methods. The inputs correspond to various seismic attributes that can be considered vectors in the space (Matos et al., 2009). After the first phase of training, where the prototype vectors were defined, they are compared to a new data set to map the n-dimensional space inputs into a two-dimensional grid still reflecting geological features. Matos et al. (2009) mention different methods that represent vectors, such as 1D or 2D color maps. Johann et al. (2001) mention that unsupervised techniques as an appropriate tool for exploratory investigations because in those situations, interpreters commonly have less reliable information compared to other areas (e.g., hydrocarbons fields already in production).

In terms of application of SOM, Roden et al. (2015) used SOM to characterize better stratigraphic elements, seismic facies, and features associated with hydrocarbon occurrence. Hussein et al. (2020) used a workflow to improve the identification of minor faults, using a structure-oriented filter, seismic attributes, PCA, and SOM in the offshore Taranaki Basin. Better results were obtained using multiple attributes (e.g., dip magnitude, energy-ratio similarity, most-positive, and most-negative curvature) than individual attributes could achieve on their own. In

Campos Basin, one example of an application of the SOM algorithm was to define the base of a turbidite reservoir (Matos et al., 2009).

With all of the recent, aforementioned studies into advancing and applying new interpretation techniques, it is observable that integrating data conditioning methods, different seismic attributes, and machine learning analysis will help achieve better results. Thus, we use this prior learning to design a workflow that consists of three main parts: data conditioning, attributes computation, and unsupervised clustering analysis.

RESULTS

Data conditioning

The interval of interest has discontinuities associated with faults, fracture zones, stratigraphic features, and seismic noise. The spectral balancing was applied to improve the recognition of geological features such as faults and fracture zones, as described by Chopra and Marfurt (2018). In particular, it better defines reflections in the interval with weak acoustic impedance contrasts. One of the most critical parameters tested was the spectral factor, for which 0.5% was the value that resulted in reflectors with higher lateral continuity. Besides, the Ormsby filter (10-15-100-120 Hz) attenuated seismic noise associated with non-geological undulations in the seismic data set.

The structure-oriented filtering was the second algorithm applied in the data conditioning phase. It included three inputs: post-spectral balancing volume, the dip data (computed using the gradient structure tensor), and a similarity attribute. Lower (0.3) and higher (0.4) similarity values act as a reference for preserving or filtering the input volume. Small inline and crossline windows

(12.5 x 12.5 m) helped to enhance small features making subtle variations of amplitude and phase more evident as indicated with the orange arrow in Figure 2.2.

The results of both processes, spectral balancing, and structure-oriented filtering, reveal more visible reflectors with higher lateral continuity (blue box in Figure 2.2). These modifications are important to highlight geologic features below the reservoir. This workflow attenuated undulating noise (red boxes) that interfere with fault recognition. Furthermore, faults and fractures are better delineated (yellow arrows) because the interruptions along the reflectors' lateral continuity are less affected by random noise. This initial data preparation phase does not remove all the seismic noise content but certainly helped to attenuate non-geological elements.

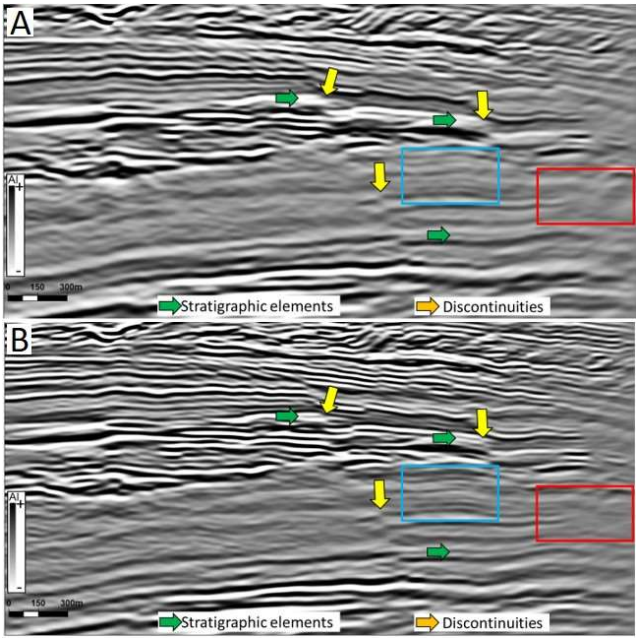


Figure 2. 2 – Comparison between the original amplitude volume (A) and the same vertical section after the application of spectral balancing, Ormsby filter, and structure-oriented filtering (B). Yellows arrows indicate discontinuities more clearly observed after the data conditioning. Red boxes indicate regions where seismic noise elements (undulating features) were attenuated. The blue box and the green arrows show improvements in the lateral continuity of reflectors.

Instantaneous attributes

Instantaneous attributes were the first group investigated to enhance fault detection. Twelve attributes were generated: Hilbert transform, envelope, instantaneous frequency, cosine of instantaneous phase, wavelet frequency, average frequency, average Bandwidth, wavelet phase, sweetness, amplitude volume transform (AVT), and RMS amplitude. Even though the calculation of some attributes was similar, all of them were evaluated. A visual inspection of the most relevant attributes (Figure 2.3) reveals strong contrasts associated with stratigraphic aspects (*e.g.,* reservoirs vs. non-reservoir). In some cases, the envelope shows discontinuities in areas with high amplitude contrasts (yellow arrow). However, it did not enhance the visualization of the fault indicated with the green arrow. In addition, the envelope attribute shows limitations in identifying discontinuities in areas with smaller amplitude contrasts, particularly below the reservoir.

The RMS amplitude attribute also demonstrates limitation in regions with weak contrast of impedance. Another disadvantage of the RMS amplitude for structural purposes is the "blurred" aspect of the discontinuities. Instantaneous frequency contains spikes that can represent reflection interference, a process described in Barnes (2016). Using the Jubarte datasets, these anomalous instantaneous frequency values were observed in regions with strong signal and low noise (such as the reservoir interval). Another disadvantage of instantaneous frequency for fault identification is its vertical computation, instead of a horizontal estimation that highlights better the structural discontinuities. Appendix G contains additional comparison figures, including all of the instantaneous attributes calculated.

Faults and fractures were better observed with other instantaneous attributes. The AVT displays the discontinuities with a relief display but contains vertical noise in some of the regions.

Cosine of instantaneous phase defines sharp terminations for faults, an essential visualization to increase interpreter accuracy. It helped define discontinuities with more linear and uniform features and is less affected by the different degrees of amplitude contrasts.

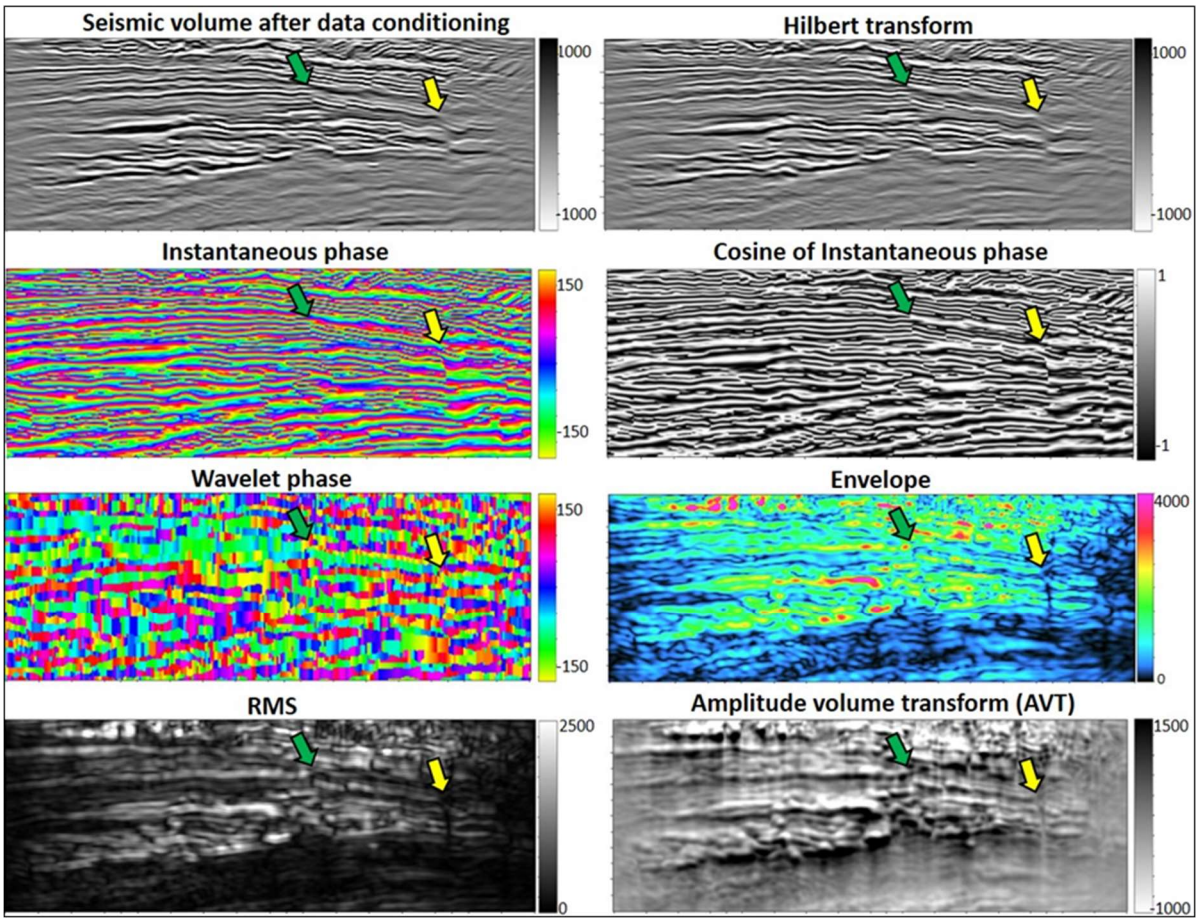


Figure 2. 3 – Comparison between the amplitude volume after the data conditioning (upper left figure) with different instantaneous attributes. Two faults are indicated with the green and yellow arrows. Better results for fault recognition are observed with the cosine of instantaneous phase attribute. A description of different aspects of these attributes is in the text. The vertical section is displaying 600ms of time.

PCA was applied to identify the attributes with the higher variability and independence from one another, thereby reducing the number of instantaneous attributes included for SOM analysis. For eigenvector one (PC1), the volumes with higher variability are RMS amplitude (35.56 %) and envelope (35.31 %). Evaluations of the attributes indicate that PCA's variability was not necessarily associated with structural elements. RMS amplitude and the envelope anomalies reflect more clearly changes in stratigraphic units. Appendix H shows the PCA results.

To generate the SOM, the RMS amplitude and envelope were combined with other attributes as guided by the PCA analysis. The highest contributions for the second principal component were defined by the Hilbert transform (46.89 %) and instantaneous phase (46.40 %) attributes. The third principal component's highest variability was controlled by the average frequency and instantaneous frequency (also considered for SOM). Although this group of attributes provided a representative visualization of the main geological units, it didn't highlight specific neurons associated with fault surfaces in the SOM. Based on this result, the application of unsupervised clustering techniques using only instantaneous attributes was noted to be limited potential. Appendix I shows figures with SOM results.

Curvature attributes

A first comparison between the structural curvature algorithm and the amplitude curvature demonstrates that the first method resulted in more uniform anomalies (Appendix J). The amplitude algorithm highlights discontinuities, especially in areas with large amplitude changes. The dip component represents a crucial volume because it helps to attenuate the effect of the regional dip of the reflectors.

A comparison with the original seismic data reveals that most-positive (k1) and most-negative (k2) principal curvature components delineate subtle changes in reflectors that are not easily observed due to weak impedance contrasts. Long and short-wavelength (λ) operators were compared during the curvature attribute evaluation (Appendix K).

The most-positive and most-negative components highlighted some features of interest, having the short-wavelength a better representation of small changes in curvature, like subtle faults or small reflector flexures (Figure 2.4). The most-positive and most-negative components also enhance stratigraphic features and seismic noise, especially when short-wavelength was applied (orange box). Vertical fault segments are highlighted with curvature (yellow arrows). Discontinuities with dip angles about 70-75º (green arrows) show stair-step features that compromise the fault geometry's recognition.

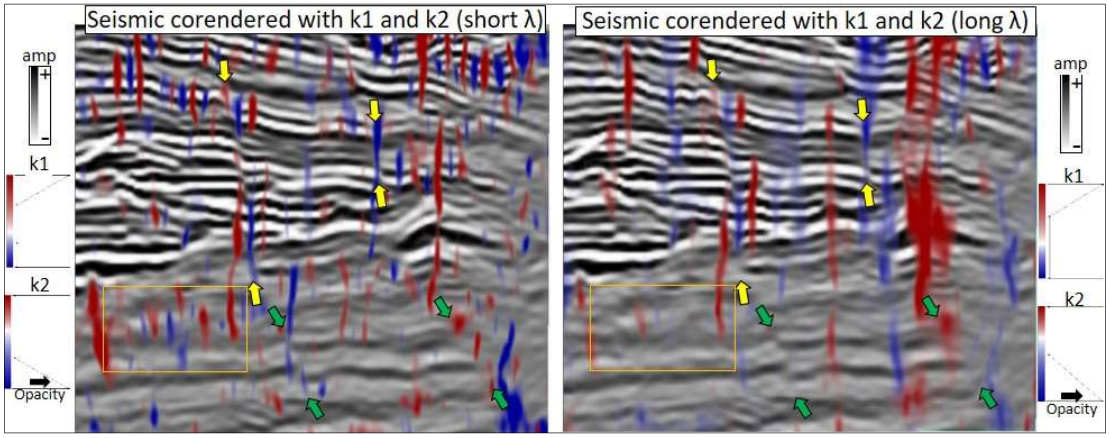


Figure 2. 4 - Comparison between the amplitude volume (post data conditioning) and the most-positive (k1) and most negative curvature (k2), obtained with short (left) and long-wavelength operators (right). Yellow arrows indicate more vertical faults observed close to the top of the reservoir. The green arrows show areas where the discontinuities have a lower dip angle, and the curvature attribute couldn't delineate the fault geometry completely (stair-step features). The orange box demonstrates the interval with weak impedance contrast, where seismic noise was enhanced with short wavelengths. The vertical section is displaying 350ms of time.

Figure 2.5 demonstrates the importance of checking the results. Using a time slice with short and long wavelength is possible to see that curvature components delineate faults (yellow and green arrows). Short-wavelength also enhances the visualization of stratigraphic features (orange arrow).

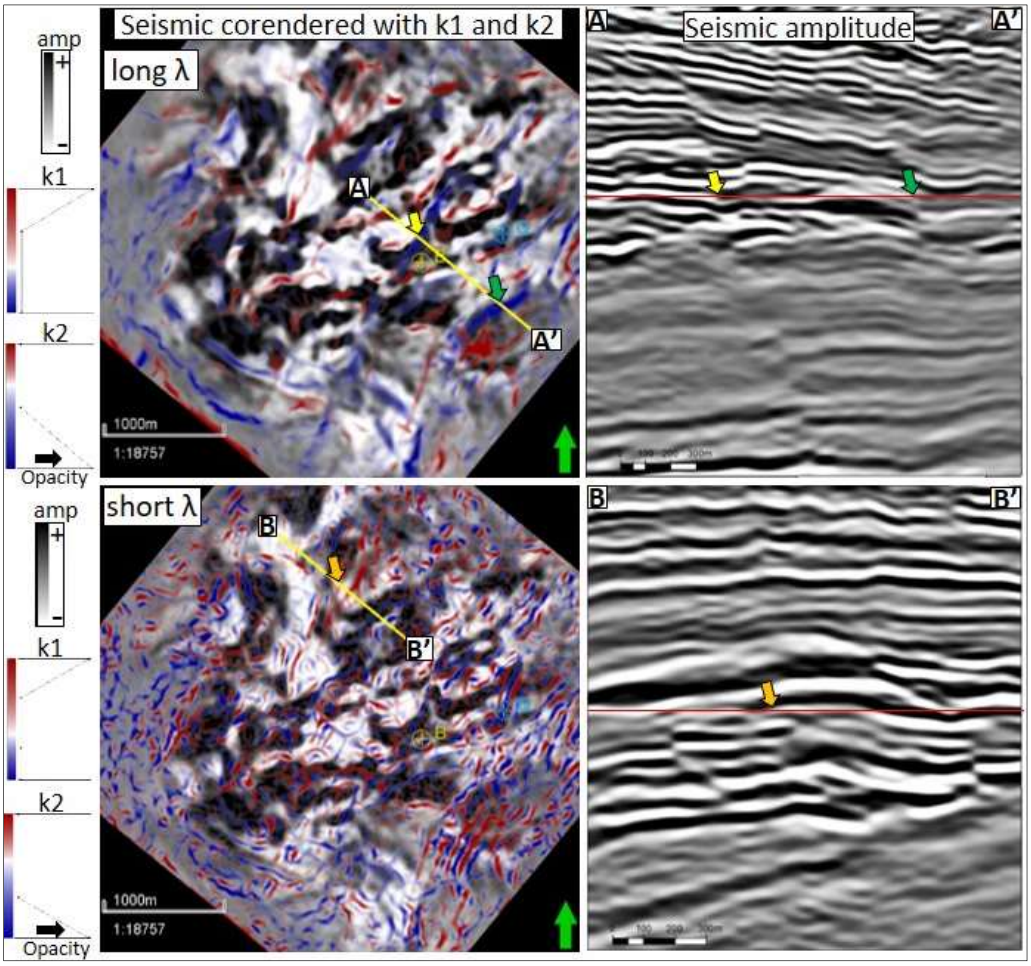


Figure 2. 5 – Comparison between short and long-wavelengths (λ) used to compute curvature most -positive (k1) and most-negative (k2) components. Upper part: time slice with long-wavelength demonstrating two faults, also visible in the vertical section (yellow and green arrows). Short-wavelength reveals localized features such as noise and stratigraphic terminations (orange arrow).

Similarity attributes

The similarity attributes computed were energy-ratio, Sobel filter, and outer product. It is possible to see that all attributes facilitate the identification of the discontinuities, optimizing the recognition of some faults. The energy-ratio attribute shows great results because the discontinuities have a sharp termination (Figure 2.6). As with the other types of attributes, it is essential to evaluate the results because seismic noise will also be enhanced (red arrow) and some stratigraphic features.

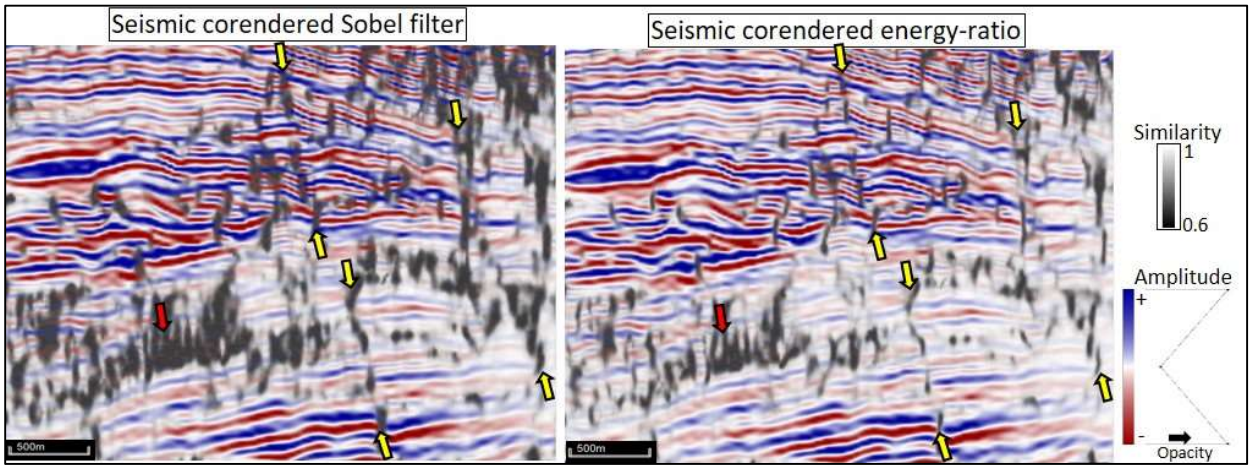


Figure 2. 6 – Comparison between the seismic dataset (after data conditioning) with Sobel filter and energy ratio similarity attributes. Note the sharp termination of features with low similarity in energy ratio (right figure).

The sharp anomalies generated with energy-ratio similarity can also be observed in time slices (green arrows Figure 2.7). Locally, some discontinuities (structural and stratigraphic) are

better observed with the Sobel filter (orange arrows). The outer-product results are similar to the ones obtained with the energy-ratio attribute.

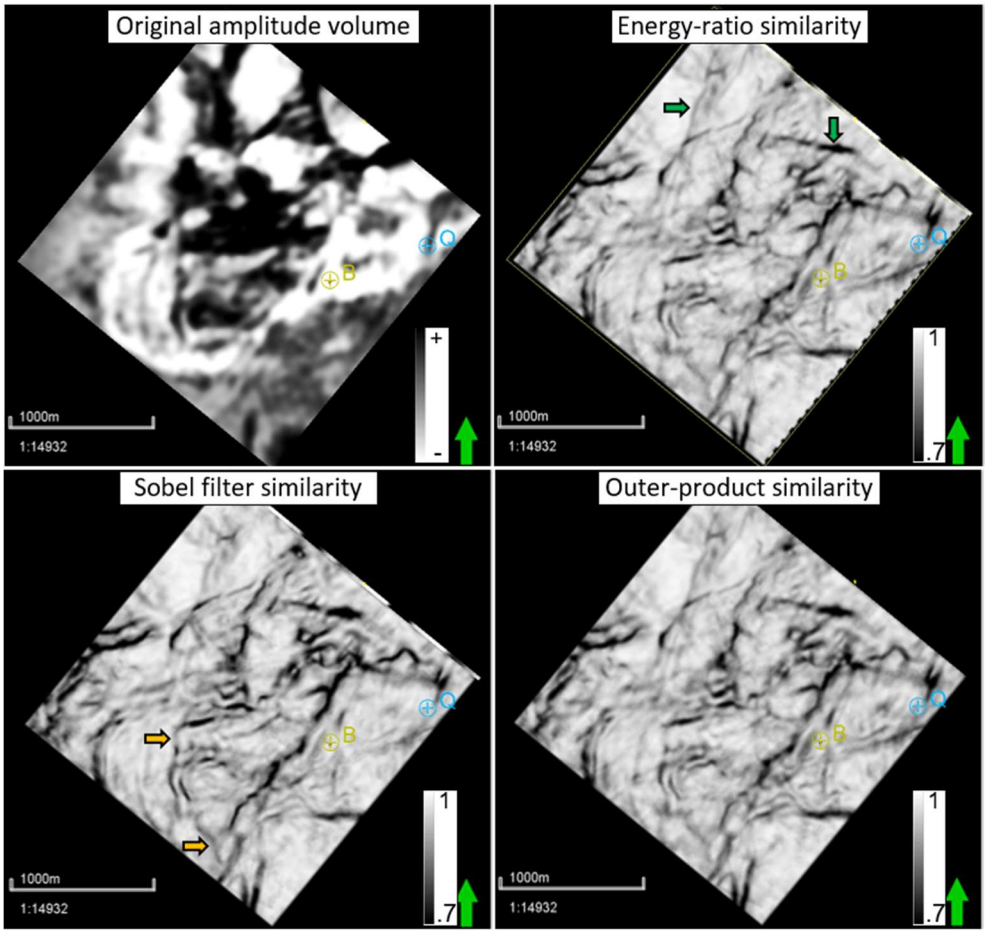


Figure 2. 7 – Comparison between the original amplitude volume (full-stack, Monitor-01) and the Sobel filter, outer-product, and energy-ratio attributes. The attributes were computed using the filtered volume after the application of the SOF algorithm. The energy-ratio attribute resulted in more sharp discontinuities compared to Sobel filter results, as indicated with the green arrows. On the other hand, the Sobel filter attribute helped reveal local features, such as the ones indicated with the orange arrows.

Frequency-based analysis

Energy-ratio similarity, Sobel filter, and outer-product attributes were used to compare the results of different frequency intervals. In some cases, specific frequencies can highlight discontinuities because some parts of the amplitude spectrum may have less noise than others. For instance, Qi et al. (2019) mention that 10 Hz volume helped define larger discontinuities better than higher frequencies spectral voices.

For each attribute (energy-ratio similarity, Sobel filter, and outer-product), one broadband volume, one multi-spectral volume, and ten frequency cubes were calculated using the linear construction. In total, thirty-six volumes were generated. The lower and higher frequencies were 5 and 85 Hz, based on the amplitude spectrum of the full stack cube, Monitor-01. The taper value of 30% was adopted. This parameter defines the Ormsby filter shape (higher values result in closer frequencies 2 and 3 components).

Figure 2.8 demonstrates that the fault geometry is uniformly delineated with the broadband volume (yellow arrows). When analyzed individually, lower frequencies (9-15-29-35 Hz) show too segmented anomalies, and the higher frequencies (49-55-59-65 Hz and 69-75-79-85 Hz) are strongly affected by noise. The qualitative investigation shows that the broadband data set provides a good visualization of the entire fault surface and is less affected by noise.

Next, all the 36 volumes generated with different frequencies were compared using PCA. The multi-spectral and broadband volumes contributed more to the variability of the first principal component (Figure 2.9). The second principal component has the contribution of lower and higher frequencies.

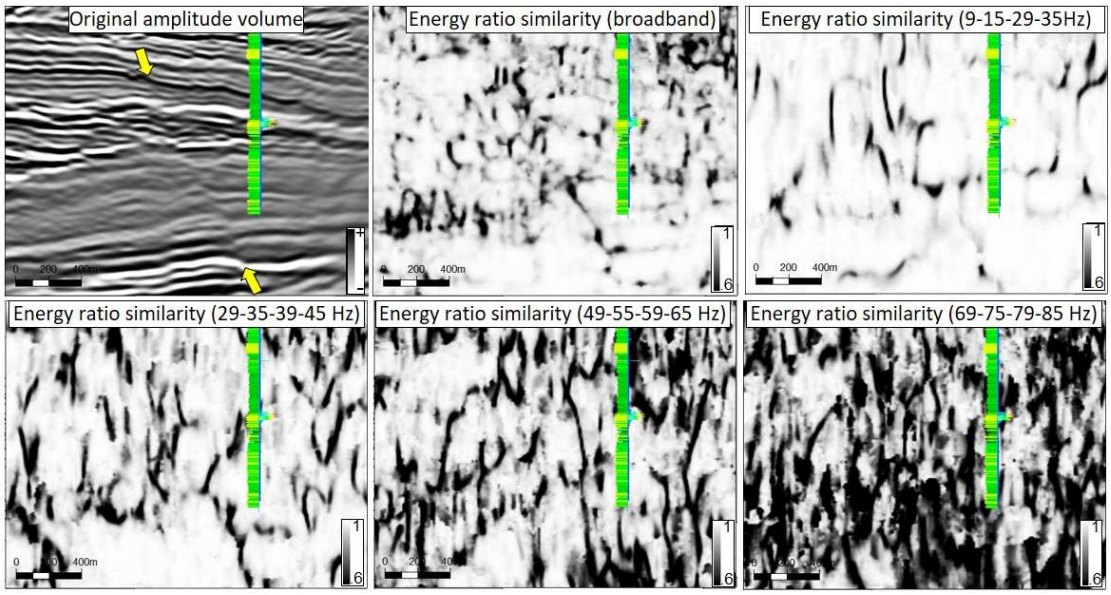


Figure 2. 8 – Vertical section comparing the original amplitude volume (full-stack, Monitor-01) with the energy-ratio similarity attribute with different frequency volumes. The broadband cube reveals better the fault geometry compared. Well is projected about 115 m from its position.

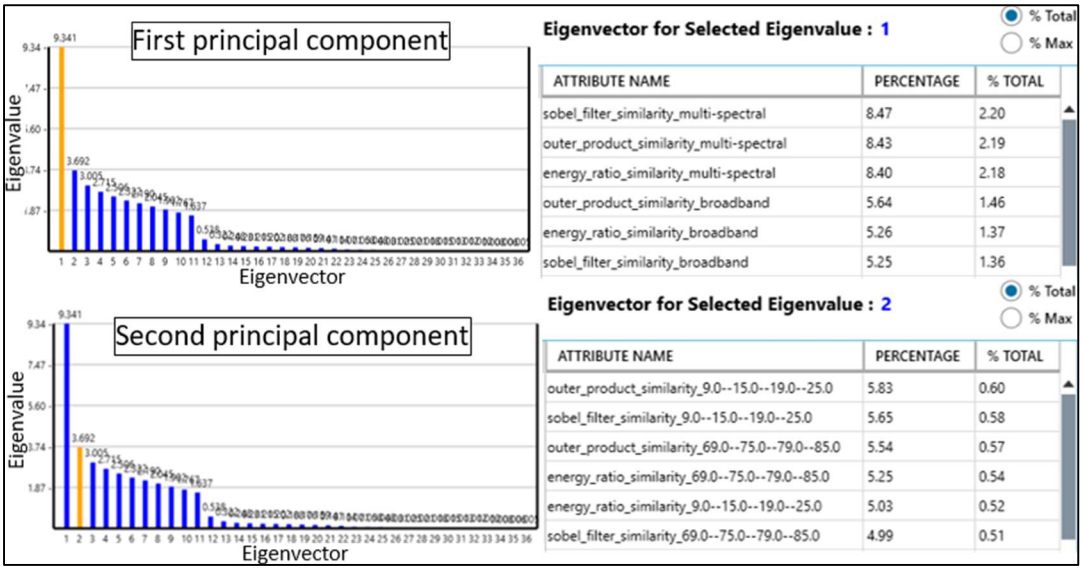


Figure 2. 9 – PCA results for similarity attributes, including multi-spectral, broadband volumes, and ten frequency cubes for each similarity attributes (energy-ratio, Sobel filter, and Outer product). Input includes 36 volumes. The volumes with higher variability include multi-spectral and broadband volumes.

Based on the agreement between qualitative investigation and PCA results for multispectral and broadband volumes, they were used as input for the unsupervised clustering investigation. SOM enhanced the visualization of some discontinuities (Figure 2.10). SOM shows fault segments defined by a specific group of neurons as indicated with the green and red arrows. The selected clusters indicated with the orange color define interruptions related to faults within the reservoir. However, as observed below the reservoir, the same cluster indicates some noise components.

Another example of improvement includes the identification of possible small fault segments (Figure 2.11). The map view with the original amplitude volume reveals an amplitude decrease (white color) in the region indicated with the composite line location. The SOM provides more contrasts (red neuron). The vertical seismic section on the right displays the changes reflector continuity that can be associated with a minor fault (green arrow). More examples of the meaning of different clusters obtained with SOM can be seen in Appendix L.

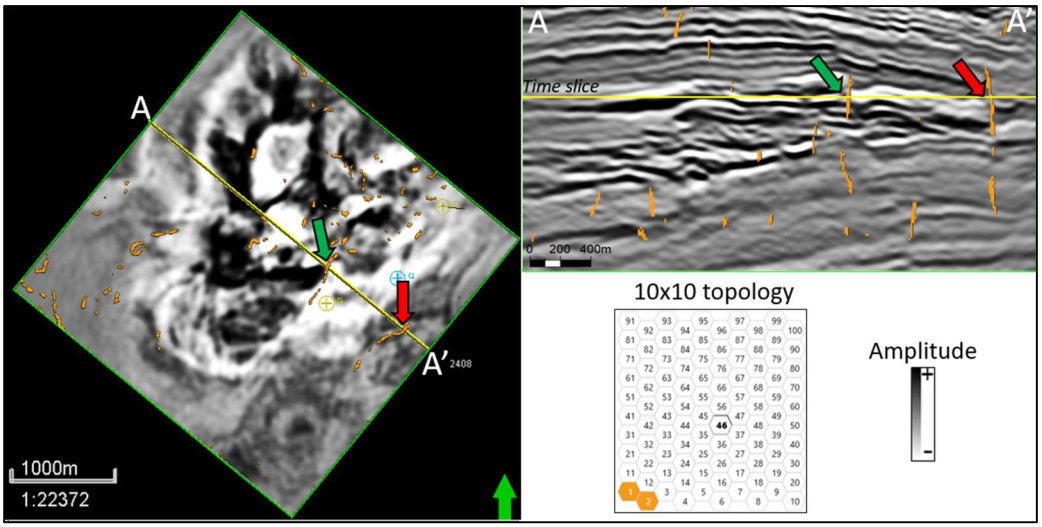


Figure 2. 10 – Comparison between the original amplitude volume and SOM in a time slice (left) and vertical section (right). The green and red arrows indicate fault planes described by specific neurons (orange color in the 10x10 topology).

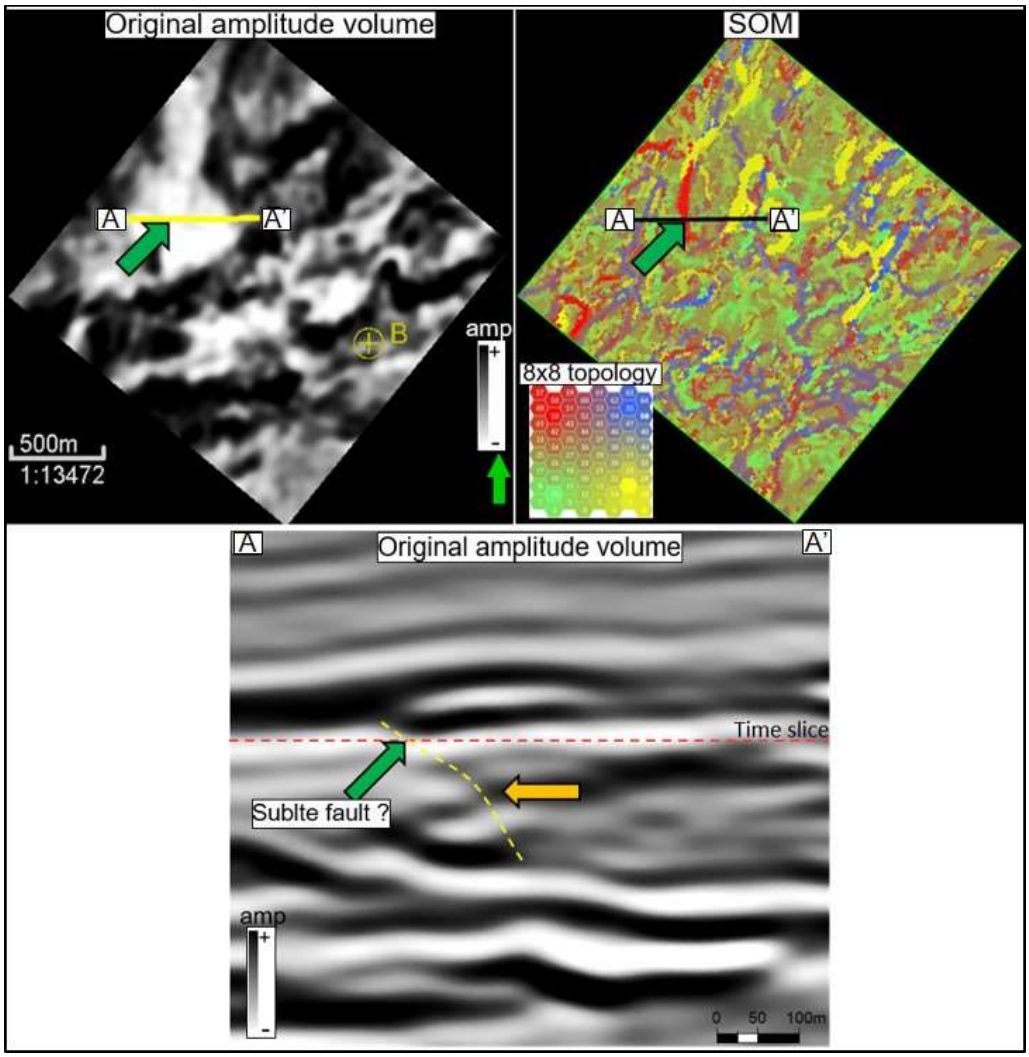


Figure 2. 11 – Comparison between the original amplitude volume (upper left) and the SOM classification (upper right) using a time slice. The discontinuity indicated in SOM colored in red is associated with a subtle change in the reflector's lateral continuity. Using the original amplitude volume is difficult to recognize this feature in a time slice (green arrow). SOM anomaly could reflect a subtle fault. The orange arrows indicate a possible vertical continuation of this subtle fault.

DISCUSSIONS

The interpretation of faults and fractures in the subsurface depends on the interpreter's experience, processing techniques, and attributes applied. The implementation of spectral balancing and Ormsby filter helped increase seismic reflectors' visualization in regions with weak impedance contrast. Another objective was to attenuate seismic noise. For that purpose, structure-oriented filtering enhances the data for improved fault detection. Some benefits observed within this research are similar to observations described by Fehmers and Hocker (2003), such as the attenuation of undulating reflections. It is necessary to highlight that various techniques can be used to prepare the seismic volumes for structural studies. Chopra et al. (2011b) list some examples of methods (median and mean filters, Radon filters) that can attenuate noise and acquisition footprint. Lyu et al. (2020a) apply adaptive subtraction to suppress footprint artifacts. Deconvolution, time-variant spectral whitening, inverse Q-filtering are examples of techniques described by these authors to enhance the spectral bandwidth. For Jubarte Field, spectral balancing and structure-oriented filtering improved the identification of the features of interest, but it is possible to see remaining seismic noise elements.

Good results for fault characterization were observed with the cosine of instantaneous phase, compared to other instantaneous attributes, as it displayed a discrete anomaly representing the discontinuities. Another positive aspect of the cosine of instantaneous phase is that it does not depend on the amplitude component (Chopra and Marfurt, 2015), which is particularly important in the Jubarte Field, where different amplitude contrasts occur, as observed in Figure 2.3. Compared to the instantaneous phase, the cosine of the instantaneous phase shows a continuous

change in the properties (Barnes, 2016). This characteristic avoids the presence of marks in the attribute visualization.

Considering the instantaneous attributes, the use of unsupervised machine learning techniques provided limited improvements. PCA shows the higher variability associated with RMS amplitude and envelope, but qualitative investigations reveal that these attributes were more appropriate for recognizing stratigraphic features. Zhao et al. (2015) describe limitations associated with cyclical attributes that should not be included in clustering studies. Self-organizing maps also have a limited potential for this group of attributes because they couldn't recognize specific neuron clusters associated with fault planes.

Curvature attributes highlighted subtle discontinuities in regions with small displacements, especially when computed with short-wavelength operators. After initial investigations, the structural curvature approach (first derivative of the structural dip components) was selected as the most appropriated method. Besides the orientation, curvature components can reveal footwall and hanging wall blocks within a deformation zone, as mentioned in Roberts (2001). That is a positive aspect that facilitates seismic interpretation, in particular, when working with time or horizons slices. One limitation of the short-wavelength approach is the enhanced noise elements in regions with a low signal-to-noise ratio.

Regarding the similarity attributes, different techniques and frequencies were evaluated. The energy-ratio similarity attribute reveals discontinuities with sharper limits than the features observed with the Sobel filter and outer product attributes. This characteristic represents an interesting aspect for a more accurate fault mapping. Broadband volumes define better the fault geometry (dip) compared to specific frequency intervals. Vertical faults are easier to characterize

than faults with lower dips. That tendency was described by Mai et al. (2009), and it is associated with the computation of vertical analysis windows that can results in stair-steps features when dipping events are present.

PCA results converge with this observation, indicating the broadband and multi-spectral volumes as having the higher variability. The exact eigenvalue should be considered with precaution because they can be affected by the noise content (even after the data conditioning). The unsupervised clustering using SOM shows interesting results with some faults defined by specific neurons. The volumes generated with SOM can complement the traditional interpretation workflow. However, they should not replace analysis based on the original amplitude volume because it has limitations representing faults with different dip.

CONCLUSIONS

The characterization of faults has many challenges, especially in regions with weak contrast of impedance. Seismic noise adds complexities to the seismic interpretation, especially when the discontinuities have different dips. This research demonstrates the advantages of combining data conditioning, multi-attributes investigation, and unsupervised machine learning techniques. Each method includes various parameters that will affect the final results. It is necessary to evaluate the attributes considering local aspects of the geology.

For the Jubarte Field post-salt section, the cosine of instantaneous phase provided good visualizations of the discontinuities, with precise and uniform anomalies not affected by changes in amplitude as observed with the envelope. One disadvantage of this attribute is the enhancement of noise close to the edges of the survey. Energy-ratio similarity shows faults with sharp limits

when computed with the full-stack data set, compared to individual frequency volumes. In the study area, curvature components computed with short-wavelength operators helped to delineate subtle features within the reservoir interval. Curvature was more affected by the noise content in the noise interval below the reservoir.

The variability indicated with PCA using geometric attributes shows an agreement with qualitative investigation using vertical sections and time slices. In combination with SOM, these techniques can be applied for structural purposes, optimizing faults' recognition. Lastly, it is essential to check the results in all the research phases, adding in-context interpretation to validate the features.

ACKNOWLEDGMENTS

The first author is extremely great full for Petrobras for founding my studies at OU and for the permission to publish this paper. I would like to thank ANP for the permission to use the data in my research. We also want to thanks Dr. Kurt Marfurt for the suggestions received during the development of this study. Also, to the AASPI consortium for the possibility to work with the software. In addition, thanks to Schlumberger, Geophysical Insights, and GeoSoftware-CGG for the software licenses and the University of Oklahoma for the laboratories.

REFERENCES

Aboaba, O., and C. Liner, 2020, Interpretation of Paleozoic paleokarst features in the Arkoma Basin of Oklahoma using 3D seismic and well logs: Interpretation, 8, no.2, T421-440,

Al-Dossary, S., and K. J. Marfurt, 2006, 3D volumetric multispectral estimates of reflector curvature and rotation: *Geophysics*, **71**, 5, 41-51.

Bahorich, M. S., and S. L. Farmer, 1995, 3-D seismic discontinuity for faults and stratigraphic features: The coherence cube: SEG Annual Meeting Abstract, 93-96.

Balabekov, Y., M. Sebastiao, R. Couto, P. Dariva, W. Lisboa, C. Reiser, and P. Johann, 2017, Permanent Reservoir Monitoring – 4D Quantitative Interpretation: 15th International Congress of the Brazilian Geophysical Society, SBGf, Expanded Abstracts, 1-6.

Barnes, A. E., 2016, Complex seismic trace analysis, *in*: Handbook of poststack seismic attributes, SEG, 45-74.

Barros, Caio, 2015, Internal processing report – 4D/4C Jubarte PRM. Unpublished.

Bezerra, M. F. C., C. Pedroso Jr., A. C. C., Pinto, and C. H. L. Bruhn, 2004, The appraisal and development plan for the heavy oil Jubarte Field, Deepwater Campos Basin, Brazil: *Offshore Technology Conference,* OTC16301, 1-5.

Bhattacharya, S., and S. Verma, 2019, Application of volumetric seismic attributes for complex fault network characterization on the North Slope, Alaska: *Journal of Natural Gas Science and Engineering*, **65**, 56-67.

Blaich, O. A., J. I. Faleide, and F. Tsikalas, 2011, Crustal breakup and continent-ocean transition at South Atlantic conjugate margins: *Journal of Geophysical Research*, **116**, 1-38.

Bulhões, E. M., and W. N. Amorim, 2005, Principio da SismoCamada Elementar e sua aplicacao a Tecnica Volume de Amplitudes (tecVA): 9th International Congress of the Brazilian Geophysical Society, 1-6. (in Portuguese)

Castro, R. D., J. P. Picolini, 2015, Main features of the Campos Basin Regional Geology, *in* Kowsmann, R. O., eds, Geology and Geomorphology: Elsevier, Habitats, **1**, 1-12.

Chenin, J., and H. Bedle, 2020, Multi-attribute machine learning analysis for weak BSR detection in the Pegasus Basin, Offshore New Zealand: Marine Geophysical Research, 41,1-21.

Chopra, S., and K. J. Marfurt, 2005, Seismic attributes – A historical perspective: *Geophysics*, **70**, 5, 1-47.

Chopra, S., and K. J. Marfurt, 2007a, Volumetric curvature attributes adding value to 3D seismic data interpretation: SEG Annual Meeting Abstract, 851-855.

Chopra, S., and K. J. Marfurt, 2007b, Seismic curvature attributes for mapping fault/fractures, and other stratigraphic features: CSEG Recorder, 37-41.

Chopra, S., and K. J. Marfurt, 2007c, Seismic attributes for prospect identification and reservoir characterization: SEG.

Chopra, S., and K. J. Marfurt, 2011a, Structural curvature versus amplitude curvature: 81th SEG Annual Meeting, Expanded Abstract, 980-984.

Chopra, S., S. Misra, and K. J. Marfurt, 2011b, Coherence and curvature attributes on preconditioned seismic data: *The Leading Edge*, **30**, 4, 386-393.

Chopra, S., and K. J. Marfurt, 2013, Structural curvature versus amplitude curvature: The Leading Edge, **32**, 2, 178-184.

Chopra, S., and K. J. Marfurt, 2014, Churning seismic attributes with principal component analysis: SEG Annual Meeting Abstract, 2672-2676.

Chopra, S., and K. J. Marfurt, 2015, Enhancing interpretability of seismic data with spectral decomposition phase components: SEG Annual Meeting Abstract, 1976-1980.

Chopra, S., and K. J. Marfurt, 2017, Volumetric fault image enhancement – Some applications: *Interpretation*, **5**, no.2, T151-T161.

Chopra, S., and K. J. Marfurt, 2018, Coherence attribute applications on seismic data in various guises: Unconventional Resources Technology Conference – URTeC:2886034, 1-9.

Coléou, T., M. Poupon, and K. Azbel, 2003, Unsupervised seismic facies classification: a review and comparison of techniques and implementation: The Leading Edge, 942-953.

Colodette, G., C. A. G. Pereira, C. A. M. Siqueira, G. A. S. M. Ribeiro, R. Rodrigues, J. S. Matos, and M. P. Ribeiro, 2007, The new deepwater oil and gas province in Brazil: Flow assurance and artificial lift: innovations for Jubarte Heavy Oil: OTC-19083, Expanded Abstracts, 1-9.

Coward, M P., E. G. Purdy, A. C. Ries, and D. G. Smith, 1999, The distribution of petroleum reserves in basins of the South Atlantic margins, *in* Cameron, N. R., R. H. Bate, and V. S. Clure, eds, The oil and gas habitats of the South Atlantic: Geological Society of London, 153, 101-131.

Damasceno, A., 2020, 4D quantitative interpretation of Jubarte Field (Brazil) – an integrated approach: M.S. thesis, Colorado School of Mines.

Dariva, P., W. L., Ramos Filho, C. C. Born, C. M. O. Falcone, and I. B. Zorzanelli, 2016, Monitoramento Sismico 4D no Campo de Jubarte, Bacia de Campos – Brasil: Congresso Brasileiro de Geologia.

Davison, I, 2007, Geology and tectonics of the South Atlantic Brazilian salt basins, *in* Ries, A. C., Butler, R. W. H., and Graham, R. H., eds., Deformation of the Continental Crust: The Legacy of Mike Coward: The Geological Society of London, **272**, 345-359.

Davison, I., L. Anderson, and P. Nuttall, 2012, Salt deposition, loading and gravity drainage in the Campos and Santos salt basins, *in* Alsop, G. I., Archer, S. G., Hartley, A. J., Grant, N. T., and Hodgkinson, R., eds, Salt Tectonics, Sediments and Prospectivity: The Geological Society of London, **363**, 159-173.

Davogustto, O., and K. J. Marfurt, 2011, Removing acquisition footprint from legacy data volumes: 81st SEG Annual Meeting Abstract, 1025-1029.

Del Rey, A.C., C.M.O. Falcone, J.G.R. da Silva, M.G.C. Meira, I.B. Zorzanelli, and R.A.B. Vieira, 2012, Jubarte Field 3D modeling based on the integration of outcrop analogs and elastic seismic attributes, *in* Norman, C.R., P. Weimer, S.M.C. dos Anjos, S. Henrickson, E. Marques, M. Mayall, R. Fillon, T. D'Agostino, A. Saller, K. Campion, T. Juang, R. Sarg, and F. Schroeder, eds, New understanding of the petroleum systems of continental margins of the world: Society for Sedimentary Geology, 32, 1-17.

Delgado, L., A. Batezelli, and J. Luna, 2018, Petroleum geochemical characterization of Albian-Oligocene sequences in the Campos Basin: "Case study: Eastern Marlin oilfield, offshore, Brazil": *Journal of South American Earth Sciences*, **88**, 715-735.

Demercian, S., P. Szatmari, and P. R. Cobbold, 1993, Style and pattern of salt diapirs due to thin-skinned gravitational gliding, Campos and Santos basins, offshore Brazil: *Tectonophysics*, **228**, 393-433.

Fehmers, G. C., and C. F. W. Hocker, 2003, Fast structural interpretation with structure-oriented filtering: *Geophysics*, **68**, 4, 1286-1293.

Fontanelli, P. De R., L. F. De Ros, and M. V. D. Remus, 2009, Provenance of deep-water reservoir sandstones from the Jubarte oil Field, Campos Basin, Eastern Brazilian Margin: *Marine and Petroleum Geology*, **26**, 1274-1298.

Guardado, L. R., B. Wolff, and J. A. S. L. Brandao, 1997, Campos Basin, Brazil, a Model for Production Atlantic Type Basins: Offshore Technology Conference, OTC-8484, Expanded Abstracts, 457-462.

Ha, T.N., K.J. Marfurt, B.C. Wallet, and B. Hutchinson, 2019, Pitfalls and implementation of data conditioning, attribute analysis, and self-organizing maps to 2D data: application to the Exmouth Plateau, North Carnarvon Basin, Australia: *Interpretation*, **7**, no.3, SG23-42.

Hart, B. S., 2011, Introduction to seismic interpretation: AAPG discovery series, **v.1.1**, no. 16.

Hill S. J., K. J. Marfurt, and S. Chopra, 2006, Searching for similarity in a slab of seismic data: The Leading Edge, 168-177.

Hoek, T. van., S. Gesbert, and J. Pickens, 2010, Geometric attributes for seismic stratigraphic interpretation: The Leading Edge, Special Section – Seismic Interpretation, 1056-1065.

Hussein, M., R. Stewart, and J. Wu, 2020, Unsupervised machine learning techniques for subtle fault detection: EAGE Annual Conference and Exhibition.

Hussein, M., R. Stewart, and J. Wu, 2021, Which seismic attributes are best for subtle fault detection?: *Interpretation*, **9**, 2, 1-21.

Jianguo, Y., Z. Qing, H. Liliang, 2015, Detection of strike-slip faults and fracture zones based on wide azimuth seismic data: SEG New Orleans Annual Meeting, 2967-2971.

Johann, P., D. D. Castro, and A. S. Barroso, 2001, Reservoir geophysics: seismic pattern recognition applied to ultra-deepwater oilfield in Campos Basin: SPE Latin American and Caribbean Petroleum Engineering Conference, SPE 69483 Extended Abstract, 1-13.

Kim, Y., R. Hardisty, and K.J. Marfurt, 2019, Attribute selection in seismic facies classification: application to a Gulf of Mexico 3D seismic survey and the Barnett Shale: Interpretation, 7, no.3, SE281-SE297.

Kang, H., J. Meng, T. Cheng, H. Jia, B. Bai, and M. Li, 2018, Characteristics of deep water depositional system in Campos Basin, Brazil: *Petroleum Exploration and Development*, **45**, 1, 99-110.

La Marca, K., 2020, Seismic attribute optimization with unsupervised machine learning techniques for deepwater seismic facies interpretation: users vs machines: M.S. thesis, University of Oklahoma.

Laudon, C., S. Stanley, and P. Santogrossi, 2019, Machine learning applied to 4D seismic data from the Denver-Julesburg Basin improves stratigraphic resolution in the Niobrara: Unconventional Resources Technology Conference, URTeC 337, 4353-4369.

Li, F., and W. Lu, 2014, Coherence attribute at different spectral scales: *Interpretation*, **2**, no.1,1-8.

Libak, A., B. Alaei, and A. Torabi, 2017, Fault visualization and identification in fault seismic attribute volumes: implications for fault geometric characterization: *Interpretation*, **5**, 2, B1-B16.

Liu, Z., C. Song, H. Cai, X. Yao, and G. Hu, 2017, Enhanced coherence using principal component analysis: Interpretation, 5, no.3, T351-359.

Lyu, B., J. Qi, G. Machado, F. Li, and K. J. Marfurt, 2019, Seismic fault enhancement using spectral decomposition assisted attributes: 89th SEG Annual Meeting Abstract, 1938-1942.

Lyu, B., J. Qi, S. Sinha, J, Li, and K. J. Marfurt, 2020a, Improving fault delineation using maximum entropy multispectral coherence: *Interpretation*, **8**, no. 4, T835-T850.

Lyu, B., Qi, J., F. Li, Y. Hu., T. Zhao, S. Verma, and K. J. Marfurt, 2020b, Multispectral coherence: Which decomposition should we use?: *Interpretation*, **8**, no. 1, T115-T129.

Lou, Y., B. Zhang, T. Lin, and D. Cao, 2020, Seismic horizon picking by integrating reflector dip and instantaneous phase attributes: Geophysics, **85**, no. 2, O37-O45.

Luo, Y., S. Al-Dossary, M. Marhoon, and M. Alfaraj, 2003, Generalized Hilbert transform and its applications in geophysics: *The Leading Edge*, **22**, 3, 1-12.

Mai, H. T., K. J. Marfurt, and S. Chavez-Perez, 2009, Coherence and volumetric curvatures and their spatial relationship to faults and folds, an example from Chicontepec basin, Mexico: SEG International Exposition and Annual Meeting, Expanded Abstract, 1063-1067.

Marfurt, K. J., 2014, Seismic attributes and the road ahead: 84th SEG Annual Meeting, Expanded Abstract, 4421-4426.

Marfurt, K. J., and T. M. Alves, 2015, Pitfalls and limitations in seismic attribute interpretation of tectonic features: *Interpretation*, **3**, no.1, A5-A15.

Marfurt, K. J., R. M. Scheet, J. A. Sharp, and M. G. Harper, 1998a, Suppression of the acquisition footprint for seismic sequence attribute mapping: *Geophysics,* **63**, no.3, 1024-1035.

Marfurt, K. J., R. L., Kirlin, S. L. Farmer, and M. S. Bahorich, 1998b, 3-D seismic attributes using a semblance-based coherency algorithm: *Geophysics*, **63**, 4, 1150-1165.

Matos, M. C., K. J. Marfurt, and P. R. S. Johann, 2009, Seismic color Self-Organizing Maps: 11th International Congress of the Brazilian Geophysical Society, SBGf, Expanded Abstracts, 914-917.

Milani, E. J., H. D. Rangel, G. V. Bueno, J. M. Stica, W. R. Winter, J. M. Caixeta, O. C. Pessoa Neto, 2007, Bacias Sedimentares Brasileiras – Cartas estratigraficas, in: Boletim de Geosciencias da Petrobras, **15** (2), 183-205.

Mohriak, W., M. Nemcok, and G. Enciso, 2008, South Atlantic divergent margin evolution: rift-border uplift and salt tectonics in the basins of SE Brasil, *in* Pankhurst, R. J., R. A. J. Trouw, B. B. Brito Neves, and M. J. Wit, eds., West Gondwana: pre-cenozoic correlations across the south Atlantic region. Geological Society of London, 294, 365-398.

Mohriak, W. U., P. Szatmari, and S. Anjos, 2012, Salt: geology and tectonics of selected Brazilian basins in their global context*, in* Alsop, G. I., Archer, S. G., Hartley, A. J., Grant, N. T., and Hodgkinson, R., eds, Salt Tectonics, Sediments and Prospectivity: The Geological Society of London, **363**, 121-158.

Mora, J.P., H. Bedle, and K. J. Marfurt, 2020, Constructing fault surface objects from fault sensitive attributes: SEG International Exposition and 90th Annual Meeting, Expanded Abstracts, 1160-1164.

Ojeda, H. A. O., 1982, Structural framework, stratigraphy, and evolution of Brazilian Marginal Basins, *The American Association of Petroleum Geologists Bulletin*, **66**, no. 6, 732-749.

Phillips, M., and S. Fomel, 2017, Plane-wave Sobel attribute for discontinuity enhancement in seismic images: *Geophysics*, **82**, no.6, WB63-WB69.

Qi, J., B. Lyu, A. AlAli, G. Machado, Y. Hu. And K. J. Marfurt, 2019, Image processing of seismic attributes for automatic fault extraction: Geophysics, **84**, no.1, O25-O37.

Radovich, B. J., and R. B. Oliveros, 2018, 3-D sequence interpretation of seismic instantaneous attributes from the Gorgon Field: The Leading Edge, 1286-1293.

Rijks, E. J. H., and J. C. E. M. Jauffred, 1991, Attribute extraction: an important application in any detailed 3-D interpretation study: *The Leading Edge*, **10**, 11-19.

Roberto, M., A. B. Coutinho, and A. R. Dos Santos, 2018, Campos Basin Technologies Yard: 40 Years of Lessons Learned: Offshore Technology Conference, OTC-28716-MS, Expanded Abstracts, 1-31.

Roberts, A., 2001, Curvature attributes and their application to 3D interpreted horizons: First break, **19,** no.2, 85-100.

Roden, R., T. Smith, and D. Sacrey, 2015, Geologic pattern recognition from seismic attributes: Principal component analysis and self-organizing maps: Interpretation, **3**, no. 4, SAE59-SAE83.

Rosa, A. L. R., 2018, Analise do sinal sismico, Sociedade Brasileira de Geofisica (SBGf), 713 p. (in Portuguese)

Sarhan, M. A., 2017, The efficiency of seismic attributes to differentiate between massive and non-massive carbonate successions for hydrocarbon exploration activity: NRIAG *Journal of Astronomy and Geophysics*, **6**, 311-325.

Taner, M. T., F. Koehler, and R. E., Sheriff, 1979, Complex seismic trace analysis: *Geophysics*, **44**, no. 6, 1041-1063.

Tarcha, B. A., R. G. Furtado, O. C. Borges, L. Vergara, A. I. Watson, and G. T. Harris, 2016, Subsea ESP Skid Production System for Jubarte Field: Offshore Technology Conference, OTC-27138-MS, Expanded Abstracts, 1-20.

Thedy, E. A., W. L. Ramos Filho, J. R. R. da Silva, S. Seth, and S. Maas, 2011, Challenges for Jubarte Permanent Seismic System: 12th International Congress of the Brazilian Geophysical Society, SBGf, Expanded Abstracts, 1379-1382.

Thedy, E. A., P. Dariva, W. L. Ramos Filho, P. O. Maciel Jr., F. E. F. Silva, and I. B. Zorzanelli, 2015, Initial Results on Permanent Reservoir Monitoring in Jubarte, Offshore Brazil: 14th International Congress of the Brazilian Geophysical Society, SBGf, Expanded Abstracts, 838-841.

Tingdahl, K., and N. Hemstra, 2003, Estimating Fault-attribute orientation with gradient analysis, principal component analysis and the localized Hough-transform: SEG Technical Program Expanded Abstract.

Valdez, M., 2019, Fault mapping in 3D seismic reflection data using seismic attributes and velocity anisotropy: example from west Virginia: M. S. thesis, Montana Tech.

Zhao, T., V. Jayaram, A. Roy, and K. J. Marfurt, 2015, A comparison of classification techniques for seismic facies recognition: *Interpretation*, **3**, no. 4, SAE29-SAE58.

White, R. E., 1991, Properties of instantaneous seismic attributes: Geophysics: The Leading Edge, 26-32.

Winter, W. R., R. J. Jahnert, A. B. Franca, 2007, Bacia de Campos, in: Boletim de Geosciencias da Petrobras, **15** (2), 511-529.

CHAPTER 3 – COMBINING AZIMUTHAL VOLUMES, ENERGY-RATIO ATTRIBUTE, AND MACHINE LEARNING TO INVESTIGATE FAULTS IN THE JUBARTE FIELD, CAMPOS BASIN

Edimar Perico[12], Heather Bedle[2], and Andrea Damasceno[1]

1 Petrobras

2 University of Oklahoma

Keywords: faults, azimuth, attributes, machine learning, and noise

This chapter includes an expanded abstract submitted to the SEG21 convention

SUMMARY

Seismic attributes represent a powerful tool to improve the identification of geological elements in the subsurface. The recognition of faults and fractures commonly includes geometric attributes. This study compares the response of the energy-ratio similarity (ERS) attribute calculated from different stacks of azimuth sectors. We use the Jubarte Permanent Reservoir Monitoring (PRM) system acquisition as a case study to evaluate the impact of the acquisition sectors on the seismic attribute response. The results show that the full azimuth stack data is less affected by seismic noise. Also, the fault geometry is better delineated using this volume compared to individual azimuth sectors. Another positive aspect is the higher lateral continuity of the discontinuities, which looks more rectilinear and uniform when using the full azimuth stack volume. Local improvements obtained with individual azimuth volumes are associated with discontinuities positioned perpendicular to the acquisition direction. The principal component

analysis (PCA) revealed the higher variability associated with the full azimuth stack volume. The second principal component highlights features close to the edge of the survey, and it is more affected by noise components. Self-organizing maps (SOM) reveal some anomalies associated with faults surfaces. The method has some limitations when evaluated in vertical sections, such as the impact of noise and the difficulty to delineate not vertical faults (stair-step features). However, this unsupervised clustering method can be used as a complementary method to improve the recognition of faults using seismic attributes, especially during the recognition of an area.

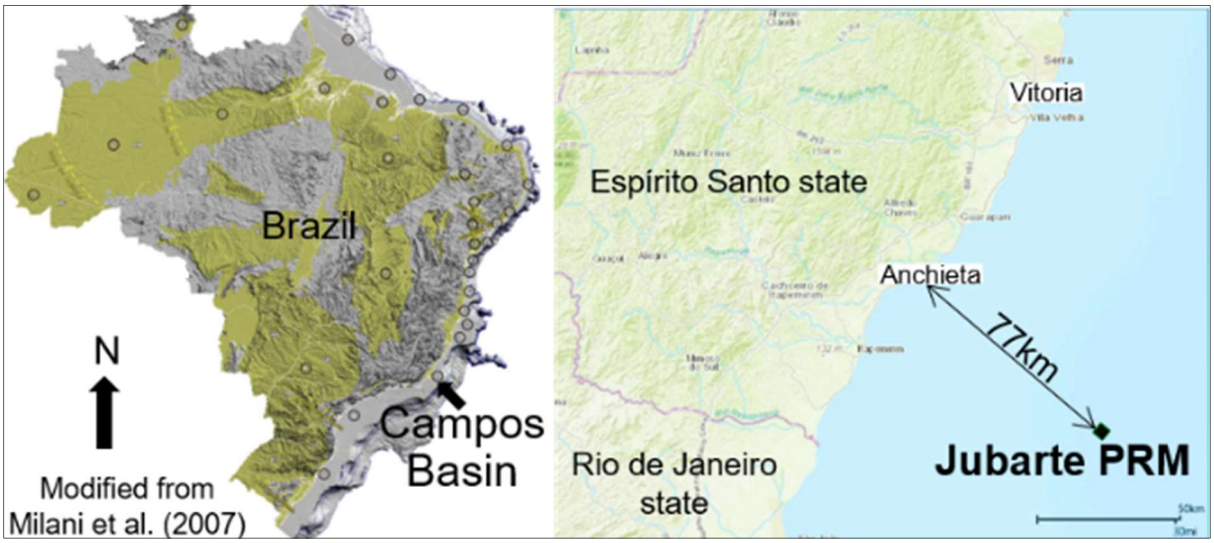


Figure 3. 1 – Left: Location of the Campos Basin along the eastern Brazilian margin. After Milani et al. (2007). Right: Position of the Jubarte PRM seismic acquisition, offshore Brazil.

INTRODUCTION

The interpretation of faults within seismic reflection data sets depends on many factors. The experience of the geoscientist is one of them. Considering the seismic acquisition

configurations, multi and wide-azimuth styles can improve the illumination of geological surfaces in complex geological settings (Long et al., 2006). Also, algorithms applied during the processing of seismic volumes can enhance some characteristics associated with structural discontinuities. Examples of features that identify cracks are changes in the amplitude, phase, and signal/noise ratio (Marfurt et al., 1998; Chopra et al., 2000; Hart, 2011). In practice, it is common to use lines oriented perpendicular to the fault of interest to map the discontinuity. Taner et al. (1979) and Chopra et al. (2000) describe the difficulty associated with recognizing faults parallel to the strike of the sediments. Mueller et al. (2010) studied two methods (conventional azimuth sectors vs. Common Cartesian Offset Bin – CCOB) to see improvements for fault identification in a carbonate field in the Middle East. The objective was to better characterize the permeability pathways associated with faults. Jianguo et al. (2015) applied azimuth-oriented filtering to increase the S/N ratio and improve the identification of fault and fracture zones based on wide azimuth data acquired in China. Chopra and Marfurt (2007) describe the advantages of using azimuths oriented perpendicular and parallel to the fault zones of interest. This study aims to compare the responses of different azimuth sector stacks that imaged the southeastern part of the Jubarte Field (Figure 3.1). The area has different contrasts of amplitude and seismic noise. Cross-correlation represents one type of operation that highlights discontinuities (Taner et al., 1979). Semblance-based coherency and Sobel filter are other attributes that emphasize discontinuities (Hill et al., 2006). Azimuthal variation is important to characterize conventional reservoirs and unconventional resources, as Trumbo and Rich (2013) described for induced fractures.

GEOLOGICAL SETTING

The study area is located offshore, in the northern part of the Campos Basin. The origin of the basin is associated with the separation of South America and Africa (Mohriak et al., 2008; Blaich et al., 2011). Important elements to understand the regional evolution are volcanic rocks and evaporitic deposits because they control the formation of some depocenters. The deformational structures related to salt movements controlled the hydrocarbon distribution of pre and post-salt deposits (Mohriak et al., 2012). The interval evaluated in this research has Maastrichtian age and belongs to the drift phase of Campos Basin's evolution (Winter et al., 2007).

On a local scale, Fontanelli et al. (2009) demonstrate the importance faults have, for instance, controlling the distribution of different rock intervals. Thedy et al. (2011) mention the difficulty associated with subtle faults' characterization using 3D seismic data sets. Bezerra et al. (2004) describe an extensional fault controlling the eastern termination of the field.

Other publications discuss additional aspects of the Jubarte Field. Daher Jr et al. (2007) and Fontanelli et al. (2009) describe textural and mineralogical elements of the reservoir, and Gontijo et al. (2015) indicate the geometry associated with the deposits. Thedy et al. (2015) and Dariva et al. (2016) describe amplitude responses obtained close to producer and injector wells. Balabekov et al. (2017) demonstrate improvements in the characterization of various properties using pre-stack Bayesian inversion. Damasceno (2020) reveals corrections to be applied within partial stack volumes to improve the amplitude variation with angle (AVA) analysis and shows the advantages of using joint PP-PS inversion (instead of conventional PP only) to refine 4D inversion outputs.

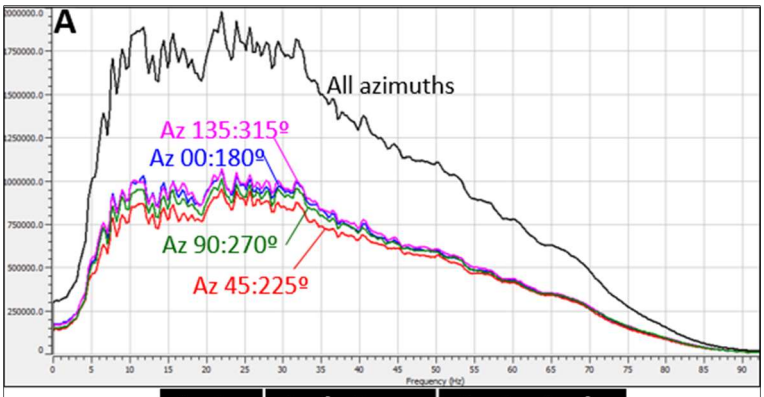
To improve seismic facies analysis and reservoir characterization in Campos Basin, Johann et al. (2001) use unsupervised and supervised techniques to classify seismic data amplitudes. Examples of applications of PCA and SOM in geosciences include Liu et al. (2017) and Hussein (2021). Principal component analysis indicates attributes with the most variability and is commonly applied to reduce dimensionality (Coléou et al., 2003). Self-organizing maps cluster the attributes into different classes that can display geological features, such as hydrocarbon contacts, reservoir extension, and fault systems (Roden et al., 2015; Laudon et al., 2019).

DATA AND METHODS

The present study uses PP-wave volumes from Jubarte PRM system seismic acquisition, covering the South-East portion of the Jubarte field. It is a 4D project that registered different seismic surveys. The volumes applied within this investigation belong to Monitor-01. The acquisition used optical cables situated on the seafloor, with 300 m spacing between the cables in an area of 9 km^2 (Thedy et al., 2015; Dariva, 2016; Damasceno, 2020). Three accelerometers and one hydrophone compose the sensors, and the processing included pre-stack VTI Kirchhoff depth migration (Barros, 2015, processing report).

We cropped the data sets to the interval of interest (Upper Cretaceous) to optimize the attributes computation, PCA, and SOM analyses. The first comparison performed was to check the amplitude spectrums of the azimuth volumes (Figure 3.2 A). The full azimuth stack amplitude volume demonstrates a broader spectrum compared to the individual azimuth sector datasets. This characteristic will be important to understand the attributes' responses. Figure 3.2 B synthesizes the four azimuthal sectors, indicated by their angle range and center angle.

The ERS is a geometric attribute that compares adjacent traces taking into account the regional dip, a critical aspect to enhance the discontinuities of interest associated with faults and fractures. The ERS computation uses the Hilbert transform and covariance matrix. We also compare the results obtained from different azimuthal sector stacks and unsupervised machine learning techniques to test if these techniques can provide additional insights over traditional interpretation methods.



B

Sector	Angle Range	Center Angle
1	335-025	0
1	155-205	180
2	020-070	045
2	200-250	225
3	065-115	090
3	245-295	270
4	110-160	135
4	290-340	315

Figure 3. 2 - (A) Comparison of the azimuth stack sectors and the full azimuth stack volume. Full azimuth stack volume has a broader spectrum compared to individual azimuth data sets. (B) Azimuthal sectors and associated angle range and center angle (Barros, 2005, processing report).

RESULTS

One way to compare the results is using vertical sections (Figure 3.3). The amplitude data (blue and red color bar) is corendered with the ERS attributes for different azimuth sectors. The full azimuth stack data (upper section) contains less seismic noise features. Also, the fault geometry is better defined in this case (yellow arrows). The white boxes show areas where it is possible to see higher noise elements in individual azimuthal volumes. The green arrow points to a region strongly affected by noise close to the survey's edge, with low seismic traces multiplicity. The area includes chaotic deposits (orange arrows) that will also result in lower similarity features.

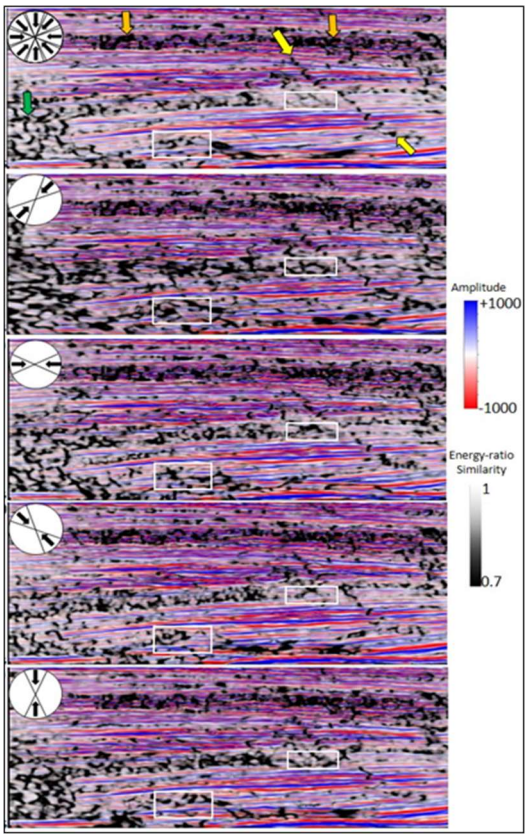


Figure 3. 3 – Comparison between the energy-ratio similarity attribute computed with the full azimuth stack volume (upper vertical section) and individual azimuth sectors (45-225º; 90-270º; 135-315º, and 0-180º). The full azimuth stack volume has less seismic noise, and it is easy to identify the fault (yellow arrows). The vertical section is displaying 1400ms of time.

Looking in time slices, the full-stack azimuth data results in more evident and rectilinear discontinuities (Figure 3.4). Figure 3.5 A shows two NE-SW faults in more detail using a 3D window. The yellow arrow shows a more uniform fault surface in the full azimuth stack cube. The other arrows indicate punctual improvements observed with individual azimuth cubes. For example, the orange indicates improvement obtained with the azimuth sector 135-315º. This fault segment is oriented perpendicular to the acquisition direction and shows higher lateral continuity.

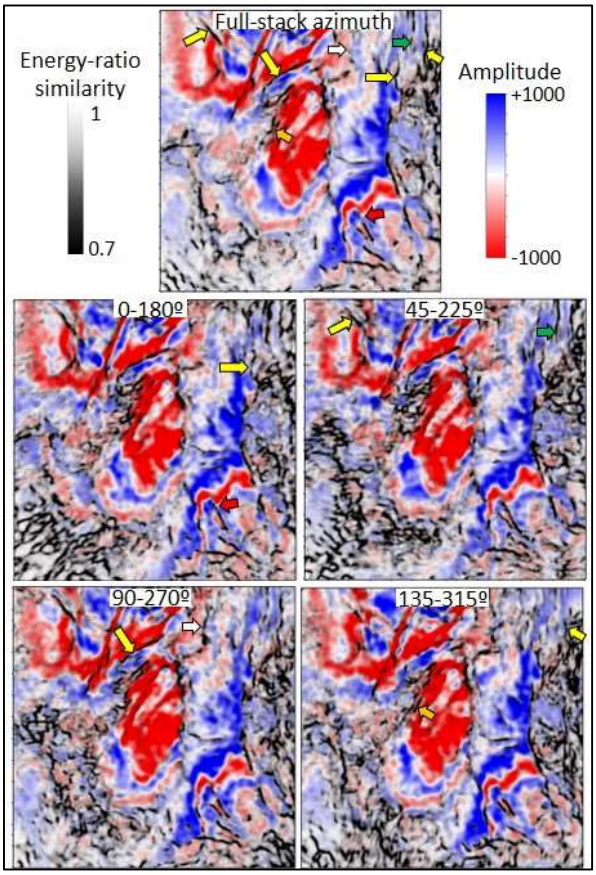


Figure 3. 4 – Comparison between the energy-ratio similarity attribute computed with the full azimuth stack volume (upper time slice) and the individual azimuth sectors. The yellow arrows show regions where the full-stack azimuth results in more linear features. Arrow with other colors demonstrate improvements obtained locally for each azimuth sector (red for 0-180º, green for 45-225º, white for 90-270º, and orange for 135-315º).

Regarding the PCA, the first principal component shows that the ERS estimated from the full azimuth stack volume is the attribute with a higher contribution when compared to the other azimuthal stacks (Figure 3.5 B). This tendency was noted using different observation windows, with different lateral and vertical sizes (Appendix M).

The results show higher eigenvalues for the first principal component (higher variability) toward the survey center. On the other hand, the second principal component displays higher eigenvalues close to the survey's edge, demonstrating a solid relation with noise components (Appendix N).

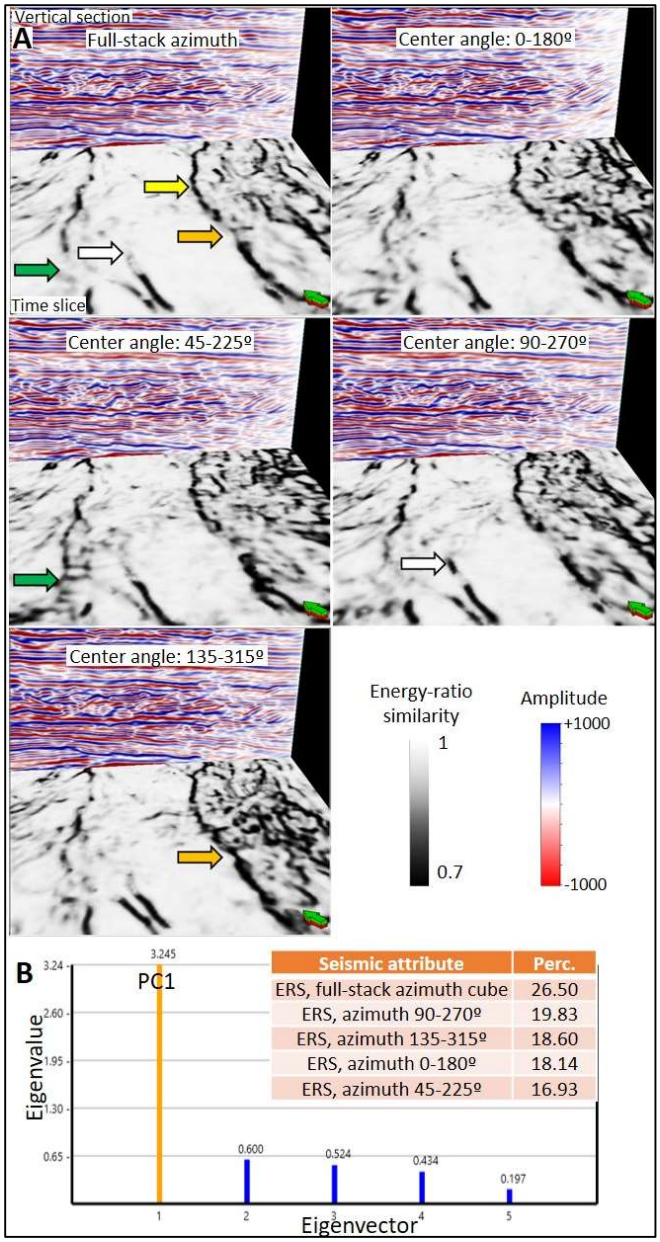


Figure 3. 5 – (A) Comparison between the full azimuth stack and individual azimuth sectors. The ERS attribute is displayed using black and white color bar in the time slice, while the seismic amplitude stacks are shown in the vertical slice. The yellow arrow exemplifies a fault segment where it is possible to see a more rectilinear and uniform discontinuity. Additional arrows demonstrate improvements obtained locally for each azimuth sector (green for 45-225º, white for 90-270º, and orange for 135-315º). (B) PCA results for the first principal component. The higher contribution is defined by the ERS attribute computed with the full-stack azimuth volume.

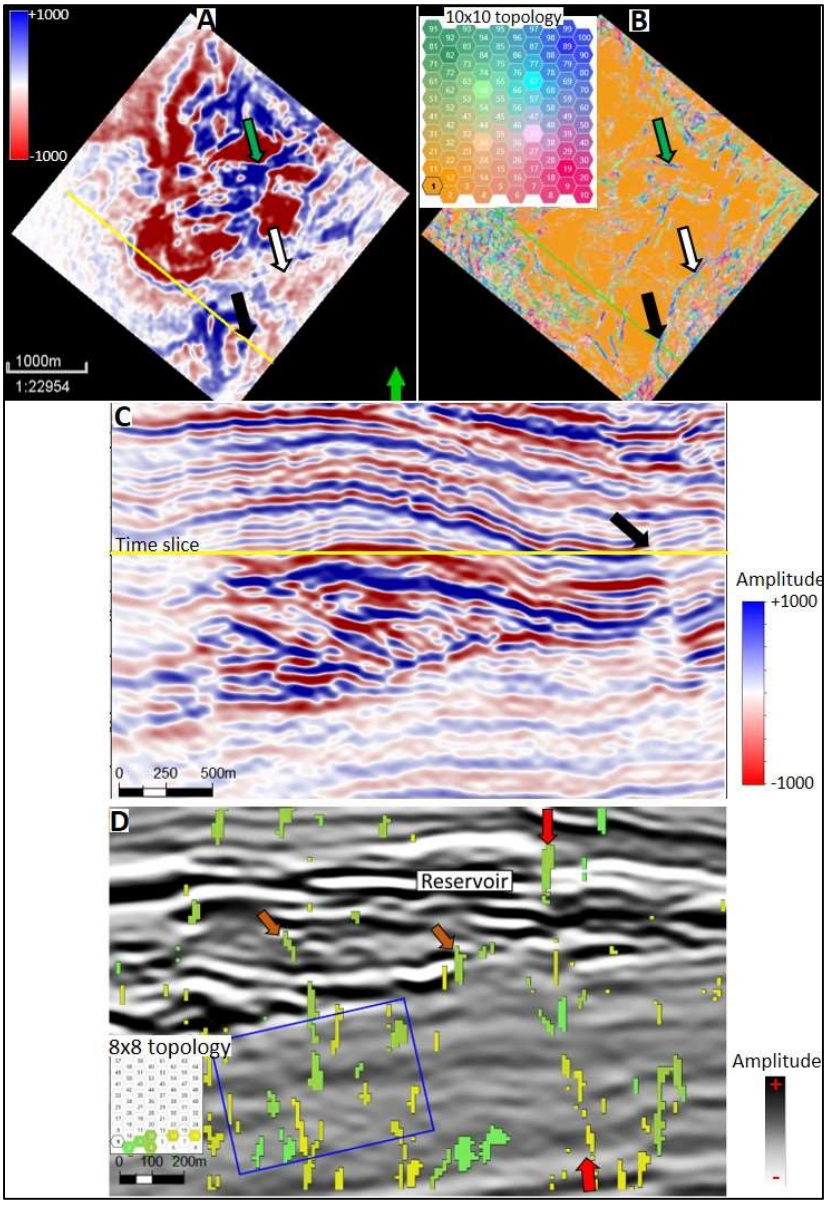


Figure 3. 6 – (A and B) Comparison between the original amplitude volume and SOM in a time slice. The black arrows indicate a fault. (C) Vertical section displayed in A and B with the location of the analyzed fault. (D) Another vertical section comparing the original amplitude volume (black and white color bar) and SOM results (8x8 topology). Note that the selected neurons indicate a fault plane within the reservoir (red arrow) and minor stratigraphic termination (brown arrow). The same vectors are also associated with seismic noise components in the interval below.

DISCUSSIONS AND CONCLUSIONS

The results show that faults are better delineated using the full azimuth stack volume. Vertical sections and time slices show less seismic noise and better delineation of the fault geometry using the full azimuth stack data. Mueller et al. (2010) also mention the higher levels of background noise associated with individual azimuth sectors. Lower similarity features are more rectilinear and uniform using this volume. Individual azimuthal volumes result in local improvements, especially when cracks are oriented perpendicular to the acquisition direction (e.g., orange arrow in Figure 3.5 A). We consider full azimuthal stack volume appropriate for the initial recognition of the discontinuities. Individual azimuthal cubes can complement the analysis with more detailed features. PCA results show agreement with the qualitative observation that it is beneficial to use the full azimuth stack cube. This observation possibly reflects the broader amplitude spectrum. This was confirmed when the original amplitude volumes were used as input for PCA. The higher variability is controlled mainly by the full-stack amplitude volume. The difference between the first and second eigenvalues is higher when looking at the amplitude data compared to the energy-ratio results. This characteristic reflects possible the window-based approach used to generate the attributes (Appendix O).

SOM combines different azimuthal stacks favoring fault identification. Further investigations are necessary to attenuate the impact of seismic noise. Figure 3. 6D shows SOM defined faults within the reservoir interval (red arrow), but also local stratigraphic features (brow arrows), and more critically, seismic components in the interval below (blue box).

ACKNOWLEDGMENTS

The first author thanks Petrobras for funding my studies at OU and providing the seismic data set. I would like to thank ANP for the permission to use the data in my research. We also thank the AASPI consortium for the software used to compute the attributes and Dr. Marfurt for the suggestions and comments. Thanks to Schlumberger, Geophysical Insights, and GeoSoftware-CGG for the software licenses and the University of Oklahoma for the laboratories.

REFERENCES

Balabekov, Y., M. Sebastiao, R. Couto, P. Dariva, W. Lisboa, C. Reiser, and P. Johann, 2017, Permanent Reservoir Monitoring – 4D Quantitative Interpretation: 15th International Congress of the Brazilian Geophysical Society, SBGf, Expanded Abstracts, 1-6.

Bezerra, M. F. C., C. Pedroso Jr., A. C. C., Pinto, and C. H. L. Bruhn, 2004, The appraisal and development plan for the heavy oil Jubarte Field, Deepwater Campos Basin, Brazil: Offshore Technology Conference, OTC16301, 1-5.

Blaich, O. A., J. I. Faleide, and F. Tsikalas, 2011, Crustal breakup and continent-ocean transition at South Atlantic conjugate margins: Journal of Geophysical Research, **116**, 1-38.

Chopra, S., V. Sudhakar, G. Larsen, and H. Leong, 2000, Azimuth-based coherence for detecting faults and fractures: World Oil, 57-62.

Chopra, S., and K. J. Marfurt, 2007, Seismic attributes for prospect identification and reservoir characterization: SEG.

Coléou, T., M. Poupon, and K. Azbel, 2003, Unsupervised seismic facies classification: a review and comparison of techniques and implementation: The Leading Edge, **22**, no.10, 942-953.

Daher Jr. B., C. A. M. Siqueira, I. Nascimento, I. A. Pinto, J. B. Farias, R. A. B. Vieira, 2007, Jubarte Field – Development Strategy: Offshore Techonology Conference, OTC 19088, 1-5.

Damasceno, A., 2020, 4D quantitative interpretation of Jubarte Field (Brazil) – an integrated approach: M.S. thesis, Colorado School of Mines.

Dariva, P., W. L., Ramos Filho, C. C. Born, C. M. O. Falcone, and I. B. Zorzanelli, 2016, Monitoramento Sismico 4D no Campo de Jubarte, Bacia de Campos – Brasil: Congresso Brasileiro de Geologia.

Fontanelli, P. De R., L. F. De Ros, and M. V. D. Remus, 2009, Provenance of deep-water reservoir sandstones from the Jubarte oil Field, Campos Basin, Eastern Brazilian Margin: Marine and Petroleum Geology, **26**, no. 7, 1274-1298.

Gontijo, R. C., C. E. Souza Cruz, J. L. L. Caldas, L. M. Arienti, R. S. F. D'Avila, 2005, Structurally controlled sand-rich gravity deposits of the Jubarte Oil Field (Brazil deep-water sedimentation on the Southeast Brazilian Margin Project): AAPG Annual Meeting, Abstract.

Hart, B. S., 2011, Introduction to seismic interpretation: AAPG discovery series, **v.1.1**, no. 16, CD-ROM.

Hill S. J., K. J. Marfurt, and S. Chopra, 2006, Searching for similarity in a slab of seismic data: The Leading Edge, **25**, 168-177.

Hussein, M., R. Stewart, and J. Wu, 2021, Which seismic attributes are best for subtle fault detection?: Interpretation, **9**, 2, 1-21.

Jianguo, Y., Z. Qing, H. Liliang, 2015, Detection of strike-slip faults and fracture zones based on wide azimuth seismic data: SEG New Orleans Annual Meeting, 2967-2971.

Johann, P., D. D. de Castro, and A. S. Barroso, 2001, Reservoir geophysics: seismic pattern recognition applied to ultra-deepwater oilfield in Campos Basin, offshore Brazil: SPE Latin American and Caribbean Petroleum Engineering Conference: SPE 69483, 1-13.

Laudon, C., S. Stanley, and P. Santogrossi, 2019, Machine learning applied to 4D seismic data from the Denver-Julesburg Basin improves stratigraphic resolution in the Niobrara: Unconventional Resources Technology Conference, URTeC 337, 4353-4369.

Liu, Z., C. Song, H. Cai, X. Yao, and G. Hu, 2017, Enhanced coherence using principal component analysis: Interpretation, **5**, no.3, T351-359.

Long, A. S., W. Pramik, E. Fromyr, R. Laurin, and C. Page, 2006, Multi-azimuth and wide-azimuth lessons for better seismic imaging in complex settings: ASES Extended Abstracts, 1-5.

Marfurt, K. J., R. M. Scheet, J. A. Sharp, and M. G. Harper, 1998, Suppression of the acquisition footprint for seismic sequence attribute mapping: Geophysics, **63**, no.3, 1024-1035.

Milani, E. J., H. D. Rangel, G. V. Bueno, J. M. Stica, W. R. Winter, J. M. Caixeta, O. C. Pessoa Neto, 2007, Bacias Sedimentares Brasileiras – Cartas estratigraficas: Boletim de Geosciencias da Petrobras, **15,** no. 2, 183-205.

Mohriak, W., M. Nemcok, and G. Enciso, 2008, South Atlantic divergent margin evolution: rift-border uplift and salt tectonics in the basins of SE Brasil, *in* Pankhurst, R. J., R. A. J. Trouw, B. B. Brito Neves, and M. J. Wit, eds., West Gondwana: pre-cenozoic correlations across the south Atlantic region. Geological Society of London, 294, 365-398.

Mohriak, W. U., P. Szatmari, and S. Anjos, 2012, Salt: geology and tectonics of selected Brazilian basins in their global context*, in* Alsop, G. I., Archer, S. G., Hartley, A. J., Grant, N. T., and Hodgkinson, R., eds., Salt Tectonics, Sediments and Prospectivity: The Geological Society of London, 363, 121-158.

Mueller, K. W., M. S. Al Nahhas, W. L. Soroka, M. al Baloushi, R. Sinno, R. D. Martinez, W. Hussein, and P. LeCocq, 2010, Azimuthal seismic pilot for fault and fracture dectection – an Abu Dhabi, U.A.E. case study: Adu Dhabi International Petroleum Exhibition & Conference, SPE 137338.

Taner, M. T., F. Koehler, and R. E., Sheriff, 1979, Complex seismic trace analysis: Geophysics, **44**, no. 6, 1041-1063.

Thedy, E. A., W. L. Ramos Filho, J. R. R. da Silva, S. Seth, and S. Maas, 2011, Challenges for Jubarte Permanent Seismic System: 12th International Congress of the Brazilian Geophysical Society, SBGf, Expanded Abstracts, 1379-1382.

Thedy, E. A., P. Dariva, W. L. Ramos Filho, P. O. Maciel Jr., F. E. F. Silva, and I. B. Zorzanelli, 2015, Initial Results on Permanent Reservoir Monitoring in Jubarte, Offshore Brazil: 14th International Congress of the Brazilian Geophysical Society, SBGf, Expanded Abstracts, 838-841.

Trumbo, A., and J. P. Rich, 2013, Azimuthal variations in attributes for induced fracture detection in the Barnett Shale: *Intrepretation*, **1**, no. 2, SB51-SB59.

Roden, R., T. Smith, and D. Sacrey, 2015, Geologic pattern recognition from seismic attributes: Principal component analysis and self-organizing maps: Interpretation, **3**, no. 4, SAE59-SAE83.

Winter, W. R., R. J. Jahnert, A. B. Franca, 2007, Bacia de Campos, in: Boletim de Geosciencias da Petrobras, **15** (2), 511-529.

CHAPTER 4 – DISCUSSIONS AND CONCLUSIONS

The characterization of faults and fractures using seismic datasets has a wide range of applications. This research integrates preconditioning, seismic attributes, and unsupervised machine learning techniques to improve the recognition of structural discontinuities. The southeastern part of the Jubarte Field has faults with different seismic signatures due to variations in the geology, acoustic impedance contrasts, and seismic noise content.

I noticed that a single attribute was insufficient to highlight all the aspects of deformational zones in the Jubarte PRM acquisition area. Better results were obtained by combining methods and attributes in different phases of the workflow. Based on the results obtained, I will answer the initial motivational questions.

► What methods can be applied during the data conditioning phase to improve the recognition of faults?

I followed the workflow described by Ha et al. (2019) that includes the spectral balancing and structure-oriented filter. The volumes after data conditioning show seismic reflectors with higher lateral continuity and less random noise. The Jubarte Field faults are more visible after the data conditioning because higher contrasts are observed. Libak et al. (2017) also noted this characteristic when studying the Norwegian Barents Sea. These authors also described fault segmentation issues that are associated with the dominant period of the seismic data. Variations in the Jubarte Field's dominant frequency, as noted within the possible changes in the resolution

(Figure 1.10), impact the lateral variations of subtle faults within the Jubarte area, as observed in Figure 3.4.

► Which seismic attributes better delineate faults and fractures?

Cosine of instantaneous phase provided good results within the instantaneous group, as demonstrated with Figure 2.3. Barnes (2016) mentions two important aspects of this attribute that were helpful to identify faults in the study area: (1) it has continuous values and (2) it is not impacted by changes in amplitude. AVT is an interesting attribute but locally it is impacted by low frequencies, an aspect also described in Lyu et al. (2020). Energy-ratio similarity revealed discontinuities with sharper limits, as observed within Figure 2.6. Another example of improvement obtained for fault identification in the Jubarte Field can be seen in Figure 4.1, where it is difficult to track the lateral continuity of the fault (green arrow) in a time slice. Close to the reservoir's base, the fault surface has no apparent contrast in the vertical section but using the energy-ratio similarity attribute, the interpreters can recognize features associated with that fault more confidently.

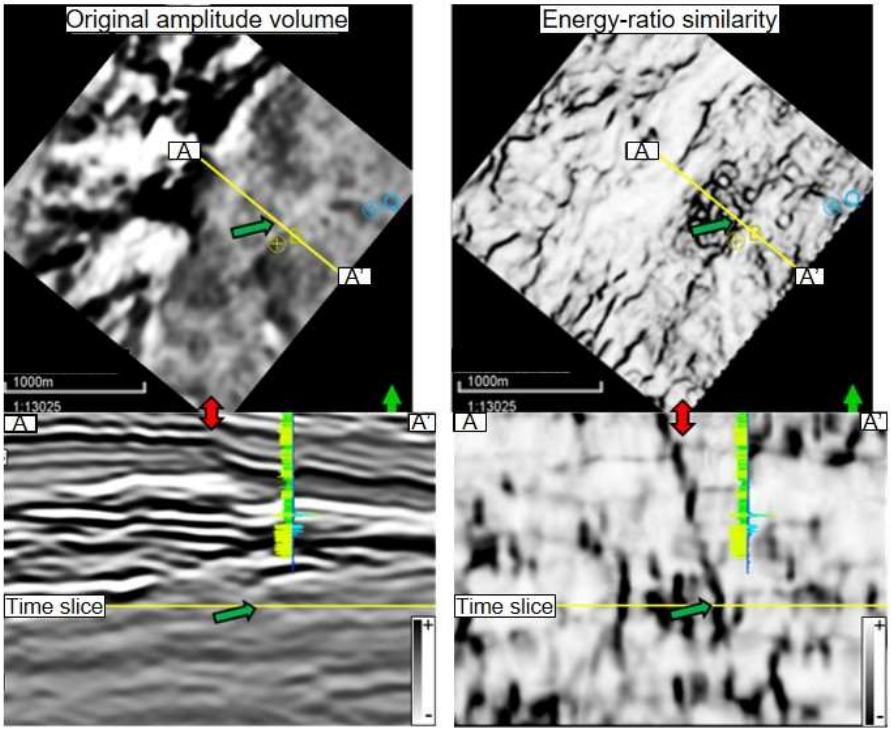


Figure 4. 1 - Comparison between a time slice and vertical section using the original amplitude volume (left) and the energy-ratio attribute (right). The fault is easily observed with the energy-ratio attribute and is also possible to interpret with more confidence close to the base of the depositional system (green arrow). The vertical section is displaying 400ms of time.

Subtle faults can be better delineated using structure curvature, with short wavelengths (especially for the reservoir interval). An interesting aspect of the most-positive and most-negative curvature components is the common association with upthrow and downthrown blocs within fault zones (Figure 2.4).

Based on the results described within Chapter 2, I noticed the advantages of having a multi-attribute approach. One additional example can be seen in Figure 4.2 that shows how curvature can complement coherency using a horizon slice visualization. The yellow arrows point to regions

where the discontinuities can be extended laterally using a combination of both attributes. Mai et al. (2009) also demonstrated improvements for fault identification combining coherence and curvature attributes.

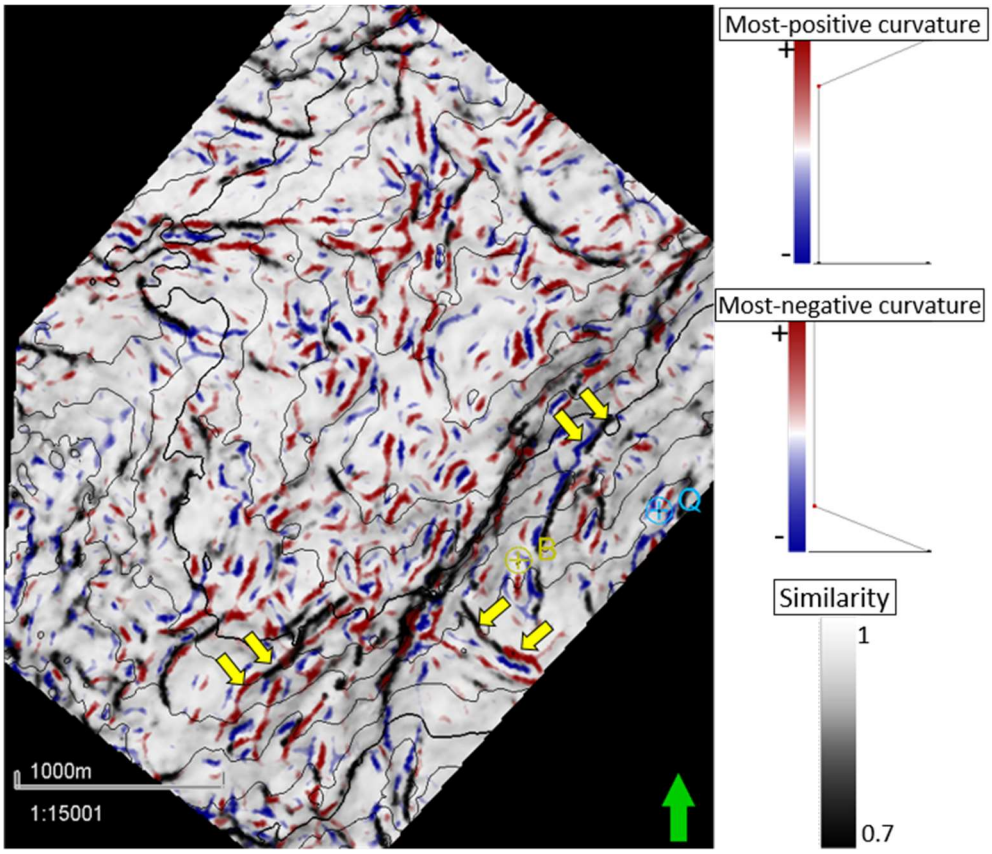


Figure 4. 2 – Curvature attributes (most-positive and most-negative components) and energy-ratio similarity attribute computed at the top of the Cretaceous horizon. An eight ms window was used to obtain the values similarity and curvature values. The energy-ratio attribute defined the major discontinuities. The lateral extension of some discontinuities can be complemented using curvature computed with short-wavelength (yellow arrows show the possible extension of the structures).

A continuous evaluation of the results is necessary to evaluate the geological meaning for the features described in different cubes. A comparison with the original amplitude volume is a good practice. Marfurt and Alvez (2015) reveal that many artifacts can affect the interpretation of seismic attributes.

► Is it better to use the entire amplitude spectrum or a specific frequency range?

Regarding the geometry and changes in fault dips, the broadband and multi-spectral volumes provided a better definition of the fault surfaces than specific filter ranges. Lower frequencies identify the structures partially, and the volumes composed only by higher frequencies (more than 50 Hz) are strongly affected by noise. Li and Lu (2014) describe improvements to delineate faults' computing coherence for specific frequency ranges. Chopra and Marfurt (2018) describe the advantages of multi-azimuthal coherence over individual azimuthal-focused coherence.

► What are the interpretational impacts of different azimuthal sectors?

A comparison between full-stack azimuth and individual azimuth sectors volumes shows less noise content in the first case. This relation between lower signal-to-noise ratio and azimuth-limited data was also described by Chopra and Marfurt (2007). Mueller et al. (2010) studied a carbonate field located in the Middle East and described the higher levels of noises associated with individual azimuth sectors.

Considering different azimuth sectors, Mueller et al. (2015) described improvements for fault recognition using sectors oriented parallel to the discontinuities. For Jubarte, individual

azimuth sectors helped to improve the identification of faults in cases when the seismic acquisition was positioned perpendicular to the fault direction. Chopra and Marfurt (2007) mention the importance of using data azimuths positioned perpendicular and parallel to the discontinuity. Each azimuth sector will have some pros and cons.

► Do principal component analysis (PCA) and self-organizing maps (SOM) provide additional insights into the traditional seismic interpretation methods?

PCA was used to reduce the number of attributes to the volumes with higher variability, and SOM was applied to recognize specific clusters within faults and fractures. The application of PCA and SOM provided results more aligned with qualitative interpretations for geometric attributes. One possible explanation for the limited improvement for fault identification using the instantaneous attributes and unsupervised clustering is the cyclical characteristics of some attributes, as described in Zhao et al. (2015).

As seen with Figures 2.10 and Figure 3.6, unsupervised clustering techniques can indicate faults. It is necessary to carefully evaluate the results using time slices and vertical sections. The same cluster that reveals a fault can indicate other features (stratigraphic termination, noise) in another part of the study area. Hussein et al. (2021) used PCA and SOM to analyze and classify anomalies related to subtle faults within the Maui region (Taranaki Basin). These authors demonstrate improvements to the identification of en echelon faults in the northern part of the field.

In the study area, faults can be better defined close to the top of the Cretaceous and top of Maastrichtian turbidite sandstones. In those zones, faults are more vertical, and the impedance contrasts more visible than the interval below composed of shale. The main discontinuities recognized in the study area are faults oriented to NE-SW. Although it contains seismic noise, the use of azimuthal volumes oriented perpendicular to the structure complements the lateral continuity of the discontinuity.

While this thesis demonstrated the importance of data conditioning, attributes computation, and unsupervised machine learning in the Jubarte Field, these methods are transferrable to other regions. A multi-attribute investigation complemented with data conditioning, and machine learning techniques provided a better description of the discontinuities than analysis using only the original amplitude volumes.

One possibility is to apply these techniques to evaluate mature fields. In other areas, where the impact of faults and fractures is critical, the discontinuities delineation can, for example, increase the oil recovery in reservoirs controlled by structural traps. These techniques are not only limited to structural enhancement for reservoir purposes but could also be applied to the recognition of discontinuities in exploratory areas.

The characterization of faults and fractures can also add insights into the understanding of basin-scale migration routes. For this purpose, curvature attributes computed with long-wavelength may provide better results highlighting first-order features. As we saw studying the Jubarte Field, short-wavelength provided more detailed features.

FUTURE WORK

I did many tests using full-stack volumes (Monitor-01 and Monitor-02) and different azimuthal data. Another possibility is to explore the computation of the attributes for each partial stack (near, mid, far, and ultra-far) available in the Jubarte PRM project. Furthermore, this study was based on PP-wave volumes due to the higher frequency content, but future work based on PS-wave cube can add more insights into the structural interpretation because it can provide insightful details about anisotropic media.

It will be appropriate to correlate the discontinuities recognized within this research with the field's production data to see if different reservoir compartments can be individualized. It will also be interesting to consider the mechanical responses of sandstones and shale because these properties will help understand the seismic signature of some faults. Analysis of different rock competence can complement the observations. This study could also be improved by combining the attribute responses with image logs.

Additional analysis can define the relation between the spectral broadening applied during the processing and the noise below the reservoir. It can be helpful to analyze the impact of the different Q factors applied. Finally, more investigations using horizon slices can be helpful to investigate features of interest.

REFERENCES

Barnes, A. E., 2016, Complex seismic trace analysis, *in*: Handbook of poststack seismic attributes, SEG, 45-74.

Chopra, S., and K. J. Marfurt, 2007, Seismic attributes for prospect identification and reservoir characterization: SEG.

Chopra, S., and K. J. Marfurt, 2018, Coherence attribute applications on seismic data in various guises: Unconventional Resources Technology Conference – URTeC:2886034, 1-9.

Ha, T.N., K.J. Marfurt, B.C. Wallet, and B. Hutchinson, 2019, Pitfalls and implementation of data conditioning, attribute analysis, and self-organizing maps to 2D data: application to the Exmouth Plateau, North Carnarvon Basin, Australia: *Interpretation*, **7**, no.3, SG23-42.

Hussein, M., R. Stewart, and J. Wu, 2021, Which seismic attributes are best for subtle fault detection?: *Interpretation*, **9**, 2, 1-21.

Li, F., and W. Lu, 2014, Coherence attribute at different spectral scales: *Interpretation*, **2**, no, 1, 1-8.

Libak, A., B. Alaei, and A. Torabi, 2017, Fault visualization and identification in fault seismic attribute volumes: implications for fault geometric characterization: *Interpretation*, **5**, 2, B1-B16.

Lyu, B., Qi, J., F. Li, Y. Hu., T. Zhao, S. Verma, and K. J. Marfurt, 2020, Multispectral coherence: Which decomposition should we use?: *Interpretation*, **8**, no. 1, T115-T129.

Mai, H. T., K. J. Marfurt, and S. Chavez-Perez, 2009, Coherence and volumetric curvatures and their spatial relationship to faults and folds, an example from Chicontepec basin, Mexico: SEG International Exposition and Annual Meeting, Expanded Abstract, 1063-1067.

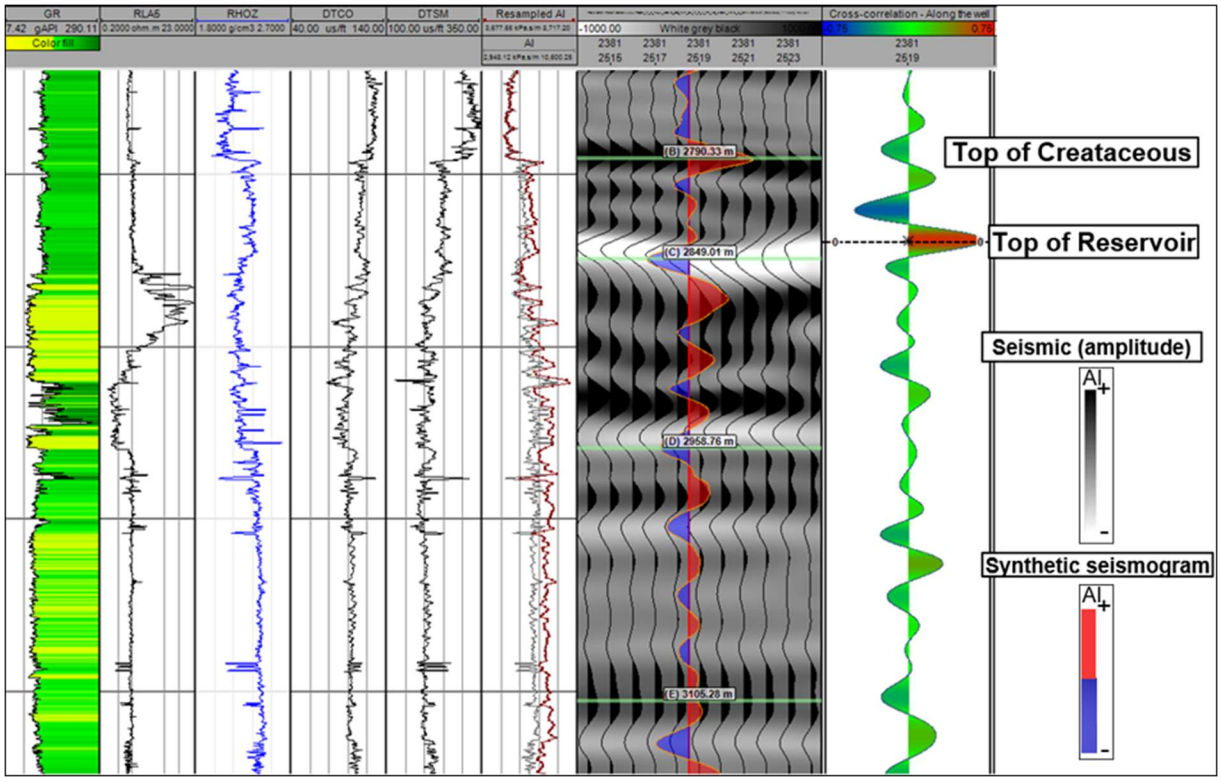
Marfurt, K. J., and T. M. Alves, 2015, Pitfalls and limitations in seismic attribute interpretation of tectonic features: *Interpretation*, **3**, no.1, A5-A15.

Mueller, K. W., M. S. Al Nahhas, W. L. Soroka, M. al Baloushi, R. Sinno, R. D. Martinez, W. Hussein, and P. LeCocq, 2010, Azimuthal seismic pilot for fault and fracture dectection – an Abu Dhabi, U.A.E. case study: Adu Dhabi International Petroleum Exhibition & Conference, SPE 137338.

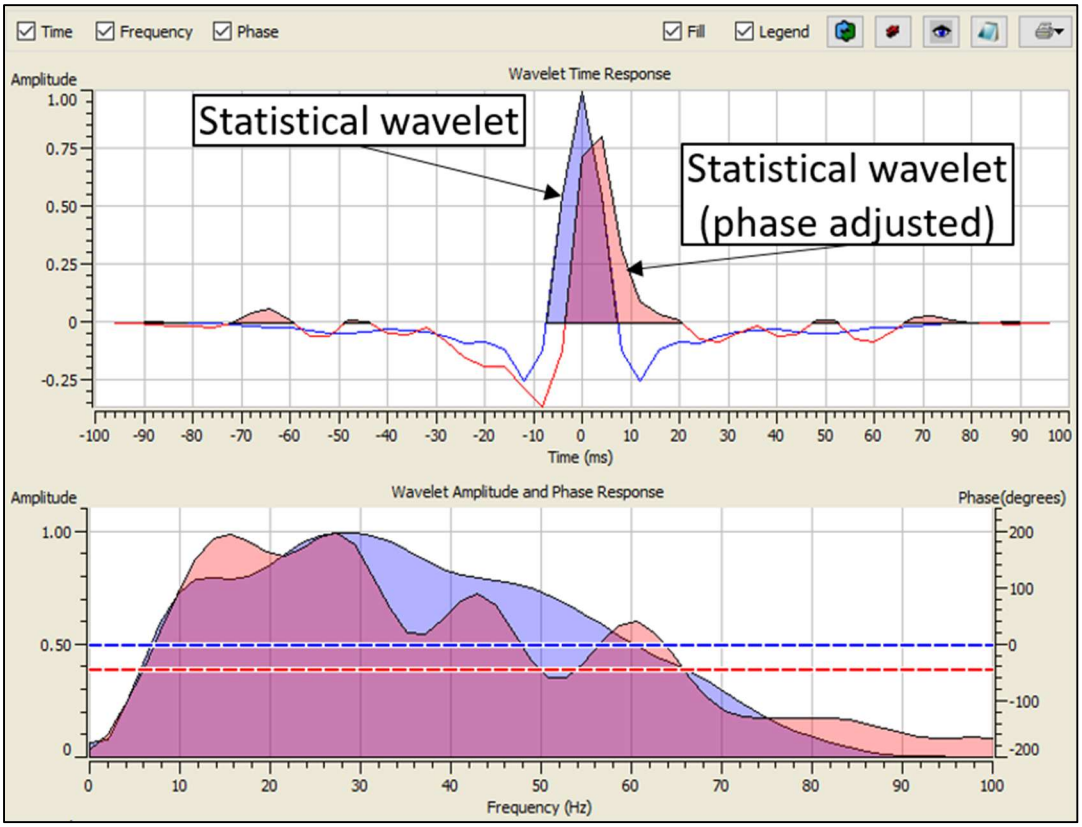
Zhao, T., V. Jayaram, A. Roy, and K. J. Marfurt, 2015, A comparison of classification techniques for seismic facies recognition: *Interpretation*, **3**, no. 4, SAE29-SAE58.

APPENDIX A – Example of well tie

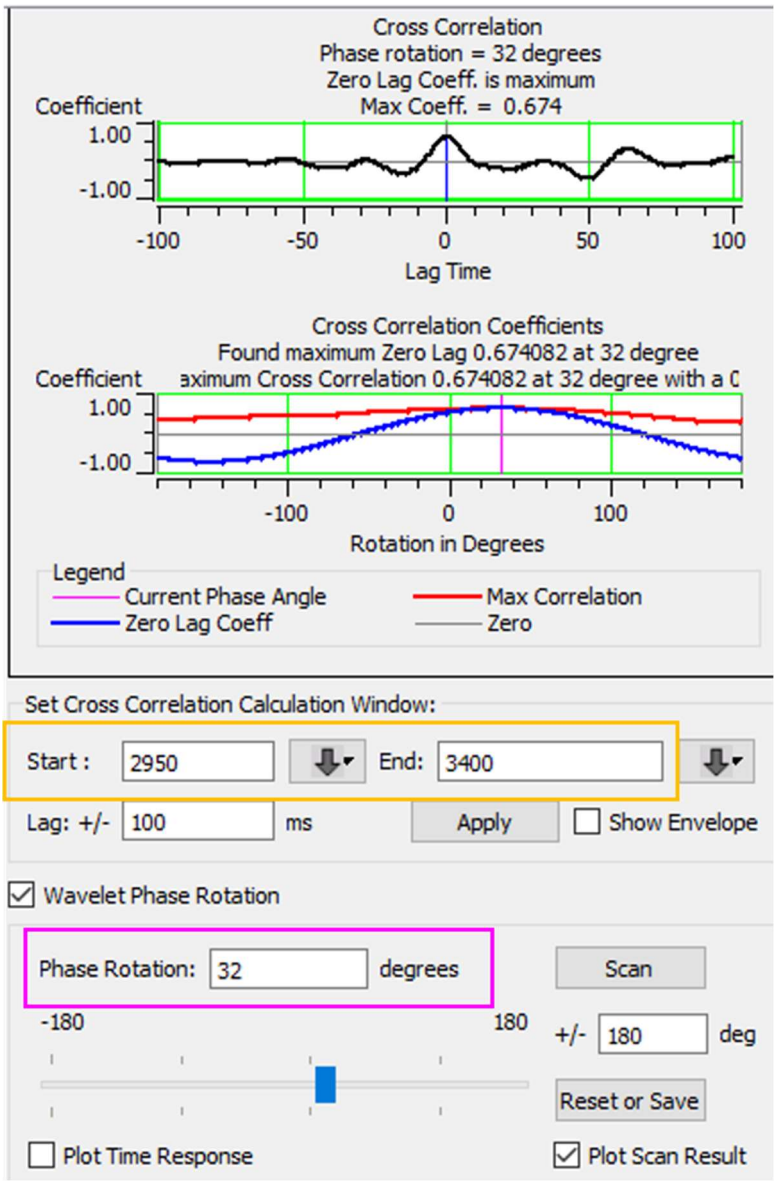
The top of the Cretaceous represents a regional surface used to initiate the correlations. To generate this seismogram was adopted a statistical wavelet (estimated from 2.5 – 3.4 s).



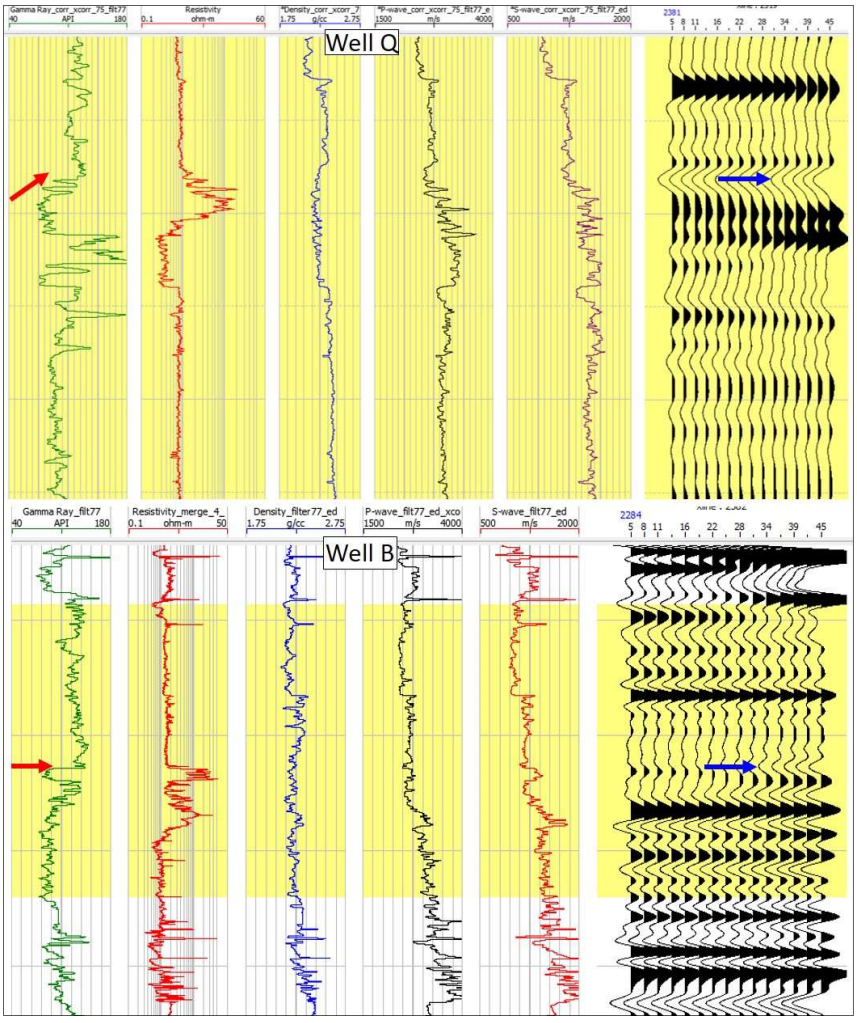
Comparison between the statistical wavelet and the same wavelet with phase adjusted based on logs from Well B. Area used to generate the wavelets is limited in time (1 second window) and area (inline and crossline numbers 2350-2530). Wavelet length: 200ms.



GUI used to analyze the phase rotation to be applied within the synthetic (pink box). The interval indicated with the orange box corresponds to the area used to scan the phase rotation value.



Different responses for the top of the Maastrichtian reservoir. Well Q has an upward thinning that interferes in seismic response. The vertical section is displaying 250ms of time. A weak gradient is observed within this setting. If we compare the synthetic seismogram from Well B calculated with the same parameter (the three-term Aki-Richards equation, incidence angles from 5 to 45 degrees, and the same wavelet), we can see a different response. Well B displays an abrupt change in the properties close to the top of the reservoir that results in a more negative gradient. S-wave velocity also reflects these different transitions from the units above and the reservoir. The vertical section is displaying 400ms of time.



APPENDIX B – Reflectivity analysis using well logs

Implementation of Fatti et al. (1994) equation in Python to investigate the impact of different density and velocity values.

```
# Application of Fatti et al.(1994) equation to estimate reflectivity in different scenarios
# Parameters:
# R = P-wave reflection coefficient
# Vp = P-wave velocity
# Vw = S-wave velocity
# rho = density
# I = rho * Vp (P-impedance)
# J = rho * Vw (S-impedance)
# Obs: the numbers 1 and 2 associate with Vp, Vw and rho correspond to upper and lower layers respectively

# Importing the libraries:
import math
import numpy as np
from fractions import Fraction
from matplotlib import pyplot as plt

#Creating a function to do the basic maths:
def fatti(Vp1,Vp2,Vw1,Vw2,rho1,rho2):
    Vp = (Vp1 + Vp2)/2
    deltaVp = Vp2-Vp1
    W = (Vw1 + Vw2)/2
    deltaW = Vw2-Vw1
    rho = (rho1+rho2)/2
    deltarho = rho2-rho1
    I1 = rho1 * Vp1
    I2 = rho2 * Vp2
    J1 = rho1 * Vw1
    J2 = rho2 * Vw2
    deltaI = I2 - I1
    deltaJ = J2 - J1
    I = (I1 + I2)/2
    J = (J1 + J2)/2

# The equation can be separated in three terms (R1, R2 and R3). Let's calculate them individualy:
    R1 = []
    for i in range (35):
        Ri = 0.5 * (deltaI/I) * (1 + (np.tan(np.deg2rad(i)**2)))
        R1.append(Ri)
    R2 = []
    for j in range (35):
        Rj = 4 * ((W/Vp)**2)*(deltaJ/J)*((np.sin(np.deg2rad(j))**2))
        R2.append(Rj)
    R3 = []
    for k in range (35):
        Rk = (0.5*(deltarho/rho)*(np.tan(np.deg2rad(k)**2)))-2*((W/Vp)**2)*(deltarho/rho)*(np.sin(np.deg2rad(k))**2)
        R3.append(Rk)

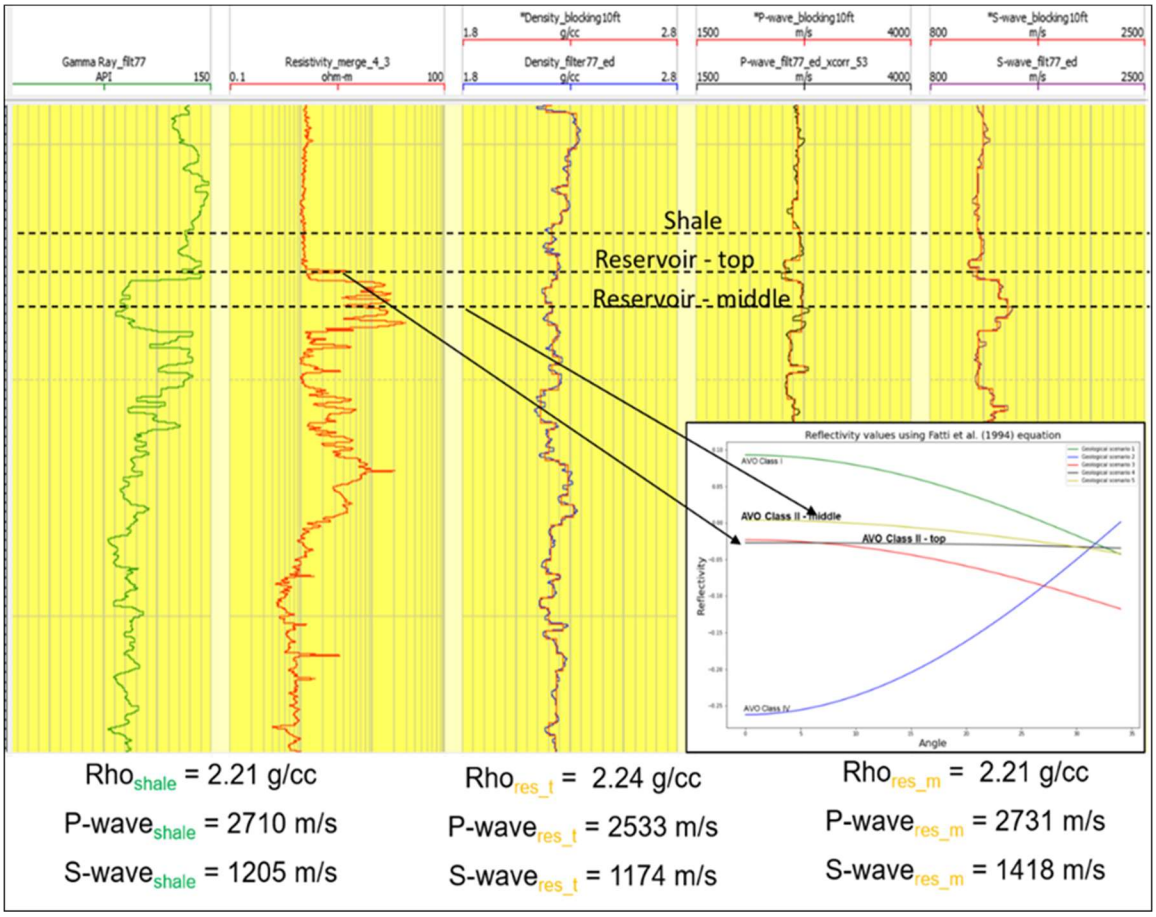
#Combination of the three terms to have the final reflectivity (R) for all angles
#R = R1 - R2 - R3
    R = []
    zip_object = zip(R1, R2, R3)
    for R1_i, R2_j, R3_k in zip_object:
        R.append(R1_i-R2_j-R3_k)
    return R

#Set parameters here
Vp1_list = [3095,3750,2645,2710,2710]
Vp2_list = [4050,3000,2780,2533,2731]
Vw1_list = [1515,2500,1170,1205,1205]
Vw2_list = [2525,1200,1665,1174,1418]
rho1_list = [2.40,2.6,2.29,2.21,2.21]
rho2_list = [2.21,1.9,2.08,2.24,2.21]
color_list = ["g","b","r","m","y"]

fig, ax = plt.subplots(figsize=(15,10))

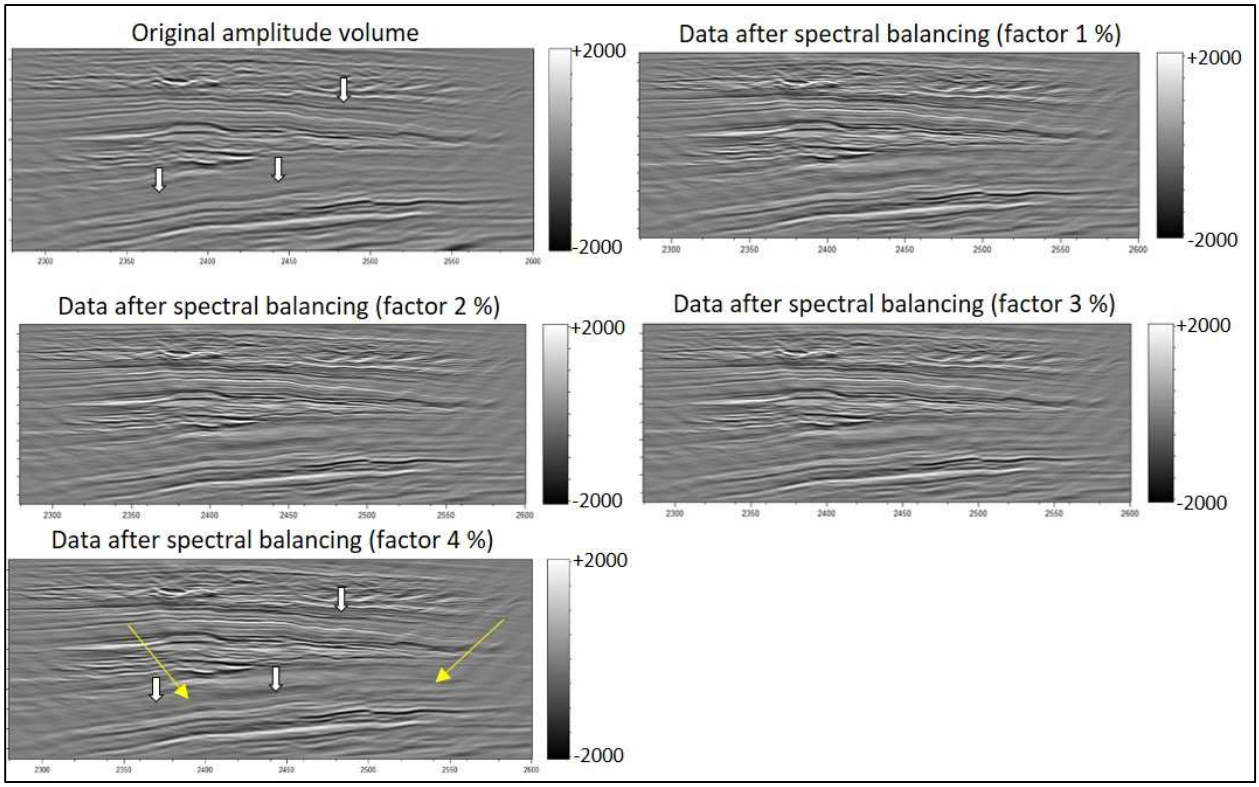
for counter in range(0,5):
    R=fatti(Vp1_list[counter],Vp2_list[counter], Vw1_list[counter], Vw2_list[counter], rho1_list[counter], rho2_list[counter])
    ax.plot(R, c = color_list[counter], label="Geological scenario "+str(counter+1)+"")
plt.title("Reflectivity values using Fatti et al. (1994) equation", fontsize=20)
plt.legend()
plt.xlabel('Angle', fontsize=20)
plt.ylabel('Reflectivity', fontsize=20)
plt.show()
```

Extraction of density, P and S velocities to evaluate the variation in the amplitude with angle using tree-terms Fatti et al. (1994) equation. This larger window shows the properties estimated for shale and reservoir (in two regions) in Well R. The minor figure displays a comparison of the reflectivity from 0 to 35 degrees calculated (black and yellow curves) compared to scenarios described in Chopra and Castagna (2014).



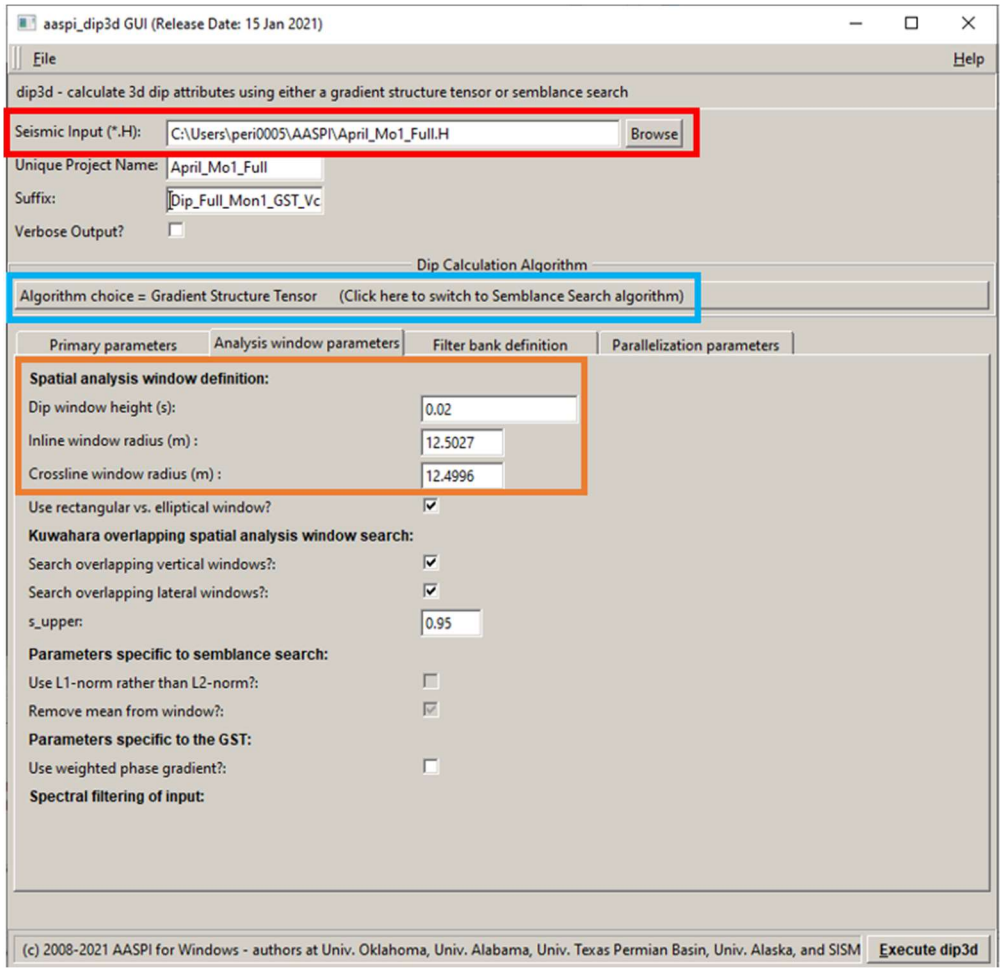
APPENDIX C – Comparison of different spectral balancing factors

Comparison between the original amplitude volume and the same vertical section after applying different spectral balancing factors (e.g., 1, 2, 3, and 4%). White arrows demonstrate points of improvement for the identification of small reflectors. The selected factor was 0.5%.

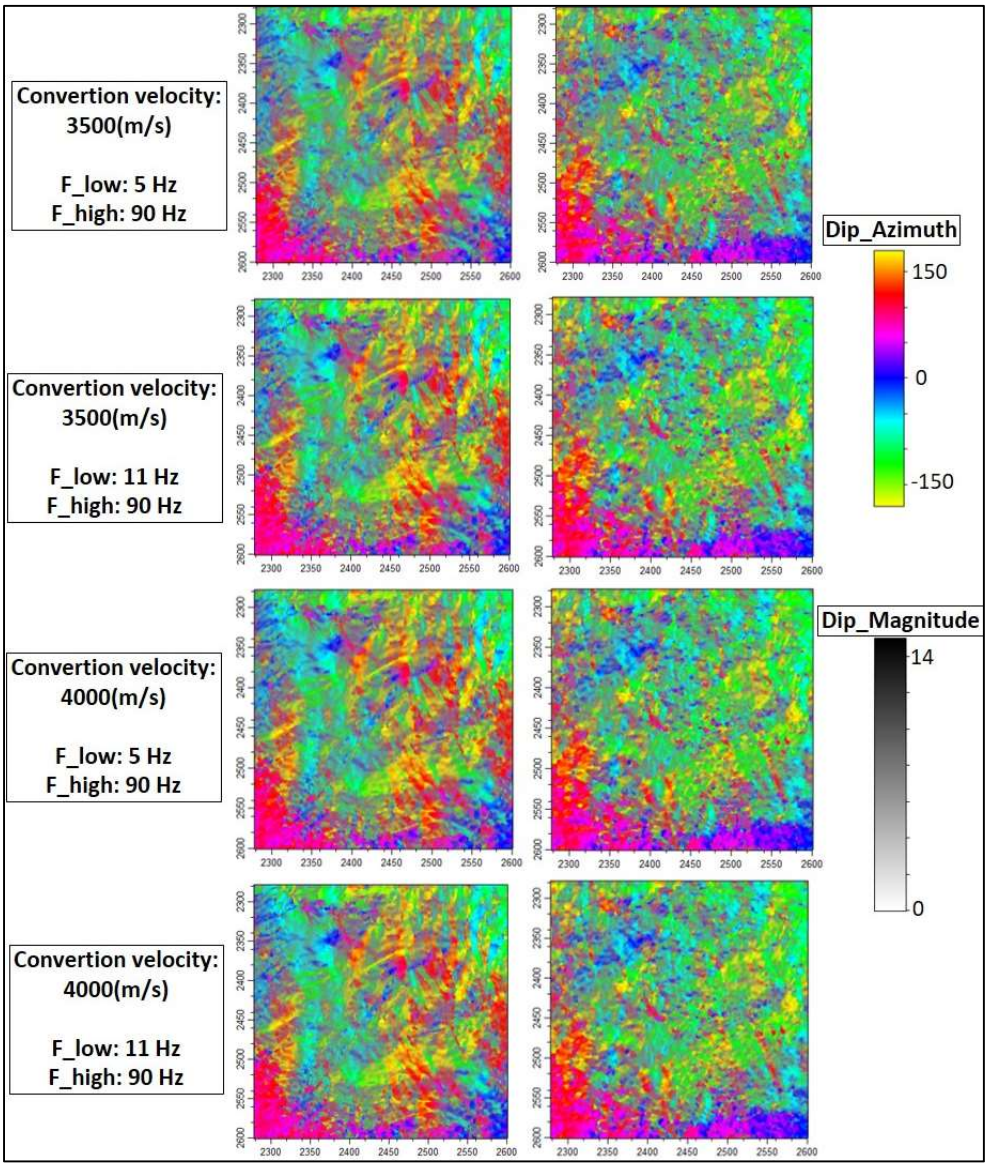


APPENDIX D – Computation of dip attribute and the results for different parameters

Example of the “Analysis window parameters” tab within the main Dip GUI in AASPI. The red box points to the field where the input is selected, and the blue box indicates the type of algorithm selected. I used the Gradient Structure Tensor. Also, the orange box includes essential parameters, such as the Dip window height (5 * 0.004 s = 0.02) and the inline and crossline window radius that correspond to the processing grid (12,5 x 12,5 m). As highlighted in AASPI documentation, using larger windows will result in a smoother dip estimation. A rectangular window was applied.

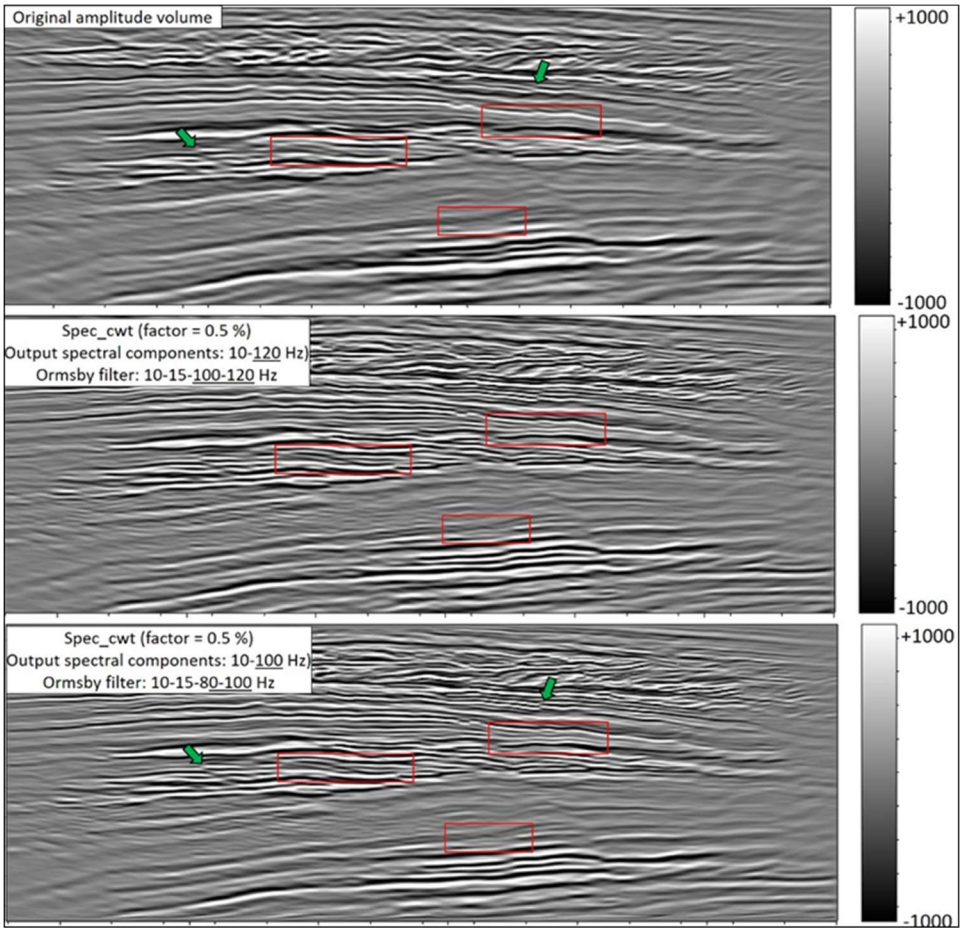


Comparison between different estimation of dip volumes. The parameters compared were the conversion velocity (3500 m/s vs. 4000 m/s), different lower frequencies values (5, 7, 9, 10, and 11 Hz), and higher frequencies (80 and 100 Hz). The comparison shows two time slices that correspond to the upper and lower parts of the reservoir. Lower conversion velocity (3500 m/s) resulted in slightly more smooth images.



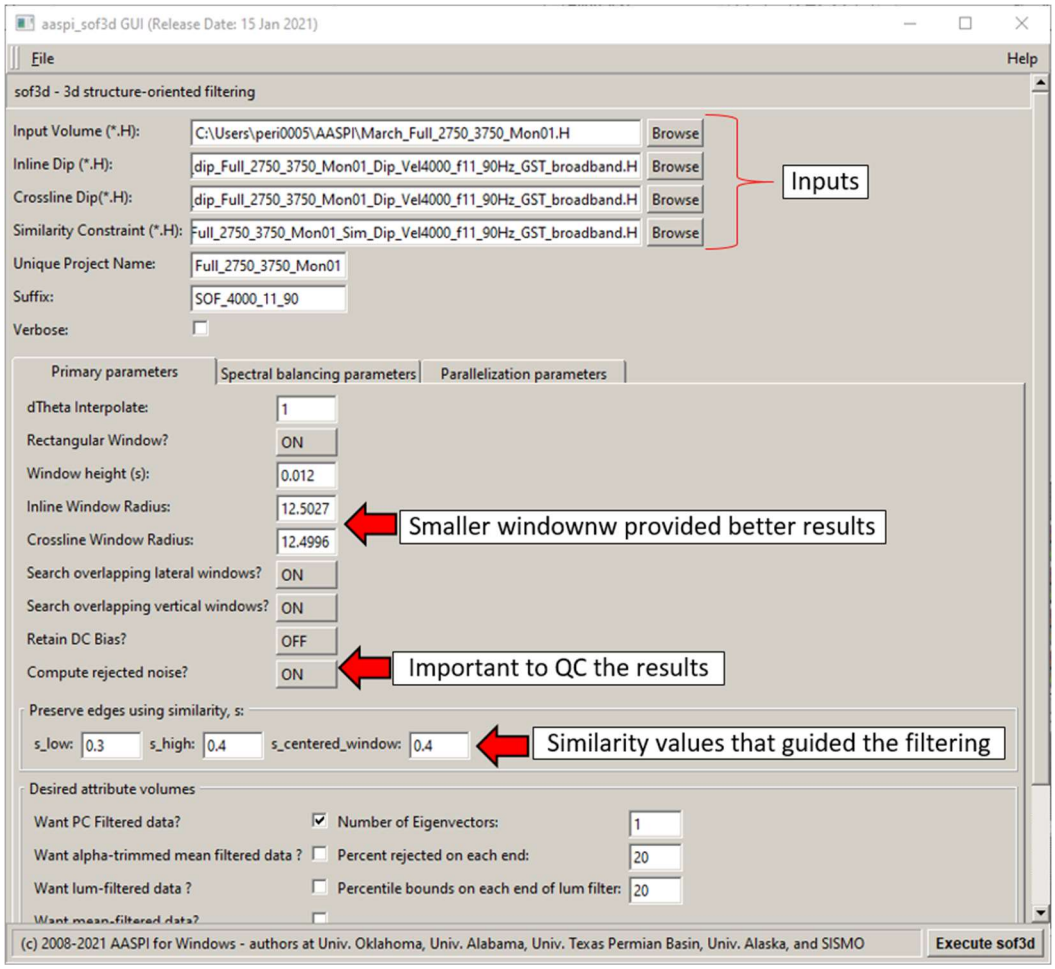
APPENDIX E – Comparison between a vertical section before and after spectral balancing and application of Ormsby Filter.

Two different limits for the higher frequencies for the Ormsby filter (f3=100 Hz and f4=120 Hz vs. f3 = 80 and f4 = 100 Hz). Green arrows show subtle faults more visible after the application of spectral balancing and Ormsby filter. Red boxes show areas with more reflectors more visible. The vertical section is displaying 900ms of time.

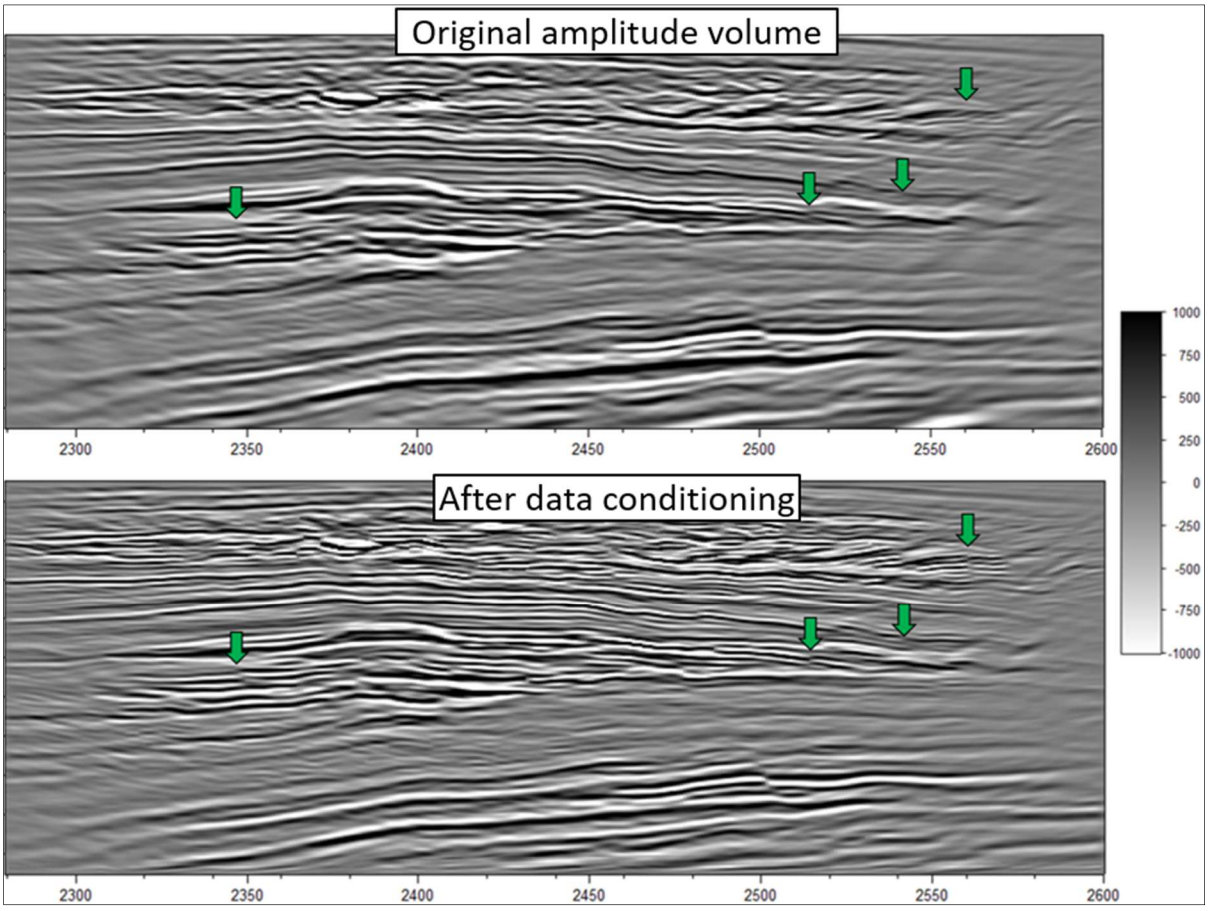


APPENDIX F – Examples of parameters used to compute the structure-oriented filtering (SOF) and an additional comparison

The main AASPI GUI used to generate the SOF volume. Inputs include the original seismic volume, dip components, and similarity constraint cube. Small windows radios provided better results (12.5 vs. 12.5 m). The use of the rejected noise cube helped to see what amplitudes were removed (QC analysis). After various tests, similarity values of 0.3 and 0.4 were considered references for preserving filtering processes.

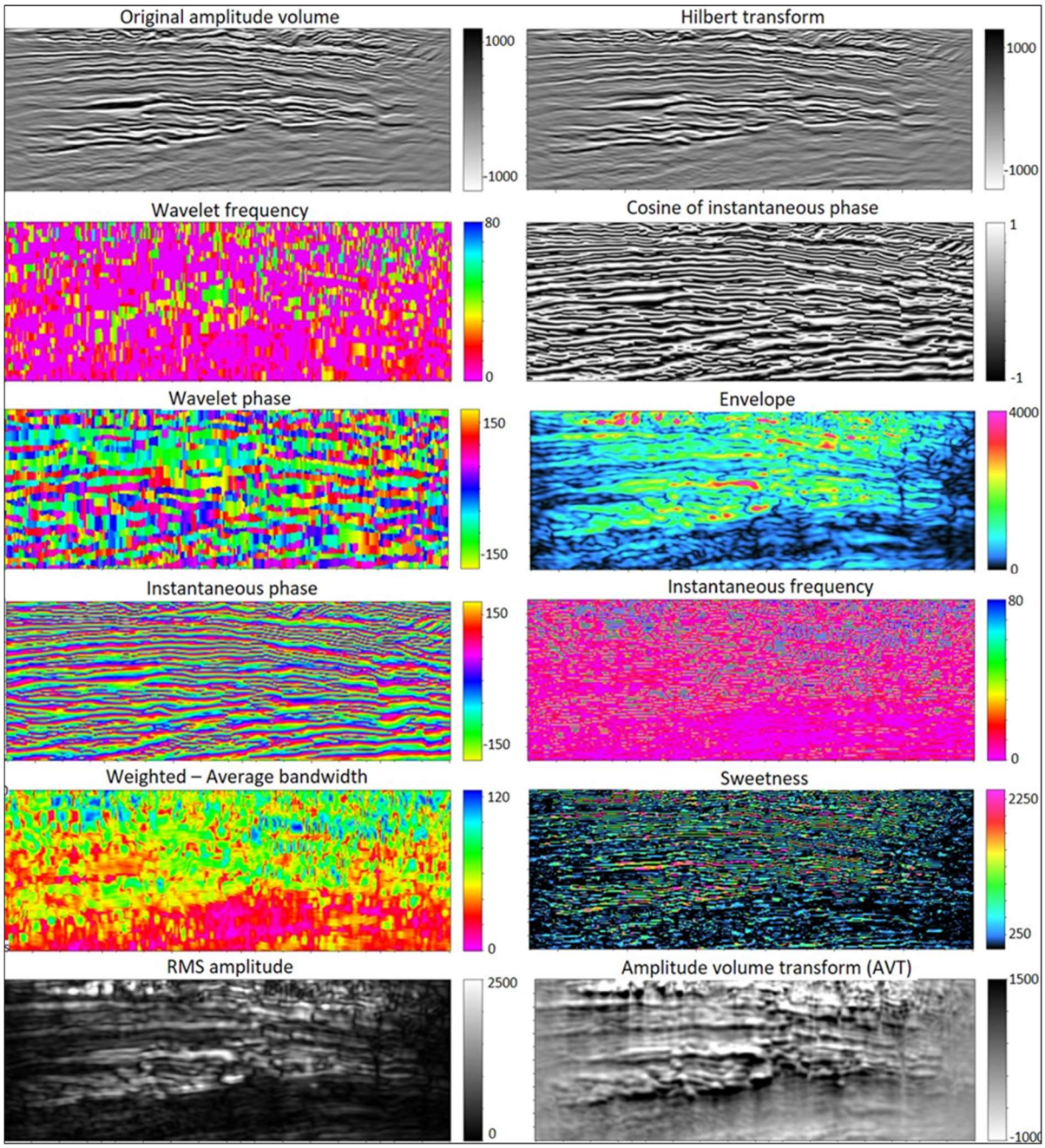


Comparison between the original amplitude volume (upper section) and the same vertical slice after data conditioning. The green arrows show discontinuities more visible after the application of the spectral balancing and structure-oriented filtering.



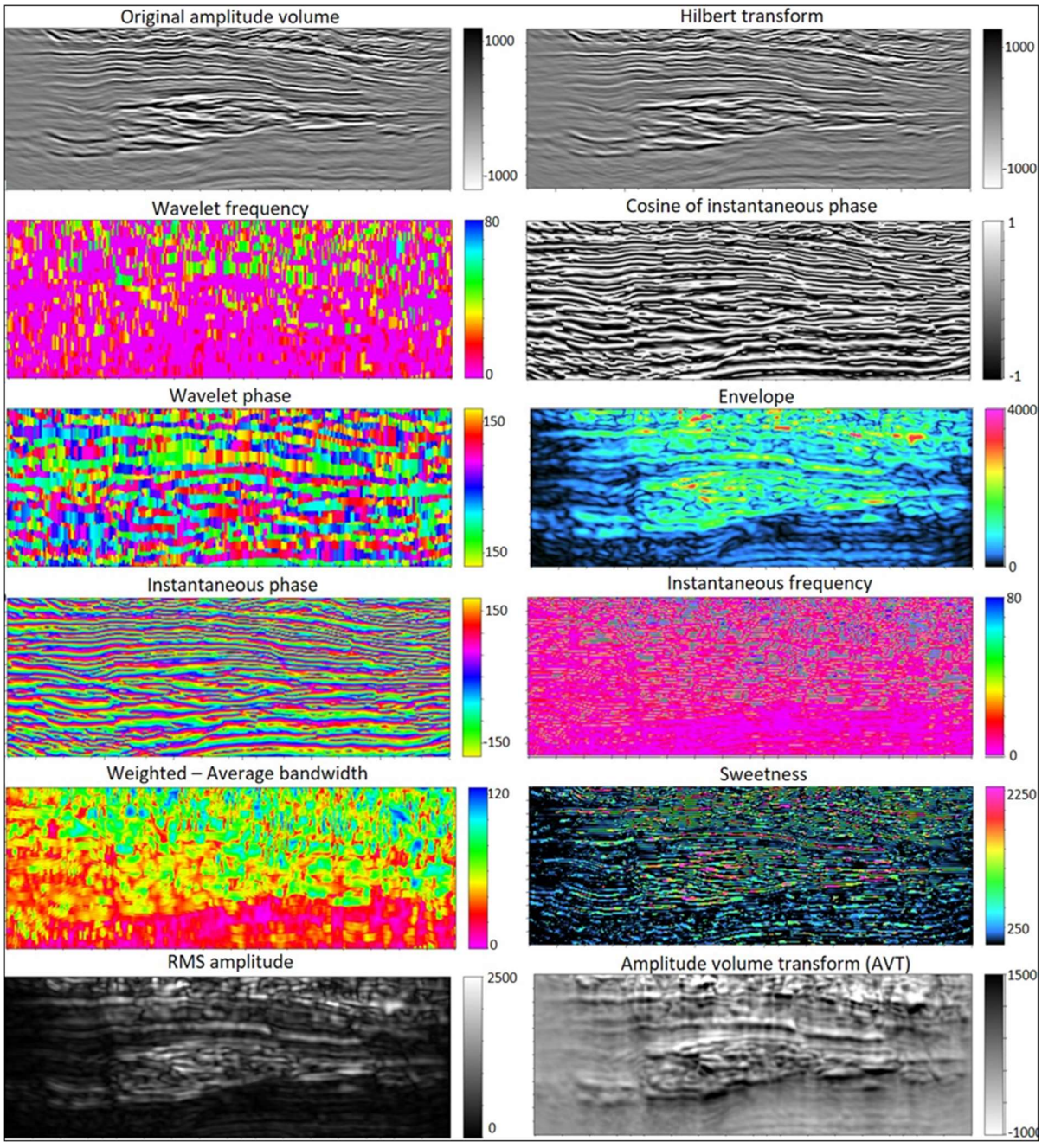
APPENDIX G– Comparison between different instantaneous attributes computed after data conditioning.

The vertical section is displaying 600ms of time.

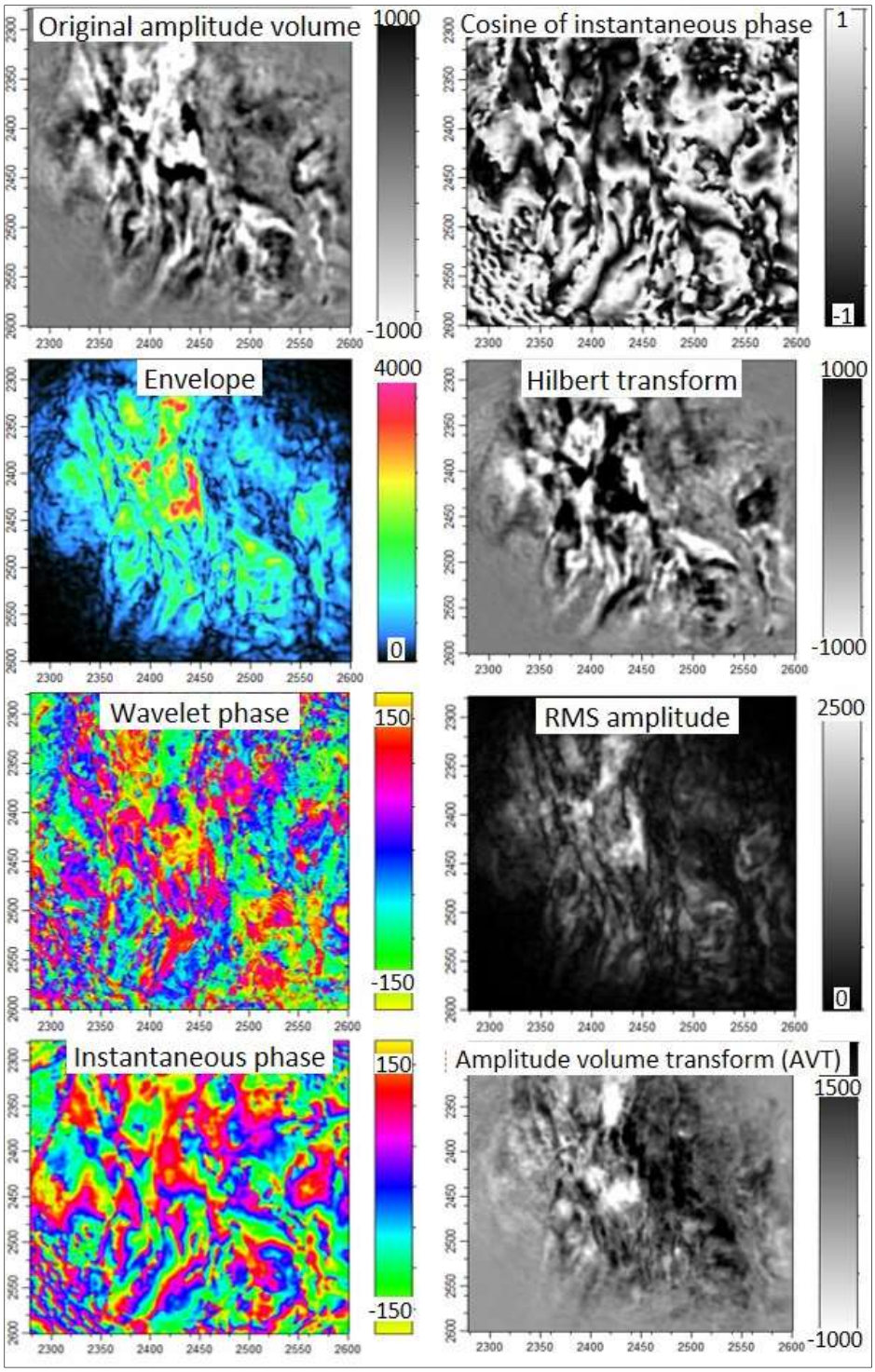


Comparison between different instantaneous attributes computed after data conditioning.

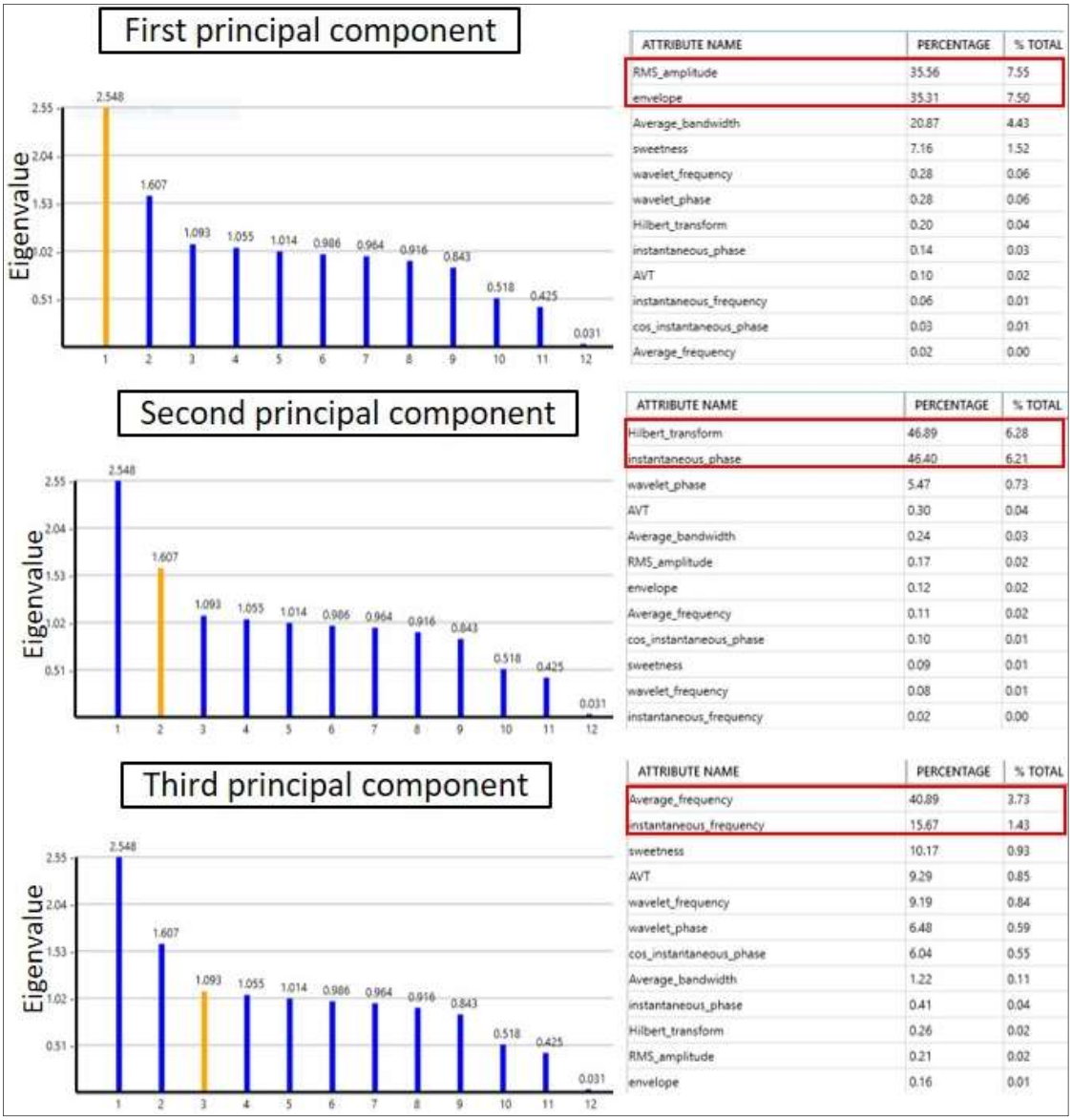
The vertical section is displaying 600ms of time.



Comparison between different instantaneous attributes computed after data conditioning.



APPENDIX H – PCA results for instantaneous attributes



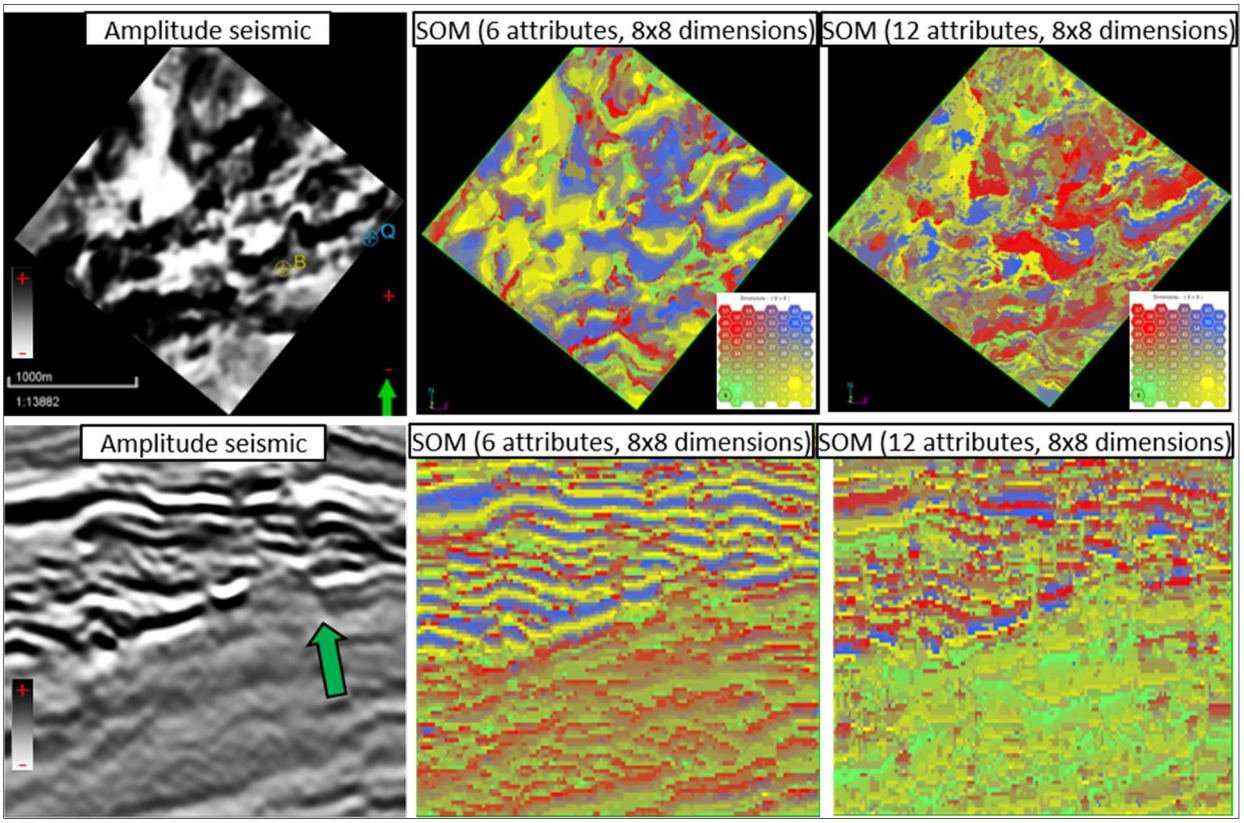
ATTRIBUTE NAME	PERCENTAGE	% TOTAL
RMS_amplitude	35.56	7.55
envelope	35.31	7.50
Average_bandwidth	20.87	4.43
sweetness	7.16	1.52
wavelet_frequency	0.28	0.06
wavelet_phase	0.28	0.06
Hilbert_transform	0.20	0.04
instantaneous_phase	0.14	0.03
AVT	0.10	0.02
instantaneous_frequency	0.06	0.01
cos_instantaneous_phase	0.03	0.01
Average_frequency	0.02	0.00

ATTRIBUTE NAME	PERCENTAGE	% TOTAL
Hilbert_transform	46.89	6.28
instantaneous_phase	46.40	6.21
wavelet_phase	5.47	0.73
AVT	0.30	0.04
Average_bandwidth	0.24	0.03
RMS_amplitude	0.17	0.02
envelope	0.12	0.02
Average_frequency	0.11	0.02
cos_instantaneous_phase	0.10	0.01
sweetness	0.09	0.01
wavelet_frequency	0.08	0.01
instantaneous_frequency	0.02	0.00

ATTRIBUTE NAME	PERCENTAGE	% TOTAL
Average_frequency	40.89	3.73
instantaneous_frequency	15.67	1.43
sweetness	10.17	0.93
AVT	9.29	0.85
wavelet_frequency	9.19	0.84
wavelet_phase	6.48	0.59
cos_instantaneous_phase	6.04	0.55
Average_bandwidth	1.22	0.11
instantaneous_phase	0.41	0.04
Hilbert_transform	0.26	0.02
RMS_amplitude	0.21	0.02
envelope	0.16	0.01

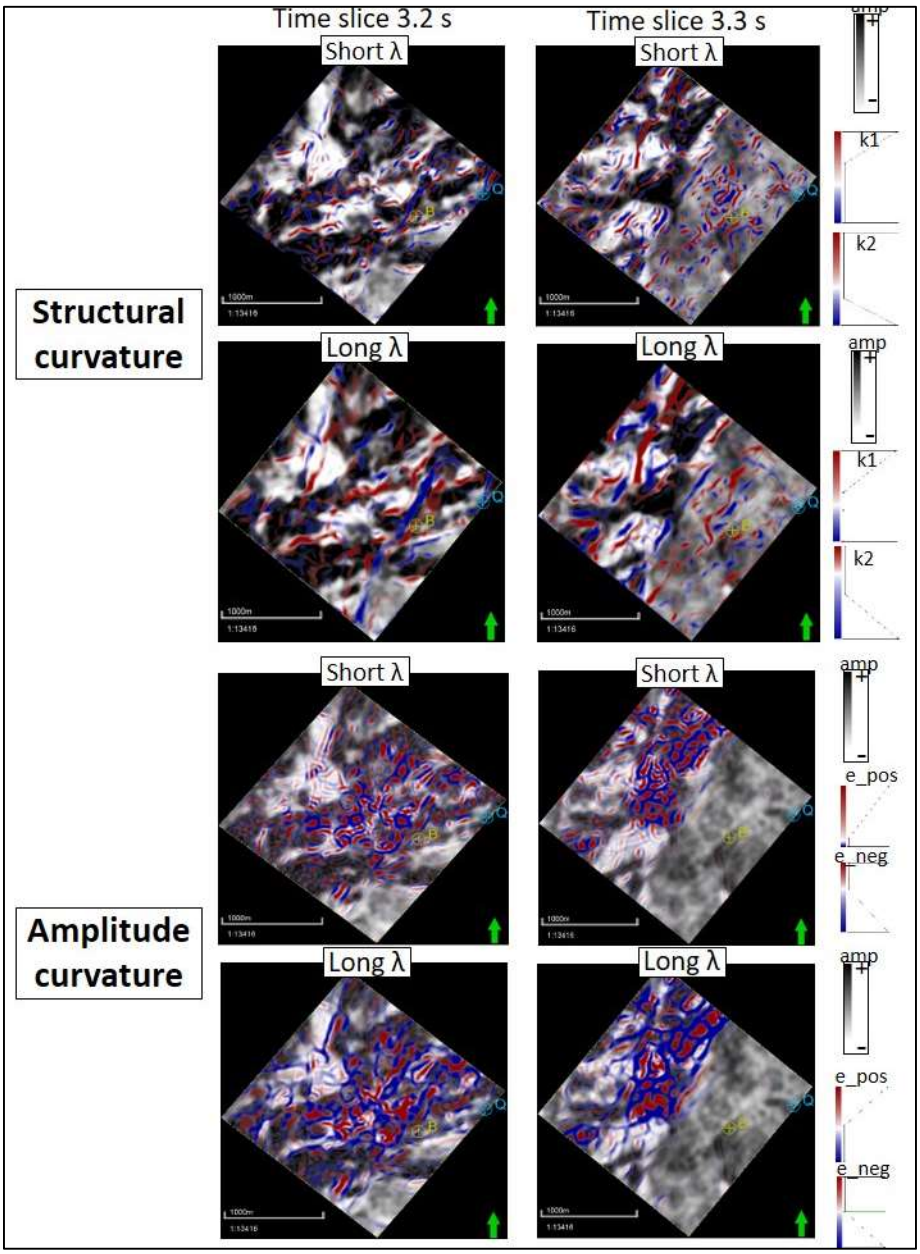
APPENDIX I - SOM results for instantaneous attributes

Comparison between SOM results using different instantaneous attributes (six attributes highlighted in PCA vs. 12 attributes generated initially). The results were considered limited for structural purposes because no significant neuron clusters defined faults and fracture surfaces.



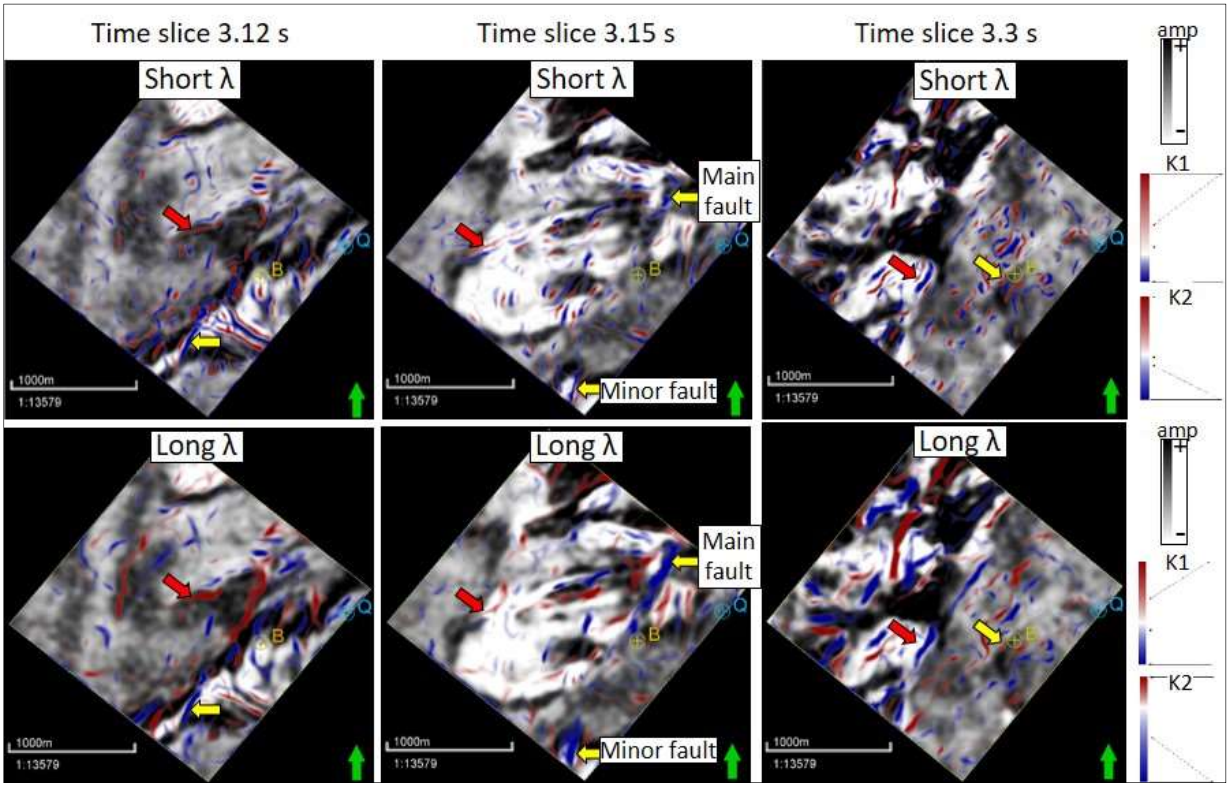
APPENDIX J – Comparison between different curvature algorithms and parameters

Comparison between structural and amplitude curvature methods, calculated with short and long operators.



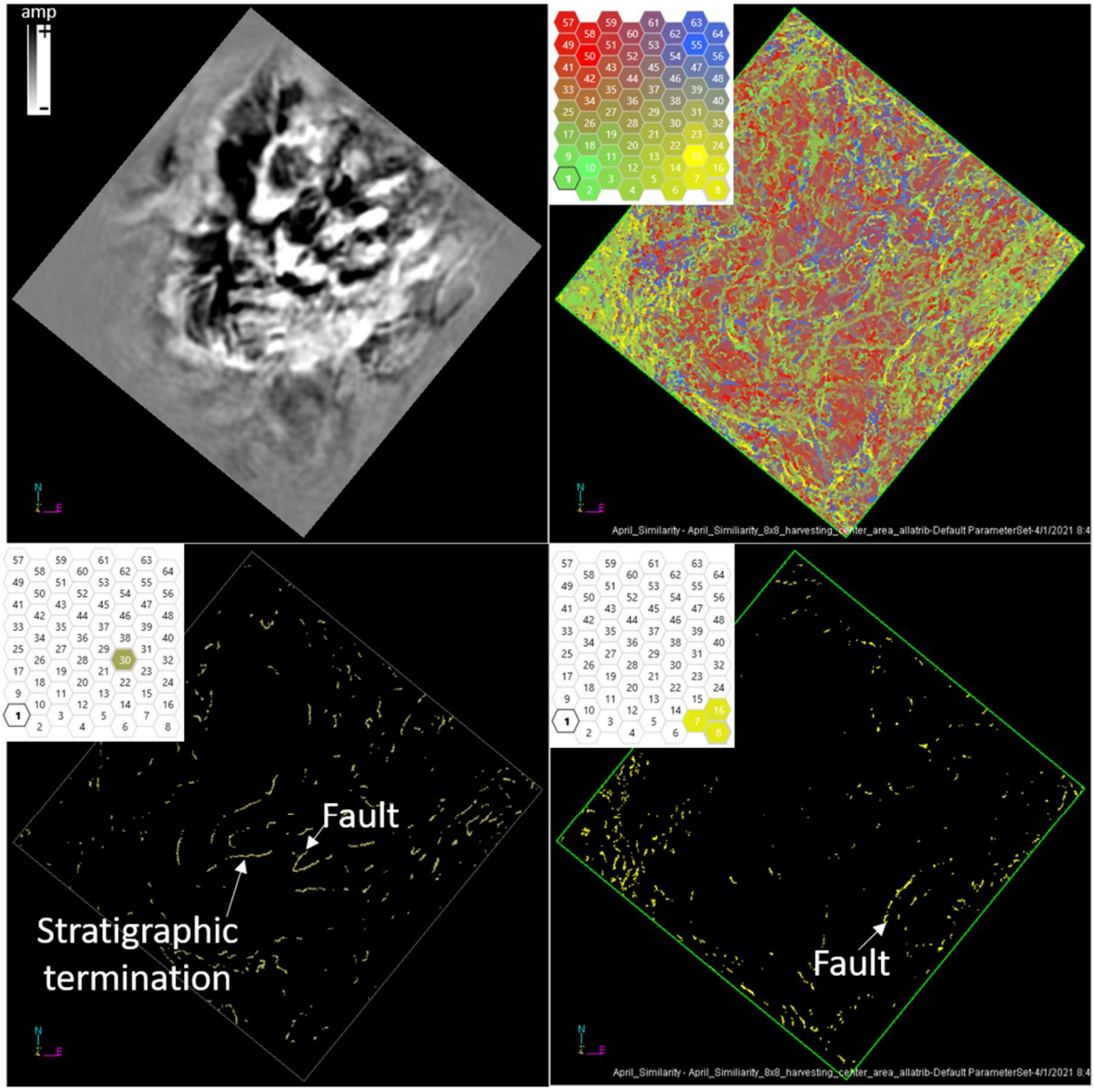
APPENDIX K – Comparison between short and long wavelengths operator

Comparison between short and long operators computed with structural curvature. In-context interpretation is essential because attributes will highlight stratigraphic terminations (red arrows) and structural elements (yellow arrows).

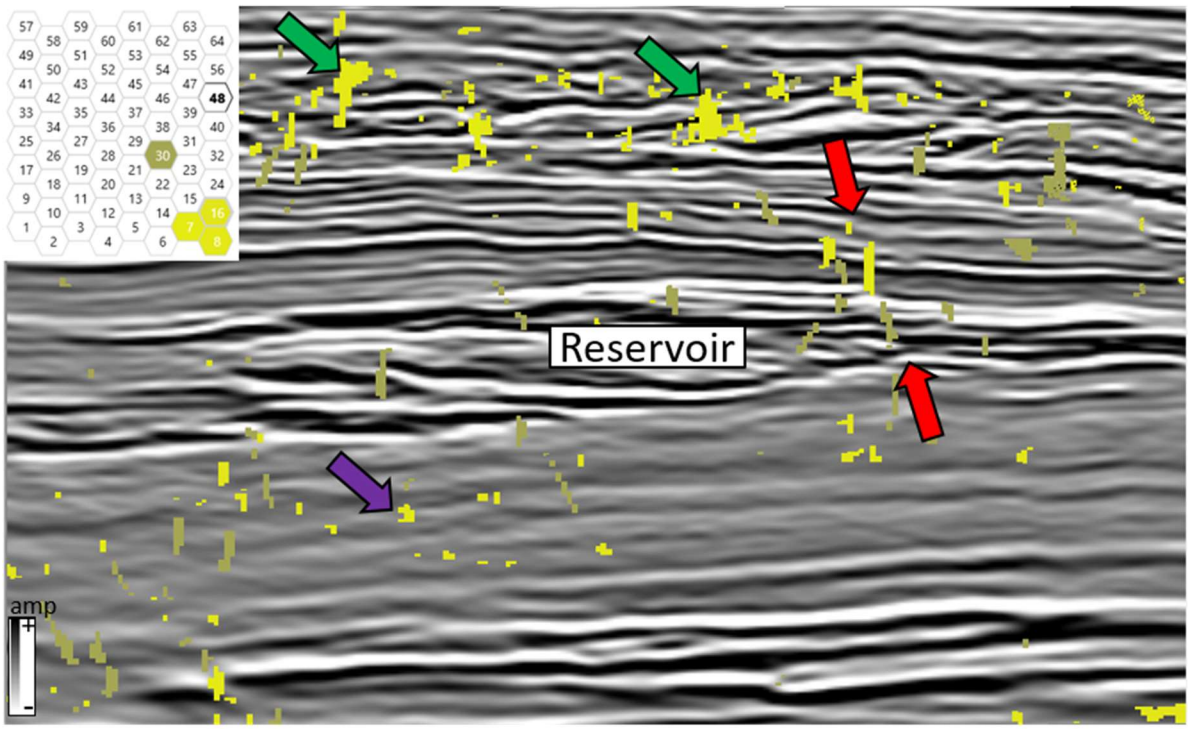


APPENDIX L - SOM results for instantaneous attributes

Comparison between the original amplitude volume (upper left) and SOM using 64 clusters (upper right) and specific neurons (lower part). Note the indication of anomalies associated with stratigraphic and faults can be recognized with some clusters. On the other hand, the same group of the cluster also reveal noise and other features.

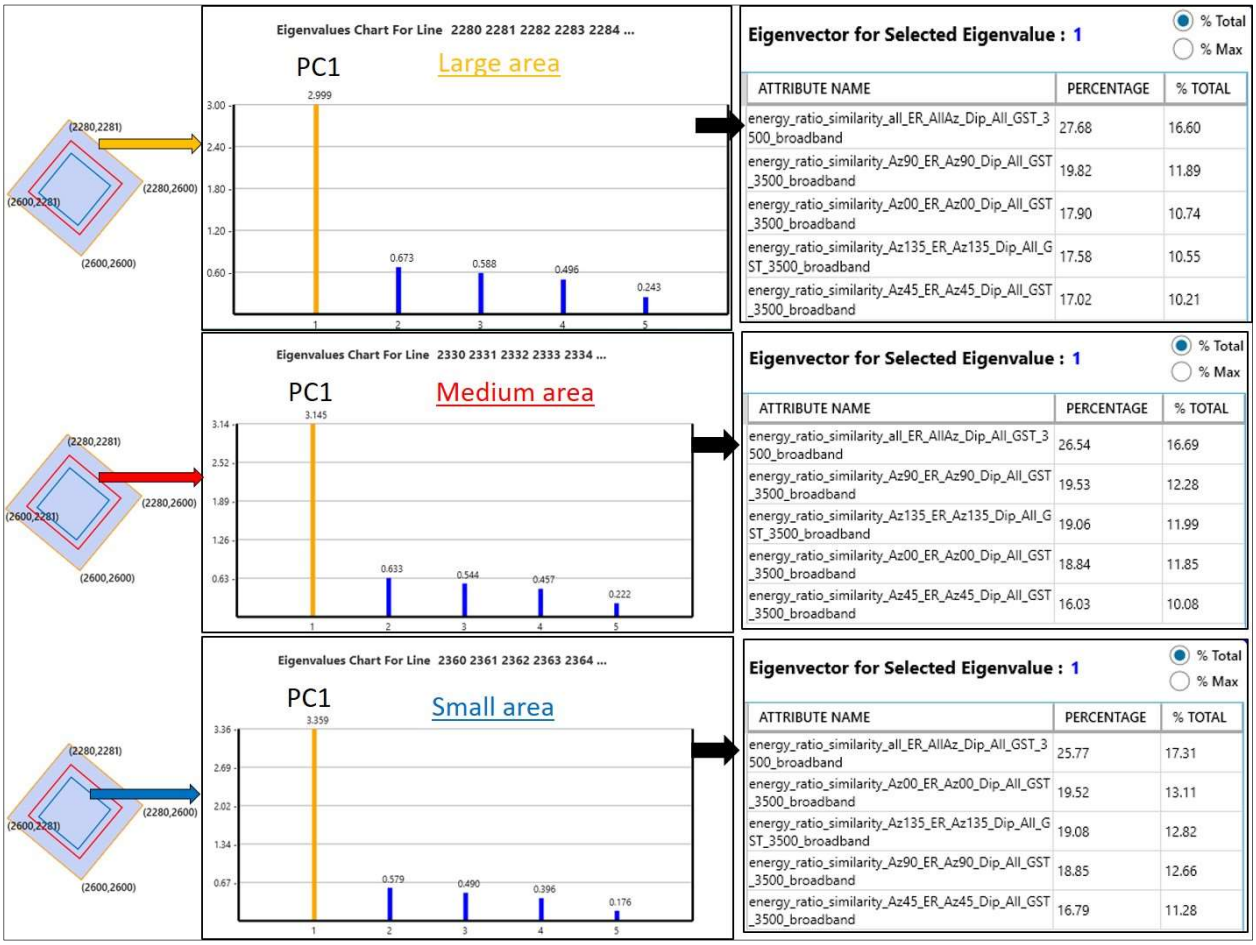


Corendered image of the original amplitude volume and four neurons. Note that for the reservoir interval, these clusters highlighted regions related to faults (red arrows), but for another section, they reveal chaotic deposits (green arrows) and noise (purple arrows).



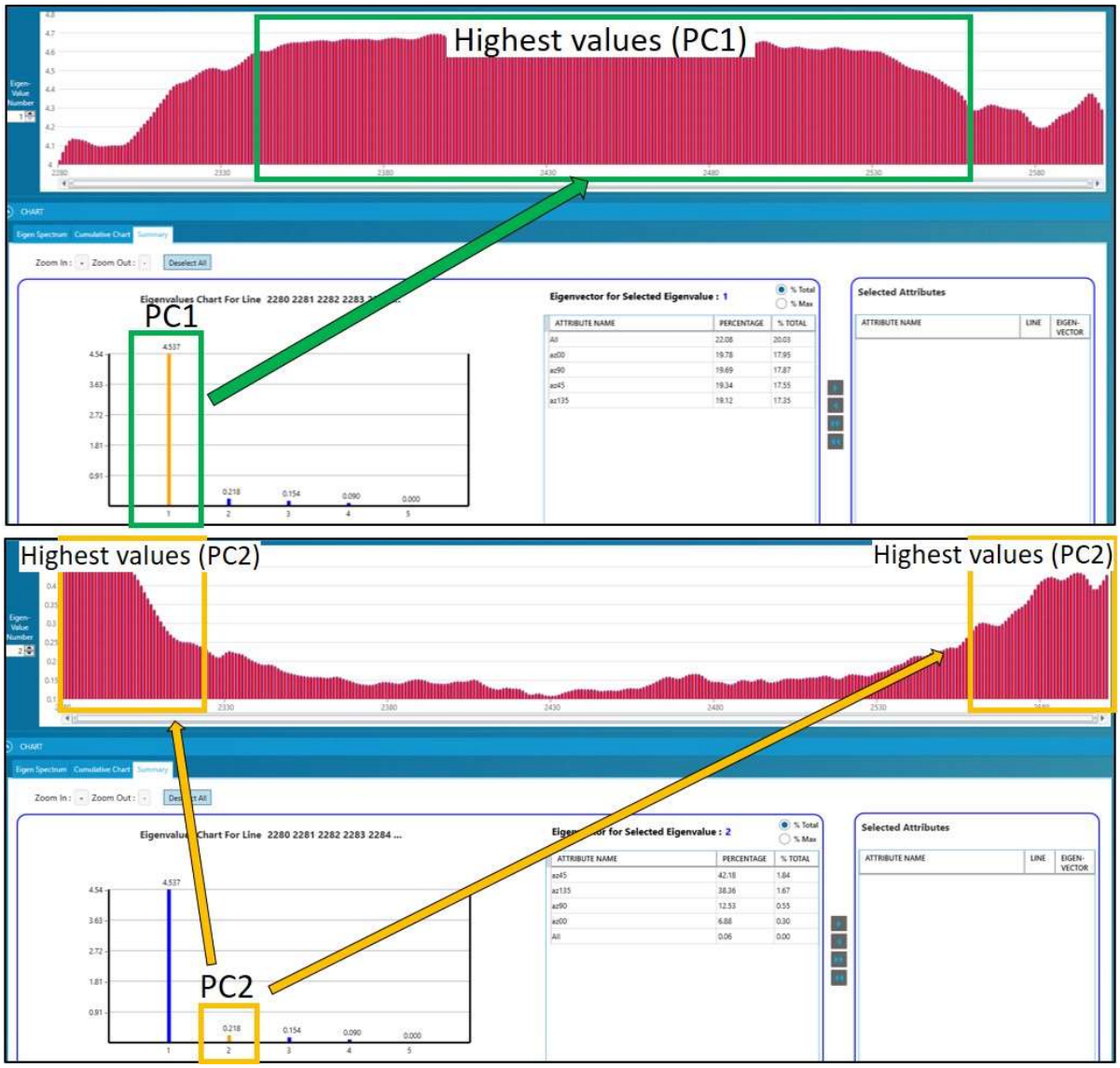
APPENDIX M – PCA results for different windows of observations.

The orange, red and blue polygons have different lateral and vertical extensions. In all three scenarios, the higher variability indicated with the first principal component is defined mainly by the energy-ratio attribute computed with the full-stack azimuth volume.



APPENDIX N – Comparison between the PCA results, considering the first and second principal components

Note how the higher eigenvalues associated with different lines are located towards the center of the survey for PC1 (green box) and towards the edges of the survey for PC2 (orange box).



APPENDIX O – PCA results (original amplitude volume vs. energy-ratio attribute)

